Structure-property correlations in compositionally complex ferroelectrics

by

Abinash Kumar

Submitted to the Department of Materials Science and Engineering
in partial fulfillment of the requirements for the degree of

Doctor of Philosophy

at the

MASSACHUSETTS INSTITUTE OF TECHNOLOGY

September 2022

Author .....
Department of Materials Science and Engineering
July 28, 2022

Certified by .....
James M. LeBeau
John Chipman Associate Professor of Materials Science and Engineering
Thesis Supervisor

Accepted by .....
Frances M. Ross
Ellen Swallow Richards Professor of Materials Science and Engineering
Chair, Departmental Committee on Graduate Student

Structure-property correlations in compositionally complex ferroelectrics

by

Abinash Kumar

Submitted to the Department of Materials Science and Engineering
on July 28, 2022, in partial fulfillment of the
requirements for the degree of
Doctor of Philosophy

Abstract

Compositional control in functional oxides can significantly alter material properties and lead to the emergence of unconventional behavior. Ferroelectrics with switchable polar ordering, for instance, are influenced by local compositional variation, thus requiring an understanding of structure-property relationships. My dissertation work focuses on using atomic scale characterization with an aberration-corrected scanning transmission electron microscope (STEM) to determine these structure-property correlations in two compositionally complex ferroelectric systems: compositionally heterogeneous relaxors and stoichiometry-controlled orthoferrites.

Relaxor ferroelectrics show exceptional electromechanical response, energy storage capacity, and electrocaloric properties, finding applications ranging from ultrasound imaging to electrical energy storage systems. These materials show nanoscale chemical and structural heterogeneity that make finding the origin of their exceptional properties a seemingly intractable problem. Here, I utilize STEM to quantify various types of nanoscale heterogeneities and determine their correlation with the nanoscale polar domain structure in a prototypical relaxor ferroelectric system $Pb(Mg_{1/3}Nb_{2/3})O_3$-$PbTiO_3$ (PMN-PT). I determined three types of heterogeneities: chemical order, oxygen octahedral tilt order, and oxygen octahedral distortion order. These heterogeneities vary with Ti content and show spatial correlation with low-angle domain walls, indicating their role in breaking down the long-range polar order and stabilizing the nanoscale domain structure essential for the relaxor response. I identified monoclinic-like distortions, which are related to both the Ti content and electromechanical response. The connection among heterogeneities in local chemistry, structure, and polarization is revealed through comprehensive STEM characterization. These experimental results also validate theoretical models proposed since the discovery of relaxors.

Further, due to the extensive demand for miniaturization of modern electronic devices, relaxor ferroelectrics are desired in their thin film forms. This requires a detailed study on the growth and characterization of compositionally heterogeneous relaxor ferroelectrics thin film. Consequently, investigating nanoscale domain struc-

tures under different conditions such as epitaxial strain is possible in thin films. With chemical and structural heterogeneities determining polar structure in bulk relaxors, their spatial distribution and behavior need to be determined to relate structure with properties in thin films. I determine the distribution of local chemistry and their role in the evolution of polar structure across thickness in PMN-PT relaxor thin films grown with pulsed-laser deposition (PLD). Further, I quantify the effect of epitaxial compressive strain in terms of the evolution of polar structure and chemical heterogeneities to explain the structural origin of decreasing relaxor behavior with strain. With an increase in epitaxial strain, the size of polar domains and chemical ordered regions increases along the film growth direction, yet the coupling among local chemistry and structure on a unit cell basis diminishes, thus showing poor relaxor response at highly strained films.

The second ferroelectric system of the interest is orthoferrites. These have been shown as potential single-phase multiferroic materials with the coexistence of both ferroelectric and magnetic ordering. These materials have unconventional ferroelectric behavior irrespective of their centrosymmetric structure in bulk form. Orthoferrite $YFeO_3$ (YFO) thin films even show composition-dependent ferroelectricity. Y-rich YFO thin films reveal ferroelectric behavior while Fe-rich films show no ferroelectric response, with the structural origins of such behavior yet to be determined. Here, I use STEM to probe the atomic structure and elemental distribution in stoichiometry-controlled YFO thin films grown by PLD. I determine Y_{Fe} antisites in Y-rich YFO thin films that are absent in Fe-rich films. These antisites modify the structure and break the local symmetry, stabilizing the ferroelectric ordering. In addition, planar defects such as antiphase boundaries (APBs) are also found in Y-rich YFO, which show large structural relaxations. Despite Y-rich composition, these APBs also host Fe_Y antisites, exhibiting bi-stable polar distortions. Density functional theory predicts the formation energy and polarization switching barrier reduces by a factor of three at these APBs, thus leading to changes in local properties. In the Y-rich YFO films, APBs show significantly lower density than Y_{Fe}antisites, indicating the ferroelectric response arises predominantly from Y_{Fe} antisites. These results reveal that defect engineering achieved via stoichiometry control allows tuning properties in functional orthoferrites.

Thesis Supervisor: James M. LeBeau
Title: John Chipman Associate Professor of Materials Science and Engineering

Acknowledgments

First, I would like to thank my advisor Prof. James M. LeBeau, for his guidance and support throughout this work. I am so grateful for the opportunity you provided me to be part of your group and work on some of the challenging materials. Without your support, encouragement, and countless discussions, I could not succeed with this work. I would like to thank Prof. Elizabeth Dickey for introducing me to relaxors and guiding me on this work. I would also like to thank my committee members Prof. Bilge Yildiz and Prof. Caroline Ross, for their time and feedback in guiding this work.

I am also thankful to present and past group members of the LeBeau group for their help, including Dr. Dennis Kim, Michael Xu, Xi Chen, Dr. Junghwa Kim, Colin Gilgenbach, Dr. Matthew Cabral, Dr. Rohan Dhall, Dr. Matthew Hauwiller, Dr. Aubrey Penn and Tim Eldred.

I am very fortunate to get the opportunity to work with amazing collaborators, Prof. Lane Martin, Prof. Andrew Rappe, Prof. Shujun Zhang, Prof. Douglas Irving, Dr. Jieun Kim, Dr. Jonathon Baker, Dr. Preston Bowes, Dr. Shuai Ning, Dr. Konstantin Klyukin, Eunsoo Cho, Dr. Hiroyuki Takenaka, Dr. Yubo Qi, Dr. Cigdem Ozsoy-Keskinbora, Dr. Mikhail Ovsyanko, Dr. Felix van Uden and Dr. Ruud Krijnen.

Many thanks to my friends Kaushik Borah, Siddarth Ghule, Tamzid Ibn Minhaj, Mohammad Delower Hossain, Yash Mehta, Mehedi Hasan Rizvi, and Abhijeet Anand for always being there for me in tough moments.

I am thankful to my parents and sisters for their love, support, and encouragement. Whatever I have achieved is not possible without you.

Finally, I also like to acknowledge National Science Foundation for the support for my thesis work as part of the Center for Dielectrics and Piezoelectrics under grant nos IIP-1841453 and IIP-1841466. I like to thank the support from ARL/ARO via the Collaborative for Hierarchical Agile and Responsive Materials (CHARM), under Cooperative Agreement No. W911NF-19-2-0119 and NVIDIA Corporation for providing

the NVIDIA Titan Xp GPU. I like to acknowledge the MIT Mathworks engineering fellowship and John Chipman Career Development Professorship for their support. This thesis work was performed in part at the Analytical Instrumentation Facility (AIF) at North Carolina State University, which is supported by the State of North Carolina and the National Science Foundation (ECCS-1542015). AIF is a member of the North Carolina Research Triangle Nanotechnology Network (RTNN), a site in the National Nanotechnology Coordinated Infrastructure (NNCI). This work was also carried out in part through the use of the MIT Characterization.Nano facility and the Harvard University Center for Nanoscale Systems (CNS), a member of the National Nanotechnology Coordinated Infrastructure Network (NNCI), which is supported by the National Science Foundation under NSF Grant No. 1541959.

Contents

List of Figures

Chapter 1

Introduction

Part of the text in this chapter is from ref[1, 2] and reproduced with permission from Springer Nature as cited, "The author of articles published by Springer Nature do not usually need to seek permission for reuse of their material as long as the journal is credited with initial publication. Ownership of copyright in original research articles remains with the Author, and provided that, when reproducing the contribution or extracts from it or from the Supplementary Information, the Author acknowledges first and reference publication in the Journal". In this chapter, part of the text is also used with permission of John Wiley & Sons - Books, from ref. [3]; permission conveyed through Copyright Clearance Center, Inc as cited, " Use of proper copyright notice for a Work is required as a condition of any License granted under the Service. Unless otherwise provided in the Order Confirmation, a proper copyright notice will read substantially as follows "Used with permission of John Wiley & Sons - Books, from ref. [3] [Antisite Defects Stabilized by Antiphase Boundaries in $YFeO_3$ Thin Films, Abinash Kumar, Konstantin Klyukin, Shuai Ning, Cigdem Ozsoy-Keskinbora, Mikhail Ovsyanko, Felix van Uden, Ruud Krijnen, Bilge Yildiz, Caroline A. Ross, and James M. LeBeau, Adv. Funct. Mater., 32, 9, 2021]; permission conveyed through Copyright Clearance Center, Inc." Such notice must be provided in a reasonably legible font size and must be placed either on a cover page or in another location that any person, upon gaining access to the material which is the subject of a permission, shall see, or in the case of republication Licenses, immediately adjacent to the Work as

used (for example, as part of a by-line or footnote) or in the place where substantially all other credits or notices for the new work containing the republished Work are located. Failure to include the required notice results in loss to the Rightholder and CCC, and the User shall be liable to pay liquidated damages for each such failure equal to twice the use fee specified in the Order Confirmation, in addition to the use fee itself and any other fees and charges specified."

Ferroelectrics show spontaneous polarization, switchable under an external electric field. These find applications as electrocaloric coolers, low-power non-volatile memory devices, capacitors, thermistors, actuators, etc. [4]. Most of the modern electronic devices use oxides-based ferroelectric materials due to their excellent performance and stability. The ferroelectric behavior in the functional oxides has shown greater sensitivity towards local chemistry and defects due to long-range Coulombic forces, which favor the ferroelectric state [5]. Thus, a complete understanding of structure-property relationships in the composition space is critical in ferroelectric oxides to achieve unprecedented control of ferroelectric behavior in them. Here, I determine the relationship between chemistry, structure, and ferroelectric properties in two compositionally complex ferroelectric systems, compositionally heterogeneous relaxors and stoichiometry-controlled orthoferrites, using a scanning transmission electron microscope (STEM).

Below, I will discuss the key characteristics of relaxor and orthoferrite ferroelectrics and find the intriguing questions that need to be answered to establish structure-property relationships in them. In the case of relaxor ferroelectrics, I will focus on the bulk and thin films form of $Pb(Mg_{1/3}Nb_{2/3})O_3$-$PbTiO_3$ (PMN-PT) [1] while in orthoferrites, $YFeO_3$ (YFO) thin films will be explored [2, 3].

The first ferroelectric system, relaxor ferroelectric, shows differences from normal/traditional ferroelectrics by their frequency-dependent, diffuse phase transitions that are commonly attributed to the existence of nanoscale order [6]. Among this class of materials, Pb-based systems remain essential as they exhibit the largest known piezoelectric coefficients and outstanding dielectric properties [7–9]. These properties have been commonly attributed to polar nano regions in the material that align to

the applied field [10, 11]. However, this simple model fails to explain relaxor behavior in various materials, including polymer-based systems [12]. The recently proposed "polar slush" model overcomes these limitations by considering a multi-domain polar state with low energy and low angle domain walls formed throughout [13]. However, model validation has been hindered by the seemingly endless number of structural characterization studies with differing interpretations, leading these systems to be described as a "hopeless mess" [6].

$Pb(Mg_{1/3}Nb_{2/3})O_3$-$PbTiO_3$ (PMN-PT) is the prototypical Pb-based relaxor ferroelectric system and exhibits state-of-the-art properties. For example, piezoelectric constants up to 4100 pC/N have been achieved via Sm doping [14]. PMN-PT adopts the perovskite structure (formula ABO_3) with the A sub-lattice occupied by Pb and the B sub-lattice occupied by either Mg, Nb, or Ti. Furthermore, as $PbTiO_3$ is added to PMN, the system reaches a morphotropic phase boundary (MPB) near PMN-30PT, where the electromechanical properties are maximized [15]. Deciphering the origins of these enhanced properties is, however, complicated by nanoscale heterogeneity of chemistry and structure. While X-ray and neutron scattering are the predominant characterization methods used to explain these details, making direct connections between composition, structure, and polarization have proven exceedingly difficult [16–22]. For example, while the nanoscale chemical ordering of the B sub-lattice cations was one of the first signatures revealed [22, 23] and is found to varying degrees in all Pb-based relaxor ferroelectrics[24, 25], its details are still being explored [26–28].

Capturing a complete picture of the connection between chemistry, structure, and polarization in relaxor ferroelectrics requires characterization techniques that can account for both cation *and* anion sub-lattices. While distortions of the oxygen sub-lattice have been previously detected [29], a combination of X-ray and neutron diffraction recently discovered that correlated oxygen displacements are likely integral to bringing forth the outstanding electromechanical properties in PMN-PT [15]. Diffraction characterization methods, however, lack the spatial resolution required to directly determine the origin of nanoscale polar variation [30, 31]. In contrast, a scanning transmission electron microscope (STEM) can readily image the projected

crystal structure at the atomic length scale, enabling a correlation between polarization, chemistry, and structure directly at the atomic scale. This will allow us to reveal the structure of relaxors, which has been missing since their discovery.

The second ferroelectric system, orthoferrites $YFeO_3$ (YFO) reveals a centrosymmetric structure (non-polar) and antiferromagnetic behavior [32, 33]. Recently, it has exhibited unconventional ferroelectric behavior depending on stoichiometry in the thin film form [2]. YFO films with Y-rich composition show ferroelectric behavior while absent in Fe-rich films. Film composition with even 20 % excess Y shows a stable structure and excellent ferroelectric behavior, indicating the presence of functional defects in them. Point and planar defects in functional oxides have shown significant changes in their properties. Point defects such as antisites enhance functional behavior and induce new functional properties in off-stoichiometric systems. Antisites of Fe and Mo in mixed ionic and electronic conductors based on strontium iron molybdenum oxide $Sr_2Fe_{2-x}Mo_xO_{6-\delta}$ reveals lower oxygen vacancy formation energy, thus, expected higher oxygen vacancy concentration leads to higher ion diffusion [34]. Presence of Ti_{Sr} antisites leads to room-temperature ferroelectricity in $SrTiO_3$ [35]. Pb_{Zr} antisites shows ferroelectric polar distortions in anti-ferroelectric $PbZrO_3$ [36]. Planar defects, such as twins or antiphase boundaries (APBs), in the ferroic systems, can also modify both the local magnetic and polarization responses. Importantly, the behavior at the boundaries differs greatly from the rest of the material. For example, twins in $CaTiO_3$ have been shown to exhibit polar displacements that lead to local ferroelectricity [37, 38]. Similarly, the presence of APBs in Fe_3O_4 reduces the total magnetization [39]. Thus, understanding functional defects and their role in determining the local structure is necessary to explain the unconventional ferroelectricity in YFO thin films with stoichiometry control.

In the following sections, I will introduce relaxor and orthoferrite ferroelectrics in detail and discuss the key questions which will be answered in the later chapters of this thesis. The organization of the thesis is mentioned in the last section of this chapter.

1.1 Introduction to Relaxor ferroelectrics

Relaxor ferroelectrics show high dielectric, electrocaloric, and exceptional electromechanical properties, making them attractive for various applications ranging from ultrasound imaging to actuators [7–9, 31, 40, 41]. These also exhibit a broad maximum in the temperature-dependent dielectric permittivity curve, and frequency dependence for temperature maximum of dielectric permittivity, also termed dielectric relaxation [42, 43]. Such characteristic behavior has been related to compositional heterogeneities in these systems. Relaxor systems are mostly compositionally complex where two or multiple elements occupy the specific cation sites A or B, creating compositional heterogeneity in the systems. Relaxor behavior has been found in both Pb and Pb free oxide systems with perovskite or tungsten bronze structures [44]. Especially, Pb based relaxor systems such as $Pb(Mg_{1/3}Nb_{2/3})O_3$-$PbTiO_3$ (PMN-PT), $Pb(Zn_{1/3}Nb_{2/3})O_3$-$PbTiO_3$ (PZN-PT), $Pb(Sc_{1/2}Ta_{1/2})O_3$ (PST), $Pb(In_{1/2}Nb_{1/2})O_3$ (PIN) etc. have been studied extensively in the past due to their exceptional relaxor behavior as compared to Pb-free ones such as $Ba_{1/2}Na_{1/2}TiO_3$ (BNT), $Sr_xBa_{1-x}Nb_2O_6$ (SBN), $BaSn_xTi_{1-x}O_3$ (BST) and $BaZr_xTi_{1-x}O_3$ (BZT) [44–46]. Apart from compositional heterogeneity, these relaxor ferroelectrics also show distinct behavior than normal ferroelectrics, as discussed below.

1.1.1 Comparison between relaxor and normal ferroelectrics

The dielectric response of normal ferroelectrics, such as $PbTiO_3$ or $BaTiO_3$ obeys the Curie-Weiss law [47, 48]. In the Curie-Weiss law, dielectric permittivity is defined as:

$$\epsilon = \frac{A}{T - T_c}$$

Where A is a material-dependent Curie constant, T is the temperature, and T_c is the Curie temperature of the material. In the case of normal ferroelectrics, the temperature-dependent dielectric permittivity curve shows sharp maxima at the Curie temperature, following the Curie-Weiss law. Below T_c, normal ferroelectrics

show spontaneous polarization accompanied by the changes in the lattice symmetry. For example, above Curie temperature (T_c), $BaTiO_3$ shows cubic symmetry, a centrosymmetric structure, and thus does not show electric polarization. Below T_c, it transforms to tetragonal symmetry, a non-centrosymmetric structure, thus stabilizing electric polarization [47]. While relaxors exhibit a broad maximum in the temperature-dependant dielectric permittivity curve (Figures1-1 a & b). The temperature for maximum dielectric permittivity (T_m) revealed frequency dependence and was uncorrelated with any change in crystal symmetry unlike normal ferroelectrics [49, 50].

Relaxors can also be distinguished from normal ferroelectrics based on the shape of the hysteresis loop of materials polarization with an applied electric field (P-E). In normal ferroelectrics, polarization show hysteresis behavior with an applied electric field. Below T_c, ferroelectrics consist of polar domains with boundaries, i.e., domain walls, to minimize the free energy. The hysteretic behavior arises from the change in polarization in each domain and the movement of domain walls [51]. There are three key features of the loop, remanent polarization (P_r), saturation polarization (P_s), and coercive field (E_c). Ferroelectrics show net/spontaneous polarization even without an external electric field, termed remanent polarization (P_r). The saturation polarization is defined as the maximum polarization achieved at the highest applied electric field. In ferroelectrics, polarization in domains aligns along the applied electric field direction to minimize the potential energy. With switching the direction of the applied electric field in the opposite direction, polarization goes through a net zero polarization state at a characteristics electric field termed a coercive field. Relaxors show lower remanent polarization due to nanoscale domain structure than normal ferroelectrics, as shown in Figures1-1 c & d [52]. Relaxors also have smaller coercive field values as it is much easier to change the nanoscale domain structure in relaxors than in microscale domains in normal ferroelectrics.

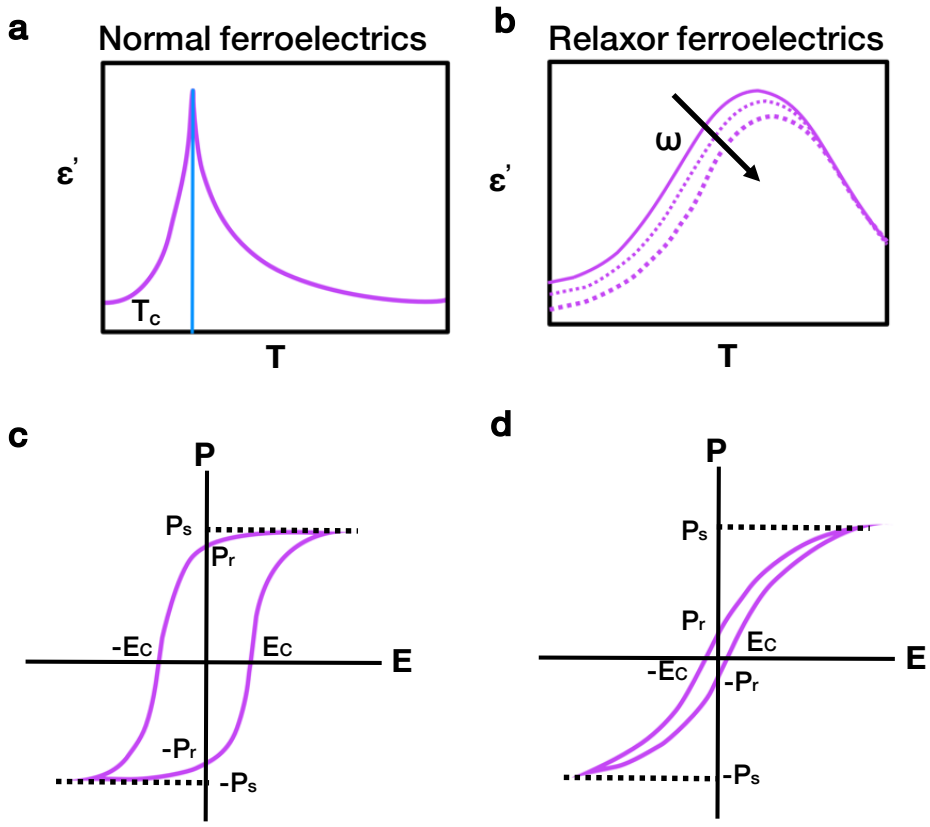

Figure 1-1: The temperature-dependent real part of dielectric permittivity for (a) normal and (b) relaxor ferroelectrics. Polarization-Electric field hysteresis loop for (c) normal and (d) relaxor ferroelectrics. ω denotes the frequency of the applied electric field.

1.2 Characteristics features in relaxors

1.2.1 Chemical ordering

With compositional complexities in relaxors, spatial variations in local chemistry have been also observed. The presence of short-range chemical ordering is found in several relaxor systems such as PMN-PT, PZN-PT, PST, PIN, etc. [22, 45]. It has been also observed that relaxor behavior is absent in systems with either long-range chemical ordering or completely disorder; thus, the short-range chemical order has been attributed as a critical feature for relaxor behavior. Characterization techniques such as X-ray, neutron, and electron diffraction show distinct superlattice spots due to the doubling of the unit cell size with chemical order. Transmission electron microscopy

has been extensively applied to study these short-range ordered regions as it provides distinct superlattice spots in diffraction patterns and also allows to visualize of local chemically ordered regions in real space with dark field TEM imaging using superlattice spots[45]. This also enables to characterization of chemical ordering behavior with changing chemical composition, as in the case of the PMN-xPT system. The intensity of superlattice spots in the electron diffraction pattern of PMN decreases with the addition of $PbTiO_3$ (PT) content [45]. This has been attributed to the decrease in the short-range chemical ordering with the addition of a higher amount of PT in PMN [22, 23].

The atomic structure of these chemical-ordered regions in PMN has been initially proposed as 1:1 type ordering of Mg^{2+} and Nb^{5+}, which is also termed the space-charge model. Here, B site atomic columns alternate between pure Mg^{2+} and Nb^{5+}. However, with further scattering and microscopy experiments [26–28], it is revealed that ordering occurs with two sites named β_I and β_{II} on (111) planes, where β_I contains Mg^{2+} and Nb^{5+} in a 2:1 ratio while neighboring β_{II} sites comprised of only Nb^{5+}. This model is defined as a random site model. These two models are also distinguished based on the local charge neutrality across the chemical-ordered regions. The random site model indicates the charge-neutral ordered regions, while the space charge model predicts these to be charged.

In the attempt to establish the connection between chemically ordered regions and nanoscale polar domain structure in relaxors, different perspectives have been found in the literature regarding spatial correlations among them. Burton et al. [53] predicted polar nanoregions (PNRs) to be formed in these chemically ordered regions, while Eremenko et al. [28] revealed that no spatial connection exists between ordered regions and PNRs. Thus, the relation of ordered regions in determining nanoscale domain structure in relaxors is still missing.

1.2.2 Diffuse scattering

Further, relaxors show diffuse scattering features in X-ray, neutron, or electron diffraction experiments which are commonly attributed to the presence of inhomogeneous

structural regions in a crystalline material [54]. Thus, these have been used extensively to probe the structural heterogeneity and, ultimately, the origin of relaxor behavior [11, 15, 20, 27, 31, 55–57]. In PMN-PT, butterfly-shaped diffuse scattering around the 100 Bragg peak had been attributed to the presence of PNRs with correlated Pb displacements. Various structural models for relaxors have also been benchmarked with similar diffuse scattering patterns over the years [13].

Recent comparative diffuse scattering studies on the PMN-PT system using X-ray and neutron scattering have revealed the significant role of correlated oxygen displacements in determining the relaxor behavior [15]. X-ray scattering showed a symmetric butterfly diffuse scattering, while neutron scattering exhibited an asymmetric diffuse pattern in the PMN-30PT bulk sample. As X-ray scattering mostly captures cation displacements, while neutron scattering is sensitive to the displacement of both cations and anions in the material, such an asymmetric diffuse pattern in neutron scattering indicates the existence of correlated oxygen displacements, which could play a significant role in determining the structure of PNRs in the system.

1.3 Structural models for relaxors

1.3.1 Polar nanoregions in a non-polar matrix

G. A. Smolensky and V. A. Isupov suggested relaxor behavior can be found in materials where two or more cations occupy equivalent crystallographic sites [22, 58]. The distribution of these cations gives rise to local chemical fluctuations, thus forming microregions with different compositions and thus showing distinct curie temperatures. These microregions were proposed as isolated polar regions surrounded by a non-polar phase (Figure 1-2a). The broad phase transition observed in the relaxor was explained as the summation of individual phase transitions from these individual microregions thus, give rise to broad curie temperature as shown in Figure 1-2b [46].

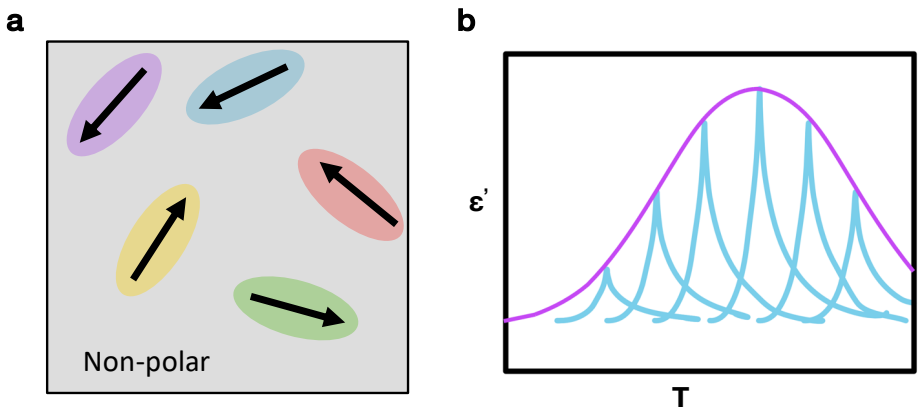

Figure 1-2: Illustration of (a) structural model for relaxors, i.e., the existence of PNRs in the non-polar matrix, and (b) broad peak in temperature dependant dielectric permittivity curve is a result of the summation of the individual curve from PNRs with distinct composition and thus curie temperature.

1.3.2 The Superparaelectric model

Relaxors are known to have a stable nanoscale domain structure. As ferroelectricity is a cooperative phenomenon that scales with the sample volume, smaller polar nano regions cannot withstand the thermal energy effects, leading to the randomization of polarization in the structure [46]. This also decreases the energy barrier for polarization switching between equivalent directions in a crystal depending on its structure. With a smaller crystal size, the energy barrier becomes comparable to the thermal energy, thus allowing regions to have all equivalent polar directions. This resembles the superparaelectric state where an ensemble of small polar regions whose sizes are characterized by the spatial coherence of their spontaneous polarization shows the polarization reorientation energy is of the order of the thermal energy of the crystal (K_BT); thus, the polarization of each cluster tends to fluctuate independently. Therefore, the superparaelectric model is proposed as the structural model of relaxors where the nature of polarization behavior in polar microregions was visualized as the dynamics of superparaelectric states [42]. The model explicitly states that the cation ordering in a disordered matrix produces local potential wells within the lattice where the superparaelectric potentials stabilize [22]. This also leads to potential differences between chemically ordered and disordered regions, which eventually cause strain

and electrostatic energy differences between these distinct regions. Such a potential barrier also causes short-range polar domains to be stable.

1.3.3 Dipolar-glass model

In a dipolar glass, dipoles froze below a given freezing temperature (T_f), leading to randomness in dipoles and the absence of long-range polar order. Dipolar glasses and relaxor ferroelectrics exhibit common features such as a broad temperature-dependent quasistatic dielectric permittivity and strong frequency dispersion of the dynamic dielectric permittivity [59]. These also show Vogel-Fulcher (VF) type dielectric relaxation behavior as followed by the equation [60]:

$$\omega = \omega_o \exp[\frac{-E_a}{K(T_m - T_f)}]$$

Where ω is the measured frequency, ω_o is the characteristic frequency, E_a is the activation energy, T_m is the maximum dielectric temperature, and T_f is the freezing temperature. A cooperative rearrangement of dipoles in a disordered polar system has been proposed as a possible relaxation mechanism in relaxors. This is analogous to the behavior of molecules in a supercooled glass-forming viscous liquid [61].

1.3.4 Random field model

The random field model proposes that relaxors consist of random distribution of electric dipoles and lattice defects such as vacancies, antisites, etc., embedded in a paraelectric matrix [49]. The formation of polar nano regions can be explained by the quenched electric field interacting with the atomic displacements. The origin of fluctuations of the static electric fields can vary across different samples. For example, in PMN, partial occupancy of heterovalent cations, Mg^{2+} and Nb^{5+} has been realized to cause microscopic fluctuations in electric fields,[62] while in tungsten bronze structure of $Sr_xBa_{1-x}Nb_2O_6$ (SBN), an empty A site out of four A2 and two A1 sites per elementary lattice cell give rise to effective disorder and static electric fields [63]. In SBN, this leads to the polar displacements of Nb^{5+} cations away from

their mean positions in the NbO_6 octahedra. Additionally, partial occupancies of Ba^{2+} and Sr^{2+} lead to oxygen ion distortions due to differences in bond lengths of Ba-O and Sr-O. Thus, NbO_6 octahedra show local buckling and tilt deformation, thus creating additional random fields. In the case of isovalent B site cations systems, $BaTi_{1-x}Sn_xO_3$ and $BaTi_{1-x}Zr_xO_3$, a larger ionic radius of Sn^{4+} and Zr^{4+} as compared to Ti^{4+} show loss of off-centrality locally in respective systems. Such change in the local bonding environment leads to broken bonds; thus, redistributions of charges due to a local change in polarizability give rise to random quenched dipolar electric fields in these systems. Interactions of such random fluctuations in the electric field with local dipoles were attributed to the formation of nanoscale polar regions in relaxors.

1.3.5 Polar slush model

Recently, using molecular dynamics simulations, the structure of the relaxor has been proposed as composed of polar domains ranging from 2 to 10 nm distributed randomly without any non-polar matrix [13]. The dielectric response from such a multi-domain state in relaxors has been shown to be analogous to the water. This model proposed that in relaxors, even at the lower temperatures, mainly below their freezing point, polar nanodomains exhibit strong but incomplete correlations, while regions between these polar domains reveal weak correlations. These incomplete correlations lead to collective rotations of dipoles being slow in individual domains. Such polarization rotation behavior in nanodomains of relaxors is comparable to the dynamics of small ordered crystals in slush water. Small ordered crystals in the slush water show slow dynamics of the molecules compared to the liquid surrounding them. These small ordered crystals are also free to rotate with respect to each other similar to the behavior of polar nanodomains in these relaxors. Thus, a slushy multi-domain state has been proposed to be a better model to describe relaxors.

This model also discussed the effect of local composition in relaxors. Mg-rich unit cell sites have been found to act as domain walls to decouple the polarization fluctuations in the neighboring sites, thus stabilizing the nanoscale domain structure. The presence of underbonded oxygen atoms from Mg^{2+} and small off-centering due

to their size and electronic structure is proposed to decouple the polarizations in nanodomains structure. This model successfully predicted features of relaxors, such as diffuse scattering, diffuse phase transition, and dielectric relaxation. This also explains relaxor behavior in the terpolymer system, P(VDF-TrFE- CTFE), which was not possible with previous models [12].

The above theoretical models provide two main contrasting pictures for the structure of relaxor behavior. One, polar nano regions exist in a non-polar matrix, and the second one is the existence of a multi-domain state without any non-polar component. Further, these models reveal the role of chemically ordered and structurally distorted regions in creating nanoscale domain structure to be either prominent or no role at all. Multiple attempts have been made to resolve the structure, but even inferences from structural characterization techniques reveal the differing structure of relaxors. STEM enables to obtain information of all cations and anions on a unit cell basis. This allows to map polarization across the sample, revealing if relaxors comprises polar nano regions with non-polar component or if these have multi-domains with low-angle domain walls. STEM can also identify the spatial distribution of chemically ordered regions and structural distortions, thus finding their role in creating nanoscale domain structure in relaxors. Thus, STEM imaging will allow obtaining the structure of relaxors in real space and also find the origin of their nanoscale domain structure in them.

1.4 Introduction to Orthoferrite perovskites

Orthoferrite perovskites have been predicted to be potential multiferroic materials. Multiferroics show combined ferroelectric and magnetic properties, thus exhibiting magnetoelectric coupling, which is of great interest in designing spintronic and magnetoelectric devices [64–67]. Few materials show both ferroelectricity and magnetism due to differences in the intrinsic mechanisms for these properties [68]. For materials to show ferroelectricity, either the 'd^0-ness' condition as shown by the Ti^{4+} ion in $BaTiO_3$, or lone pair stereochemical activity as on the Pb^{2+} in $PbTiO_3$ [69] needs

to be satisfied. While partially filled localized (f-electron) states on rare earth ions or partially occupied d levels in transition metals are found to give rise to magnetic properties. Thus, finding the multiferroic behavior in a single material is rare.

A prototypical multiferroic, $BiFeO_3$, shows significant ferroelectric distortions arising from the stereochemical activity of the Bi^{3+} $6s^2$ 'lone pair' electrons and antiferromagnetism from the 3d electrons of Fe [68]. In $SrMnO_3$, strain effects lead to partially filled d electron systems having cation off-centering [70]. (Eu, Ba)TiO_3 shows multiferroic behavior arising from the d^0 condition for ferroelectricity and magnetism from the f electron condition [71]. Other mechanisms for multiferroic behavior include geometrically-driven ferroelectricity from polyhedral rotations [72] or electronically-driven ferroelectricity due to charge ordering [73].

Orthoferrites, $AFeO_3$ with the orthorhombic unit cell, have recently received considerable attention due to their magnetic properties. $TmFeO_3$ shows magnetocaloric behavior finds application in magnetic refrigerants [74]. Recently, multiferroic behavior has been observed in orthoferrites, $SmFeO_3$ (SFO), $LaFeO_3$ (LFO), and $YFeO_3$ (YFO) despite their centrosymmetric structure, which inhibits spontaneous polarization[75, 76]. The spin-orbit coupling has been attributed to unconventional ferroelectric behavior in $SmFeO_3$ [75]. Meanwhile, in YFO, due to an empty 4f orbital for Y^{3+} ions, ferroelectricity cannot originate from spin-exchange interactions. The ferroelectricity in YFO also shows a strong dependence on the stoichiometry of the sample [2]. Y-rich YFO shows ferroelectricity, while Fe-rich reveals non-ferroelectric behavior. The mechanism for the ferroelectric behavior in the stoichiometry-controlled YFO is yet to be determined. Even the YFO thin film with excess 20% of Y shows stable structure and ferroelectricity, suggesting the presence of point or/and planar functional defects. The distribution of functional defects across the YFO thin films needs to be determined along with their contributions to creating local structural distortions, which lead to the breaking of the inversion symmetry to explain their stable ferroelectric ordering. STEM imaging and spectroscopy enable to identify the type of functional defects, point or/and planar, and their distribution across the YFO thin film. This also allows mapping local structural distortions across defects and sym-

metry changes at the unit cell level critical to explaining the structural origin of the ferroelectric behavior in the stoichiometry-controlled YFO films.

1.5 Key Questions & Thesis Organization

In this thesis, I focus on understanding the structure-property relationships in compositionally heterogeneous relaxors and stoichiometry-controlled orthoferrites using STEM. The atomic scale characterization of these compositionally complex ferroelectrics using an aberration-corrected STEM allows us to understand the convoluted correlations among the chemistry, structure, and ferroelectric properties. My thesis consists of seven chapters; where chapter two discusses methods used in studying the various material systems in this thesis, and contents of each chapter, from three to seven, are discussed as follows with key questions:

- Chapter 3 answers the key questions about the origin of relaxor behavior in Pb-based systems and their composition-dependent electromechanical coupling response. In this chapter, through aberration-corrected STEM imaging, I determine the structural and chemical origins of relaxor ferroelectric properties in PMN-xPT (x=0, 10, and 30). I identify three main types of heterogeneities, chemical, oxygen octahedral tilt, and oxygen octahedral distortion orders, which show spatial correlations with low-angle domain walls. This indicates the key role of these chemical and structural heterogeneities in breaking down the long-range polar order leading to nanoscale domain structure and relaxor behavior. Further, monoclinic-like structural distortions of octahedra show direct correlations with composition dependant electromechanical response. These results also validate theoretical models proposed to describe the structural origin of relaxor behavior.

- As thin films provides a platform to develop the design principles to tune properties with extremely controlled growth conditions. Chapter 4 develops an understanding of the distribution of structural and chemical heterogeneities and the

evolution of polar structure in relaxor thin films, which is key to achieving complete control over the relaxor properties. Through imaging and spectroscopy in STEM, the spatial distribution of heterogeneities and polar structure evolution across film thickness are directly correlated with the local chemical variation across the film. The influence of the combination of epitaxial strain from the substrate and chemical pressure in determining local chemistry during the thin film growth is also discussed. Further, the critical film thickness phenomenon to obtain stable relaxor ferroelectric behavior is determined by studying the polar structure evolution in film grown with varying thicknesses. These results allow to the development of strategies to engineer relaxor thin films with changing growth conditions and film thickness.

- Chapter 5 aims to determine the structural origin for decreasing relaxor behavior with increasing biaxial in-plane compressive strain in thin films. Atomic scale characterization of PMN-PT relaxor thin films allows us to understand the changes in the correlations among chemistry, structure, and properties under strain conditions. The polar structure shows strong influence under strain and reveals an increase in polar ordering with higher strain. Chemical heterogeneities such as chemical order also revealed significant variation with strain due to coupling of local strain from these ordered regions and epitaxial strain from the lattice mismatch between thin film and substrate. An increase in epitaxial strain also leads to a weaker correlation between local lattice parameters and chemistry in these thin films, indicating a decoupling of polar distortions from local chemical variation and thus decreasing the relaxor behavior.

- Chapter 6 focuses on revealing the structural origin of unconventional ferroelectric behavior achieved with stoichiometry control in orthoferrite YFO thin films. STEM allows identifying point and planar defects in YFO thin films grown with changing stoichiometry. Y_{Fe} antisites are found in ferroelectric Y-rich YFO thin films, while such defects are absent in non-ferroelectric Fe-rich YFO. These also reveal the breaking of crystal inversion symmetry, thus sta-

bilizing the ferroelectric order in Y-rich YFO films. Planar defects such as antiphase boundaries (APBs) also show strong structural relaxation and become the perfect host to stabilize Fe_Y antisites which are not expected to form within the structure. APBs show bi-stable polar behavior where the presence of Fe_Y antisites significantly decreases the ferroelectric switching barrier. While APBs also reveal ferroelectric behavior, these show substantially lower density than Y_{Fe} antisites across the YFO thin films. Thus, the out-of-plane ferroelectric response in Y-rich YFO thin films is found to arise predominantly from Y_{Fe} antisites.

- In Chapter 7, a summary of the results and conclusion are presented with suggestions for future work in the characterization of compositionally complex relaxors and orthoferrites ferroelectrics.

Chapter 2

Materials and Methods

In this chapter, part of the text is also used with permission of John Wiley & Sons - Books, from ref. [3]; permission conveyed through Copyright Clearance Center, Inc as cited, " Use of proper copyright notice for a Work is required as a condition of any License granted under the Service. Unless otherwise provided in the Order Confirmation, a proper copyright notice will read substantially as follows "Used with permission of John Wiley & Sons - Books, from ref. [3] [Antisite Defects Stabilized by Antiphase Boundaries in $YFeO_3$ Thin Films, Abinash Kumar, Konstantin Klyukin, Shuai Ning, Cigdem Ozsoy-Keskinbora, Mikhail Ovsyanko, Felix van Uden, Ruud Krijnen, Bilge Yildiz, Caroline A. Ross, and James M. LeBeau, Adv. Funct. Mater., 32, 9, 2021]; permission conveyed through Copyright Clearance Center, Inc." Such notice must be provided in a reasonably legible font size and must be placed either on a cover page or in another location that any person, upon gaining access to the material which is the subject of a permission, shall see, or in the case of republication Licenses, immediately adjacent to the Work as used (for example, as part of a by-line or footnote) or in the place where substantially all other credits or notices for the new work containing the republished Work are located. Failure to include the required notice results in loss to the Rightholder and CCC, and the User shall be liable to pay liquidated damages for each such failure equal to twice the use fee specified in the Order Confirmation, in addition to the use fee itself and any other fees and charges specified."

The following sections discuss growth, sample preparation, and microscopy methods to characterize bulk and thin films of relaxor ferroelectrics and orthoferrites. The bulk samples of PMN, PMN-10PT, and PMN-30PT were grown by Prof. Shujun Zhang at the University of Wollongong, Wollongong, Australia. The thin films samples of PMN-32PT with varying thickness and epitaxial strain were grown by Dr. Jieun Kim under the supervision of Prof. Lane Martin at the University of California, Berkeley, California, the United States of America, and YFO thin films were grown by Dr. Shuai Ning under the supervision of Prof. Caroline Ross at Massachusetts Institute of Technology, Cambridge, Massachusetts, United States of America.

2.1 Single Crystal and Thin Films Growth

2.1.1 PMN and PMN-xPT single crystal growth

The PMN single crystals used to study the origin of relaxor behavior were grown via the high-temperature flux method [8, 77]. In this method, high purity powder samples of Pb_3O_4 and $MgNb_2O_6$ weighted according to the stoichiometric composition were mixed properly and put in a platinum crucible. Further, the platinum crucible was sealed inside an alumina crucible to minimize PbO evaporation at higher temperatures. This assembly was kept in a furnace at a temperature of 1200-1250°C for several hours to homogenize the melt. PMN crystals were formed by slow cooling at the rate of 0.5-1.0°C per hour of the melt solution. After finishing the growth process, the furnace was cooled down to room temperature at the rate of 50-100°C per hour. Further, these as-grown single crystals were leached out using nitric acid.

PMN-10PT and PMN-30PT single crystals (chapter 3) were grown via a modified Bridgeman method [8, 77]. Growth of PMN-PT single crystals was also performed in a platinum crucible with a mixture of high purity powder samples of Pb_3O_4, $MgNb_2O_6$, and TiO_2 weighted according to the desired composition and PbO as the flux. A seed PMN-PT crystal was sealed with a platinum lid to avoid PbO evaporation at higher temperatures. This assembly was placed in an alumina buffer tube filled with alumina

or zirconia powders. This was placed in a multi-zone heating furnace at a temperature above 1350°C for 5-10 hours to homogenize the melt. An axial temperature gradient of >20°C/cm was maintained at the solid-liquid interface. Crystal growth occurred with the platinum crucible being slowly lowered through the temperature gradient at the speed of <1mm/hr. After the completion of the growth process, the furnace was cooled to room temperature at a rate of 50°C/hr to avoid cracking of these single crystals.

2.1.2 PMN-PT thin film growth

The PMN-PT thin films (chapters 4 & 5), were grown using pulsed laser deposition (PLD) using a KrF excimer laser (248 nm, LPX 300, Coherent). Heterostructures of 55 nm $0.68Pb(Mg_{1/3}Nb_{2/3})O_3$-$0.32PbTiO_3$ (PMN-PT) / 25 nm $Ba_{0.5}Sr_{0.5}RuO_3$ (BSRO) were grown on $NdScO_3$ (NSO), $Nd_{0.5}Sm_{0.5}ScO_3$ (NSSO), and $SmScO_3$ (SSO) (110) substrates (CrysTec GmbH) to achieve compressive in-plane epitaxial strain of -0.5%, -0.75% and -1% respectively [55]. The PMN-PT thin film growth was carried out at an elevated temperature of 590°C in a dynamic oxygen pressure of 200 mTorr with a laser fluence of 2.0 J/cm^2 and a laser repetition rate of 2 Hz. A ceramic PMN-PT target of the same composition was used with 10% lead excess to compensate for lead loss during film growth at high temperatures. The BSRO bottom electrodes were grown with PLD using a ceramic target with the same composition at 800 °C in a dynamic oxygen pressure of 20 mTorr with a laser fluence of 1.8 J/cm2 and a laser repetition rate of 2 Hz. Following the growth of heterostructures, samples were cooled down to room temperature at the rate of 5°C/min in a constant oxygen pressure of 700 Torr.

2.1.3 YFO thin film growth

The following text is used with permission of John Wiley & Sons - Books, from ref. [3]; permission conveyed through Copyright Clearance Center, Inc.

The YFO thin films were grown using pulsed laser deposition on an Nb-doped STO

substrate using a KrF excimer laser ($\lambda = 248$ nm) with 1.3 J/cm^2 fluence and 10 Hz of repetition rate [2]. A commercial $YFeO_3$ target from Plasmaterials Inc. was used for thin film growth. The substrate was held at 900 °C and the oxygen partial pressure was kept at 10 mTorr. The as-grown thin films were cooled to room temperature under a similar partial pressure of oxygen at the rate of 20 °C/min. The YFO film with varying stoichiometry was achieved by co-deposition using $YFeO_3$ (YFO) and $Y_3Fe_5O_{12}$ (YIG) targets.

2.2 TEM lamella preparation

In this investigation, TEM samples were obtained using either mechanical polishing or the focused ion beam (FIB) method along with Ar^+ ion milling.

In the case of single crystals of PMN, PMN-10PT, and PMN-30 PT, thin TEM samples along [100] and [110] axes were obtained by mechanical wedge polishing. Sample of size 3 mm times 3 mm were cut out from the bulk single crystals and were glued on a flat TEM pyrex paddle using crystal bond on the desired orientation. It is necessary to glue the specimen on a flat surface of the pyrex paddle to avoid cracking in the sample during thinning process. Thus, the paddle was first flat polished using diamond lapping films with grit sizes of 9 and 3 μ m. Once the sample is glued on the paddle, one side was first polished using lapping films with grit size in the progression of 30 to 15 to 9 to 3 to 1 μ m and ending with 0.1 μ m. During the polishing step using films of grit size greater than 1 μ m, deionized water was utilized, while with lower grit size film, hexylene glycol (greenLube) or mixture of ethyl alcohol, propylene glycol, and isopropyl alcohol (purple tube) were used as lubricants. An optical microscope was used to examine the polished sample surface during each polishing step. A scratch-free surface should be obtained under the optical microscope at the end of all polishing steps mentioned before. After obtaining scratch free surface on one side of the sample, the orientation of the specimen was changed such that the scratched surface face up for polishing. The second side of the specimen was polished in a similar progression with a film grit size of 30 to 15 to 9 to 3 μ m. At the end of the

polishing step with 3 μ m grit size film, the sample must be thinned down to 50-70 μ m. For wedging the sample, an angle of 1° was set and sample was polished with 1 μ m lapping film. The sample was regularly monitored under the optical microscope for thickness fringes at the edge of the sample. Once thickness fringes appeared at the front edge of the sample, further polishing was performed with 0.1 μ m lapping film to obtain a scratch-free surface. At the end of this step, sample thickness of 600-800 nm was usually obtained at the front edge of the sample. Later, the specimen was glued on a Molybdenum TEM glider grid. The sample was further ion milled with Ar^+ ions to achieve a sample thickness of 5-10 nm at the edge of the sample. The milling procedure included change in ion beam voltage in progression from 2.5 to 2 to 1.5 to 1 to 0.5 and finally 0.1 kV. Each step was performed for about 20-30 min. Angles of Ar^+ ion guns were adjusted between 9-6° to minimize redeposition with minimal damage to the sample surface. Samples were also cooled to liquid nitrogen temperature to reduce the beam damage.

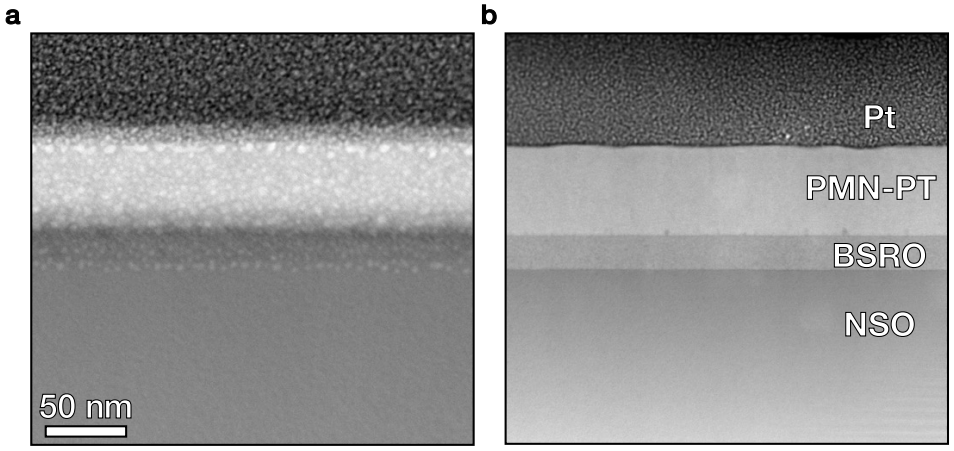

Figure 2-1: High-angle annular dark-field (HAADF) STEM image of a lamella of a heterostructure of FIB Pt/PMN-PT/BSRO/NSO (a) before and (b) after Ar^+ ion milling

Cross-sectional TEM samples from PMN-PT thin films were prepared either by mechanical polishing or focused ion beam methods. To obtain TEM samples from thin films, first, a sandwich was prepared by gluing two pieces of size 2 mm times 2 mm on the film side using M-bond or epoxy glue and kept for the curing step at optimum

curing temperature. The film sandwich was further glued on the TEM pyrex paddle using a crystal bond and polished down using the similar method described for single crystal samples. The thin wedged samples were ion milled with Ar^+ ion beam to obtain electron transparent cross-sectional samples. In the focused ion beam method, Ga^+ ions were used to obtain a TEM lamella. First, a protective platinum layer of thickness 2 μm was deposited using electron beam to protect the thin film from direct exposure with Ga^+ ions. Further, trenches were created across the protective layer to obtain a 2 μm thick lamella. The lamella was later transferred to the TEM grid using a micromanipulator. The sample was further thinned down to 100 nm in the cross section with varying beam currents from 0.23 nA to 40 pA at 30 kV. The TEM lamella was further ion milled with Ar^+ ions to obtain a sample with a final thickness between 8-15 nm. Ar^+ ion milling at 0.3 kV for 10 min was found to be necessary to obtain thin TEM lamella with minimal surface damage, as shown in Figure 2-1.

2.3 STEM imaging and spectroscopy

Scanning transmission electron microscope (STEM) has become an extremely powerful tool for materials characterization. With significant developments in aberration correctors, detectors, and spectrometers in STEM, a wealth of information about the atomic structure of materials can be determined [78]. In STEM, a focused electron beam of 1Åsize rasters across the sample to determine their projected atomic structure. A typical STEM consists of an electron gun, magnetic lens systems, and detection units. The electron sources in high-resolution STEMs are typically Schottky field emission gun (FEG), which provides a coherent electron beam with high brightness. A magnetic lens such as a condenser and objective allows demagnifying the electron beam to a finely focused angstrom-sized electron probe over an electron transparent sample. Electrons scatter through the thin samples captured by scintillator-based STEM detectors at different annular ranges to form an image. Magnetic lens in an electron microscope introduce significant spherical aberrations while electron sources lead to chromatic aberration in the electron beam. These aberrations significantly

limit the resolution of an electron microscope. With modern aberration correctors and electron sources, spherical and chromatic aberrations can be minimized significantly, allowing to achieve sub-angstrom resolution using STEM.

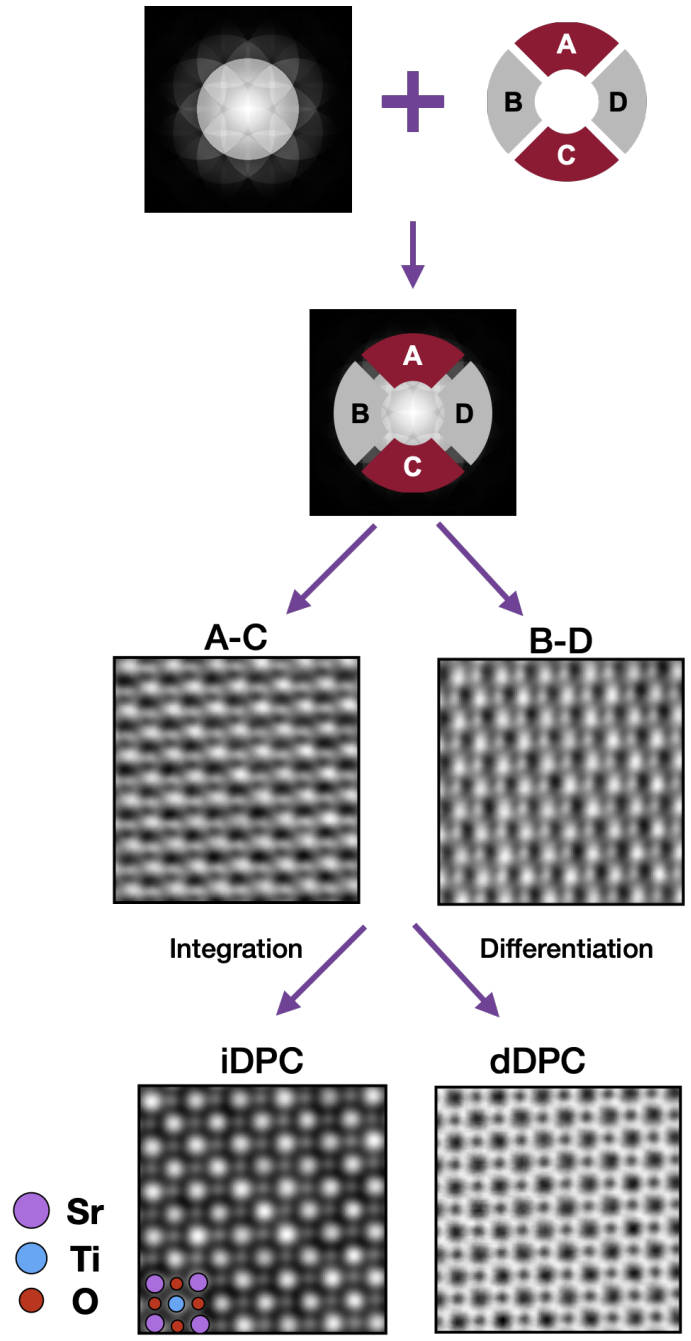

Figure 2-2: Schematics to illustrate the method to obtain DPC/iDPC/dDPC images from $SrTiO_3$

In STEM, a focused electron probe interacts with the thin, electron transparent

sample and undergoes elastic and inelastic scattering. For imaging, annulus-shaped detectors are utilized to collect these scattered electrons at different annular ranges to generate various types of images. High angle annular dark-field (HAADF) STEM images capture mostly elastically scattered electrons and provides incoherent images. HAADF image intensity varies strongly with type and the total number of scatterers along the atomic columns [79]. These images are also referred as Z-contrast images due to the scaling of their image contrast with the atomic number (Z) of elements as $Z^{1.6-1.7}$. However, these lack contrast from low atomic number elements like carbon and oxygen. Bright-field (BF), annular bright-field (ABF) and differential phase contrast (DPC) images allow imaging of both heavier and lighter elements in the structure. Primarily, an integrated or differentiated DPC signal provides higher contrast from lighter elements even in the presence of heavier atoms [80, 81]. DPC imaging is usually performed with a four-segmented detector as shown in Figure 2-2. This captures the electrons deflected in the presence of atomic potential of the sample, providing two signals, A-C and B-D [82]. These signals show direct proportionality to the electric field in the sample. By integrating these signals, iDPC images can be obtained whose contrast is directly proportional to the atomic potential of atomic columns. iDPC image has enabled imaging of low atomic number elements, including hydrogen [83], but lacks the chemical sensitivity unlike HAADF or ADF images (Figure 2-2). Differentiating the DPC signal are sensitive to the changes in charge density from atomic columns and also provides higher contrast from low atomic number elements.

In this thesis, STEM imaging was performed with a probe-corrected ThermoFisher Scientific Themis G2 80-300 kV or Themis-Z G3 60-300 kV electron microscope equipped with an extreme field emission gun (X-FEG) at 200 kV and a probe semi-convergence angles of 19.6, 18 or 25 mrad. I develop a custom python-scripting interface to automate the Thermo Fisher Scientific Velox software for image acquisition. This uses scripts to control the mouse and keyboard actions. HAADF images were collected with a semi-collection angle range of 65-200 mrad, ADF images with a semi-collection angle range of 34-205 or 25-153 mrad and iDPC/dDPC with a col-

lection semi-angle range of either 7-28 or 6-24 mrad. Simultaneous imaging of ADF and iDPC/dDPC was performed to quantify the local chemistry and structure with information about cations and anions.

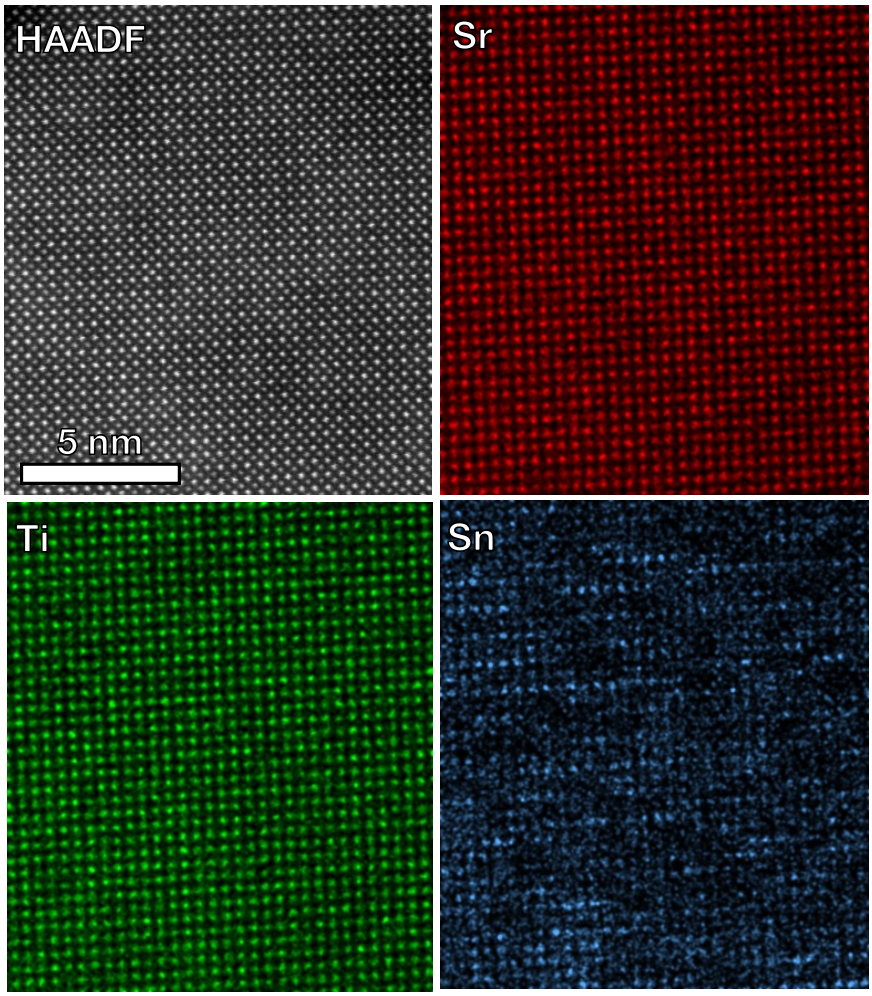

Figure 2-3: Atomically resolved STEM-EDS element map of Sr, Ti, and Sn in Sn doped $SrTiO_3$ thin films

.

Inelastic scattering of the electron beam from the sample involves generation of characteristics X-rays, characteristics electron energy loss spectra, secondary electrons, cathodoluminescence and auger electrons. Here, I will focus on the two signals used for analytical microscopy, characteristics X-rays and characteristics electron energy loss in the direct beam.

X-rays are generated when an electron interacts with the thin TEM sample. Dur-

ing electron interactions, electron energy transfers to bound electrons of atoms which excites them to occupy the higher energy levels. This excited state is unstable, leading to an outer shell electron moving to the position of the ionized electron. Such events lead to characteristic X-ray emissions. Emitted X-rays show energy as the differences between electrons at higher and lower shells. This is unique to most of the elements enabling to determine all the elements present in the sample with energy dispersive X-ray spectroscopy (EDS) with a STEM probe. For example, atomic site occupancy of Sn in Sn doped $SrTiO_3$ can be easily determined with STEM-EDS elemental maps, shown in Figure 2-3. The continuum energy X-rays are also emitted due to the deceleration of the electron beam in the presence of a local electric field from the electron clouds of the sample. These are termed Bremsstrahlung X-rays and exist as the background X-rays along with characteristic X-rays. Background subtraction is usually applied to raw X-ray signals to extract the characteristic X-ray signals. The net intensity obtained for each characteristic X-ray peak after background subtraction is further used to quantify the amount of element present in the material. Quantitative composition analysis using characteristics X-rays is usually performed using Cliff–Lorimer analysis [78]. In this, the concentration ratio of elements A and B relates to the ratio of the net intensity of characteristic X-ray peak for elements A and B by the following equation:

$$\frac{C_A}{C_B} = K_{AB}\frac{I_A}{I_B}$$

Where C_A and C_B are concentrations of elements A and B in weight percents, repectively, I_A and I_B are net intensities of characteristic X-ray peak from elements A and B, respectively, and K_{AB} is the Cliff-Lorimer factor (k-factor). The values for k-factors can be either determined using modeling calculations or experimentally using a reference sample containing elements A and B. This allows obtaining the amount of each elements in a materials in terms of weight or atomic percentages. For elemental quantification with higher accuracy using STEM-EDS, a longer acquisition time is required to obtain characteristics X-ray signal with a higher signal-to-noise ratio as

the collection efficiency of X-rays is typically low ($\sim 6\%$) with typical X-ray detectors in electron microscopes. Electron channeling also affects elemental quantification, especially at atomic resolution thus, an additional error needs to be accounted in estimating the concentration of each element.

Elemental distribution across the sample can also be determined with electron energy loss spectroscopy (EELS). This has advantages over EDS mapping due to its higher collection efficiency as it uses all the electrons in the direct beam after transmission through the specimen. These transmitted electrons get collected by the spectrometer allowing the separation of electrons based on their energy, leading to an electron energy loss spectrum. An energy loss spectra have three distinct regions, zero loss peak, low-loss, and high-loss. The zero-loss peak arises from transmitted electron without any energy loss and also includes electrons scattered by phonons. The full width at half maximum of this peak determines the energy resolution of the EELS measurements. With FEG as an electron source, an energy resolution of $\sim$ 0.8-1 eV can be achieved readily. The low-loss region is usually defined in energy loss spectrum with energy $<$ 50 eV. This contains information about surface plasmons and inter-band electronic transitions. The high-loss regions show characteristic intensity edges corresponding to the ionization energy of core-shell electrons. These edges enable the quantitative determination of the chemical distribution across the sample. First, the net intensity of characteristic edges is determined after subtracting a background which depends on energy range usually modelled by a power law dependence based on the following equation:

$$I = AE^{-b}$$

Where I represents the background intensity in the channel of energy loss E, and A & b are constants. These net intensities of characteristic edges from each elements can be used to obtain absolute quantification of concentration, N in terms of number of atoms per unit area of the specimen as follows:

$$N = \frac{I_{edge}(\beta\Delta)}{I_{zl}(\beta\Delta)\sigma_{edge}(\beta\Delta)}$$

Where, $I_{edge}(\beta\Delta)$ is net intensity of the characteristic edge, $I_{zl}(\beta\Delta)$ is the intensity of zero-loss peak, $\sigma_{edge}(\beta\Delta)$ is the partial ionization cross-section, β is the collection angle and Δ is the integration energy window to obtain net intensity of the edge. Factors such as β is fixed during an EELS acquisition, Δ usually are selected in the range of 20-100 eV and partial ionization cross-section, $\sigma_{edge}(\beta\Delta)$ is determined either using theoretical modeling (hydrogenic cross-section or Hartree-Slater model) or experimentally using a known sample as reference.

2.4 Data acquisition and processing

STEM images are usually acquired serially with a focused probe raster across the sample. These influence significantly with the sample drift, leading to large image distortions, and limiting to determine of the local lattice distortions. Revolving STEM enables correct linear sample drift with the acquisition of an image series with a 90^o scan rotation for every frame [84]. With subsequent scan rotation, the drift-induced distortions effectively rotate with every frame. These drift induced distortions are obtained from the image series by finding the linear drift rate and drift angle and finally corrected using an affine transformation. In this approach, these drift rate and angle are evaluated based on the change of at least two of the lattice vector angles with changing scan rotation as mentioned in ref. [84]. The sum of all drift and scan distortion corrected frames provide final image with high signal-to-noise ratio, enables to extract quantitative information about the atomic structure of a crystalline material.

The atom column information was extracted from the drift and scan distortion corrected images by fitting a two-dimensional Gaussian function using a custom Python script [85]. Information about atomic column intensity and position was further ar-

ranged in a matrix form enabling to easily access periodically arranged atomic columns across the sample. Such atom column indexing also allows us to find the correlations between chemistry and structure easily.

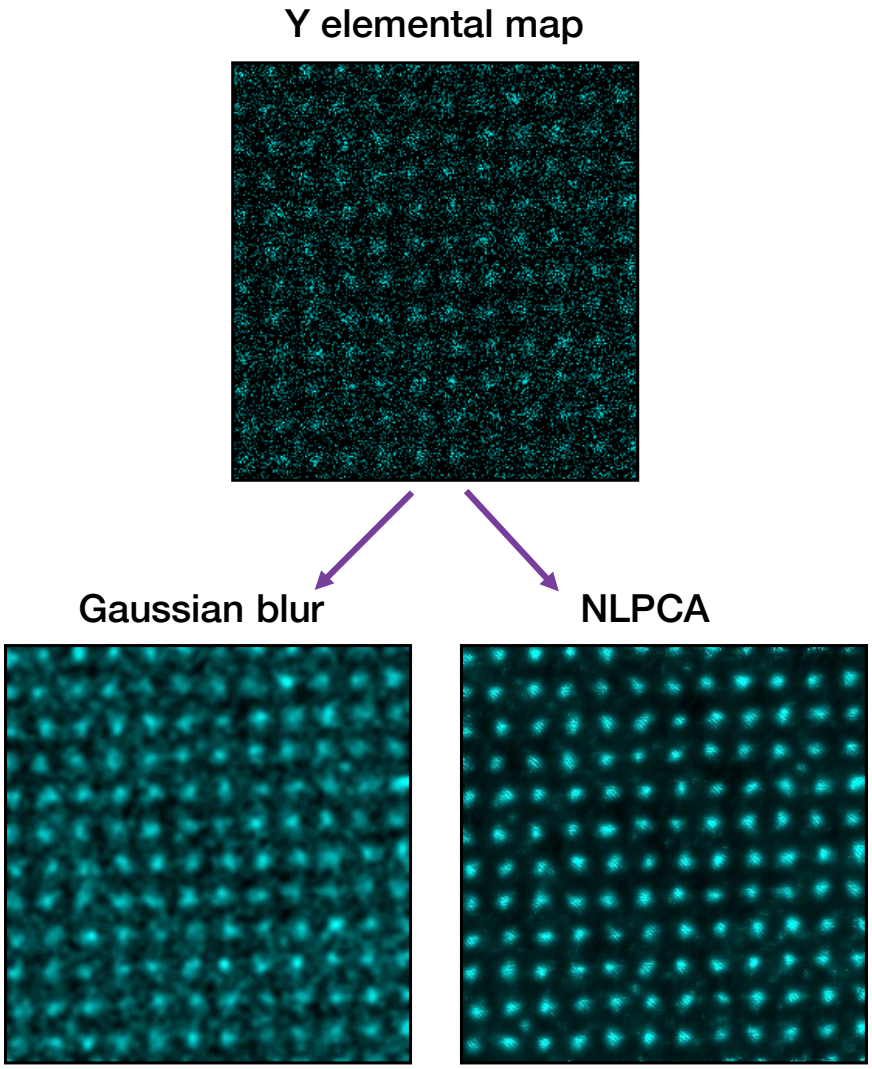

Figure 2-4: Atomically resolved STEM-EDS element map of Y in YFO thin films before and after denoising using gaussian filtering and non-local principal components analysis methods

.

As discussed before, STEM EDS elemental mapping allows finding the chemical distribution across the sample. Especially at the atomic scale, these allow finding all the elements present in each atomic column. Atomic resolution EDS data for YFO thin films (as discussed in chapter 6 was collected using either a Super-X or an Ultra-X

EDS detector on ThermoFisher Scientific microscopes. STEM-EDS signals at atomic resolution have a poor signal-to-noise ratio (Figure 2-4). Denoising methods such as gaussian filtering or non-local principal components analysis (NLPCA) can be applied to enable better inferences from such EDS maps [86]. The comparison of two denoising methods using Gaussian filtering and NLPCA on the Y elemental map, shown in Figure 2-4 indicates NLPCA to be a better method in extracting clear inferences about elemental distribution across atomic columns. In NLPCA based denoising, noisy image patches are clustered together based on their spatial structure rather than their spatial proximity, followed by removing noises from the cluster of patches using principal components analysis (PCA) and finally combining these denoised patches to form a denoised image [87]. This allows obtaining the atomically resolved image with a higher signal-to-noise ratio. But as this uses PCA based denoising approach for patches, utilizing fewer components, less than 10 had been found to create artifacts in a denoised image; thus, using a larger number of components is critical to avoid artifacts [87]. Here, the NLPCA method is applied to the EDS intensity map via an open-source Matlab script[86].

2.5 Multislice simulations

STEM image simulations enable to the comparison of the experimental images in contrast to the theoretical structural models. This also becomes a handy tool for understanding the image features which are otherwise difficult to predict due to the electron beam's complex interactions with the sample's atomic potentials. The frozen phonon multislice approach is typically used to obtain simulated STEM images [88]. In multislice simulations, the theoretical atomic structure of the sample is sliced into many periodic sections through the depth, as shown in Figure 2-5. Atomic potentials are projected over each slice which scatters the probe wavefunction. The scattered wavefunction from one slice is further propagated to the next slice with the convolution of the wavefunction with a Fresnel propagator. This process repeats until the end of the sample thickness. The final exit wave function from the sample is used

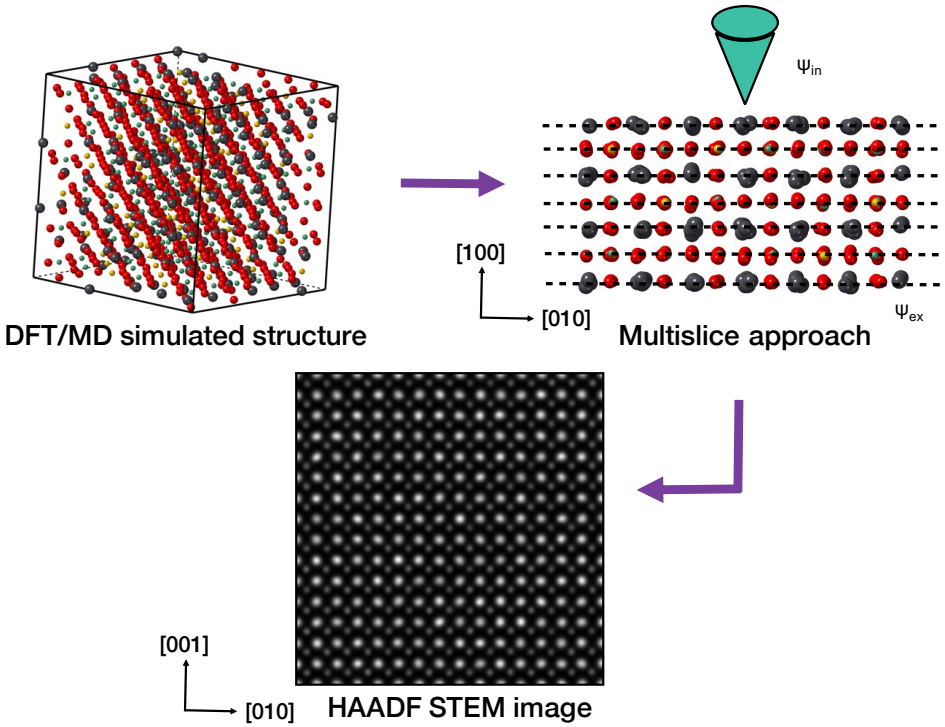

Figure 2-5: Schematics to illustrate the multislice approach to generate simulated images using DFT relaxed structure

to generate the simulated images. Various image types such as HAADF, ADF, ABF, and BF can be obtained by the summation of scattered intensity over the angular range similar to the experimental collection angle. These simulated images are based on the assumption of neutral and non-interacting atoms in the crystal structure.

The effect of imaging parameters such as aberrations and sample mistilts on STEM images can be easily studied with simulated images. Aberration effects can be added as a phase factor in the probe wavefunction. The Fresnel propagator enables to add smaller sample mistilts in the simulated images without the input of tilted structure. These simulations also account for atomic vibrations in real crystals. Random displacements in a defined range of magnitude determined from the Debye-waller factor are added to each atom. An average of multiple simulated images with each unique random displacement (thermal configurations) enable us to mimic the effect of atomic vibrations on image contrast. These images are found to be comparable to experimental STEM images qualitatively [79]. But quantitatively, the simulated images show

differences from the experimental images. Simulated images show higher contrast than the experiment. This disparity is explained by spatial incoherence arising from a combined effect of finite effective source size, instabilities, sample drift, etc. Effect of spatial incoherence is included in the simulated images by convolving them with a Gaussian envelope function with full width at a half-maximum of 80 pm [79]. This allows for the quantitative comparison of the simulated and experimental images.

Chapter 3

Origin of relaxor behavior in bulk PMN-xPT systems

Text and figures in this chapter is from ref[1] and reproduced with permission from Springer Nature as cited, "The author of articles published by Springer Nature do not usually need to seek permission for reuse of their material as long as the journal is credited with initial publication. Ownership of copyright in original research articles remains with the Author, and provided that, when reproducing the contribution or extracts from it or from the Supplementary Information, the Author acknowledges first and reference publication in the Journal".

The main objective of this chapter is to determine the structural and chemical origins of relaxor ferroelectric properties in PMN-xPT (x=0, 10, and 30). Through a combination of ADF and iDPC aberration corrected STEM, the projected positions of cation and anion sub-lattices are used to measure the subtle features of nanoscale polarization in these materials. The projected polarization reveals the presence of nanoscale domains that are consistent with the polar slush model. The distribution of chemical and structural heterogeneities is quantified as a function of Ti content, and a direct correlation is found between the spatial distribution of chemical/structural heterogeneities and polarization domain walls. The heterogeneities are found to inhibit polarization rotation, leading to the formation of low-angle domain walls. The presence of monoclinic-like distortions explains the composition-dependent electrome-

chanical response. In combination, these results provide evidence for the underlying mechanisms responsible for yielding relaxor behavior and their electromechanical coupling behavior.

In this study, the bulk PMN-xPT (x=0, 10, and 30) samples were provided by Prof. Shujun Zhang at University of Wollongong, Wollongong, Australia. The density functional theory calculations were performed by Dr. Jonathon Baker and Dr. Preston Bowes under the guidance of Prof. Douglas Irving at North Carolina State University, Raleigh, North Carolina, United States of America.

3.1 Mapping nanoscale polarization variation

As discussed in chapter 2, unlike ADF STEM images, iDPC can capture both cation and oxygen atom column positions, as shown in Figure 3-1a. Using iDPC STEM, the projected polarization is measured along $\langle 1\bar{1}0 \rangle$ projection as the difference between the cation and anion center of masses, across ten different sample locations. It is important to note that along the PMN-xPT $\langle 1\bar{1}0 \rangle$ projection, lead(Pb) and oxygen(O) atoms overlap. To evaluate the relative impact of Pb/O atom column displacements, iDPC images are simulated with and without displacement of Pb and O separately. With 10pm O displacements, the Pb/O atom column center shift is minimal (< 1 pm). In contrast, a 10 pm Pb displacement leads to the significant displacement ($\sim$10 pm) of the Pb/O atom columns center as shown in Figure 3-2. We thus conclude that these positions are almost entirely dominated by Pb. The net projected polarization is then calculated as the difference in the center of mass of cations atom columns (Pb/O and Mg/Nb/Ti) from the center of mass of anions (O) in a double perovskite unit cell in $\langle 1\bar{1}0 \rangle$ projection.

Projected polarization is evaluated on approximately 5,000 unit cells at each of the three PMN-PT compositions. The high sampling of each composition provides a statistical representation of the underlying structure of the material, aiding in connecting the results presented here to prior diffraction studies. Calculating the center of mass difference between the cations and anions using iDPC STEM, Figure 3-1c

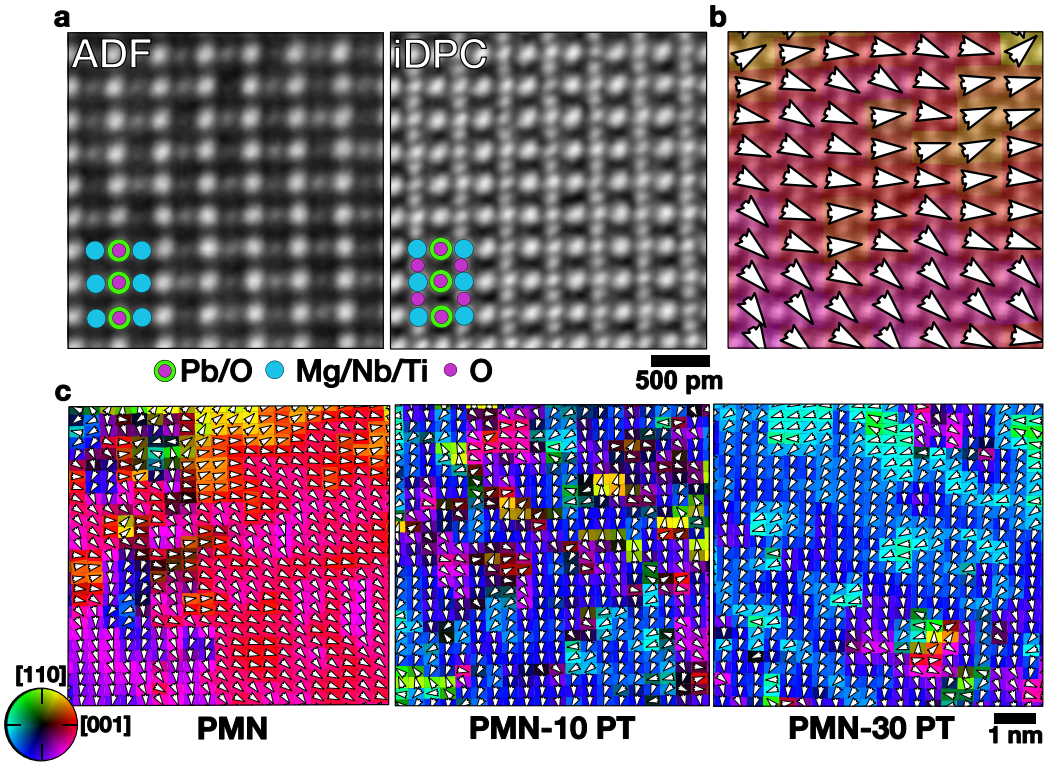

Figure 3-1: (a) Simultaneously acquired ADF and iDPC images of PMN along the $\langle 1\bar{1}0 \rangle$ projection with the (b) projected displacement (polarization) map from iDPC. (c) Projected displacement (polarization) for PMN-xPT (x=0, 10, and 30) unit cells in representative iDPC images. The projected displacement(polarization) magnitude ranges from 1 to 20 pm, and is indicated by luminosity. From Ref[1] and reproduced with permission from Springer Nature.

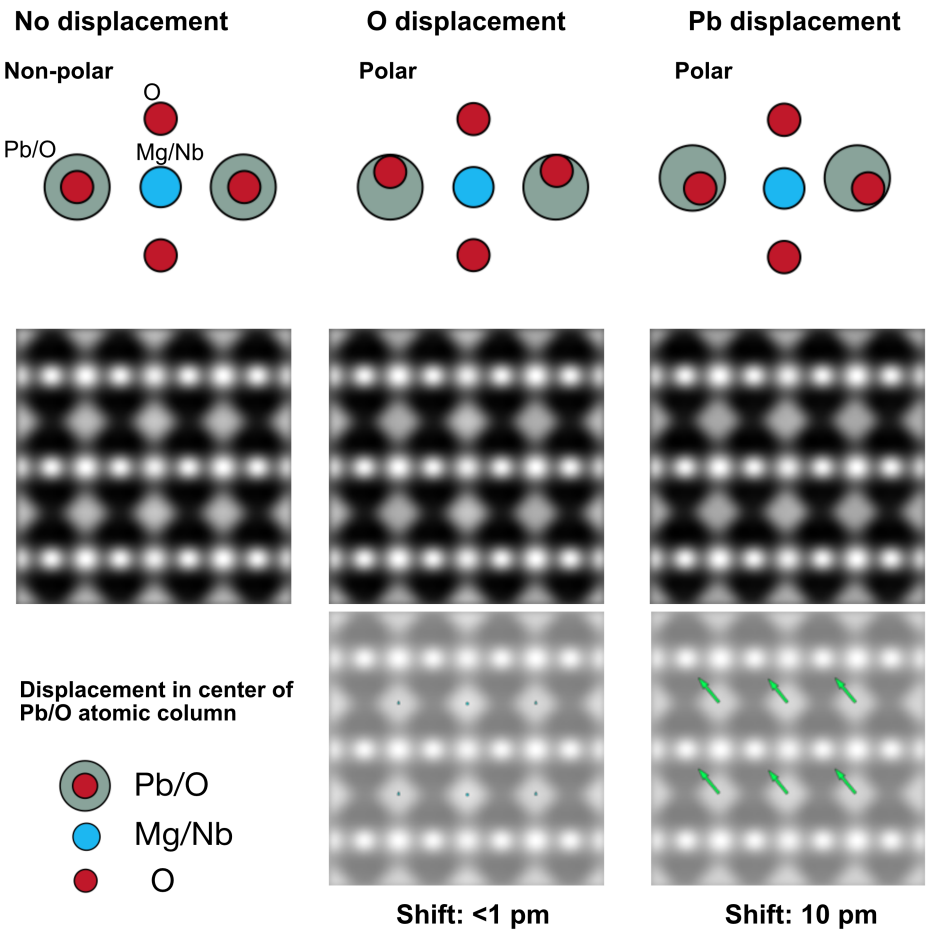

Figure 3-2: Simulated iDPC images with (a) no displacements, (b) 10 pm O displacements, and (c) 10 pm Pb displacements. From Ref[1] and reproduced with permission from Springer Nature.

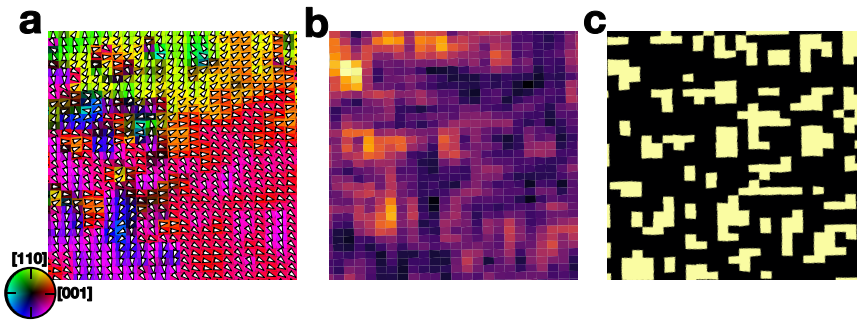

Figure 3-3: (a) Polarization map in PMN, (b) Standard deviation of polarization, and (c) local maxima map determined using Sato filter. The local maxima correspond to domain walls and are highlighted as yellow blocks. From Ref[1] and reproduced with permission from Springer Nature.

shows representative projected polarization maps for PMN, PMN-10PT, and PMN-30PT imaged along $\langle 1\bar{1}0 \rangle$. The projected polarization exhibits regions with similar magnitude and direction, i.e. polar domains, that vary smoothly across each image. Notably, for PMN, the observed polar domains do not decay to a non-polar background, which contrasts with the polar nanoregion model that assumes a non-polar matrix. These nanoscale domains vary in size from 2-12 nm and form a high density of domain walls between them. This observation is also remarkably similar to the reverse Monte Carlo analysis of diffraction data [28].

Further, domain wall angles are calculated from polarization maps across the datasets. Domain walls are defined as regions where maximum variation of the polarization occurs, for example in Figure 3-3a. To locate these domain walls, the standard deviation of the local 3×3 unit cell projected polarization magnitude is determined. The resulting standard deviation map, Figure 3-3b, exhibits local maxima that correspond to regions of greatest polar direction variation and thus the domain walls. A Sato filter[89] is then applied to accentuate curvilinear structures. Subsequently, a median threshold is applied to the Sato filtered image to generate a binary mask that can be used to locate domain wall centroids, as shown in Figure 3-3c. After locating the domain walls using the Sato filter-based maximum polarization variation approach, the domain wall angle is evaluated as the maximum change in polarization angle between each domain wall unit cell and its first nearest neighbor. The minimum

domain wall angle observed here is ≈2° for all the samples. The domain wall angle distribution is evaluated by binning every 5° starting with bin 0-5°.

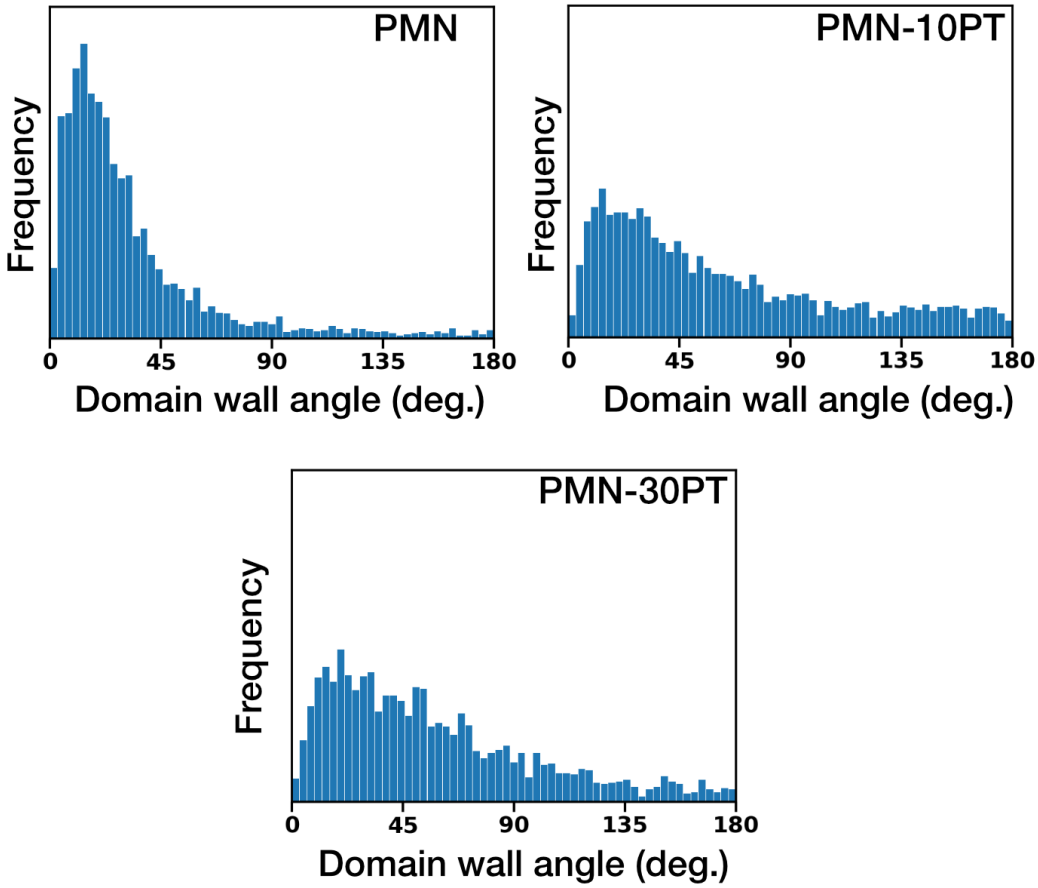

Figure 3-4: Domain wall angle distribution for PMN-xPT (x = 0, 10, and 30), with a minimum observed domain wall angle of ≈2°. From Ref[1] and reproduced with permission from Springer Nature.

In PMN, a significant majority (72%) of the domain wall angles are in the range of 10-35° as shown in Figure3-4, which is in agreement with predictions from the polar slush model [13, 55]. As the fraction of PT increases, the average domain wall angle increases, reflecting the onset of ferroelectric behavior. This behavior leads to the mixed relaxor and ferroelectric properties found in PMN-PT materials and is expected from the polar slush model [13, 55]. This model does not, however, incorporate the specific structure and chemistry details that drive the formation of the polar domains.

3.2 Quantifying the types of local order

3.2.1 Chemical order

Chemical ordering is revealed in the ADF STEM data, as shown in Figure 3-5a, left. Clustered oscillation of B sub-lattice atom column intensity on (111) planes indicates a doubled perovskite lattice where occupancy of Mg and Nb vary systematically. The weaker normalized intensity atom columns (blue) contain more Mg or Ti (β_I), while those stronger intensity atom columns (red) contain more Nb (β_{II}).

To locate the chemically ordered regions (CORs) regions, a correlation method is employed as shown in Figure 3-6. First, the B sub-lattice intensity data is normalized with the 3×3 unit cell local average. The image average intensity is then subtracted (Figure 3-6a, b). The absolute value of the correlation coefficient between this image and a 3×3 template pattern, such as in Figure 3-6b, is then calculated. For example, the absolute correlation coefficient map of B sub-lattice intensity reveals regions of chemical ordering as shown in Figure 3-6c. To quantify the area fraction of ordered regions, a binary mask is generated, a method as shown in Figure 3-6d-f. Finally, the area fraction is determined as the ratio of masked unit cells to the total number of unit cells in the image.

At each composition, the CORs are found throughout and account for 39±1% of the total projected area in the case of PMN, 37±2% for 10% of PT, and only 11±1% for 30% PT. The decreasing chemical order with increasing Ti is in agreement with previous X-ray and neutron scattering results where superlattice reflection intensity also decreases as the composition approaches the MPB [15, 45]. Recently, Krogstad suggested the presence of anti-ferrodistortive displacements based on diffuse scattering features, i.e. Pb displaces in the opposite direction of its B sub-lattice neighbors [15]. The chemical and spatial origins of this behavior could not, however, be unambiguously determined. When the oxygen atom columns are not considered in iDPC STEM data (similar to X-ray diffraction), the chemically ordered regions (CORs) exhibit Pb-atom-column anti-ferrodistortive displacements with respect to the B sub-lattice, as shown in Figure 3-7. Here, anti-ferrodistortive displacements of

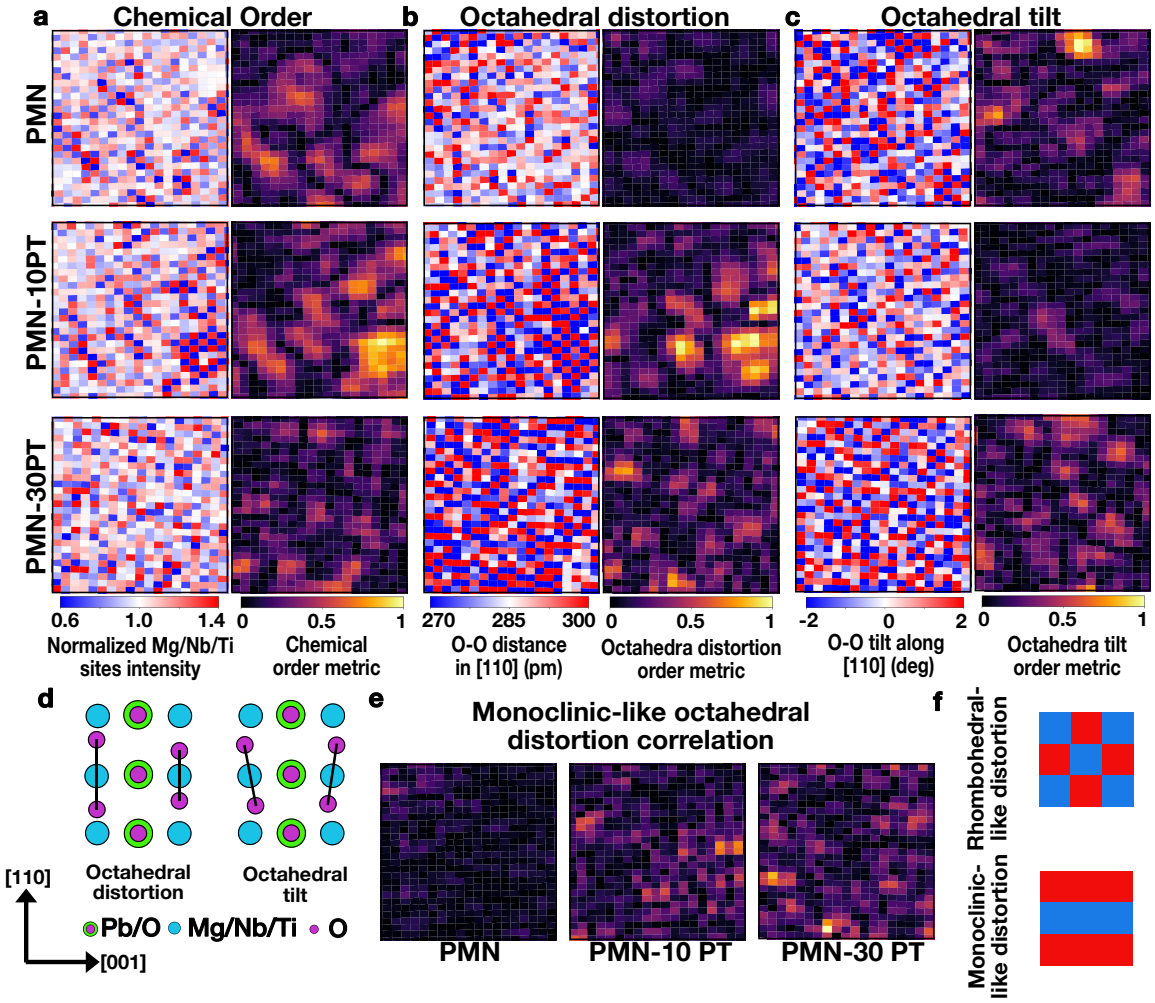

Figure 3-5: Spatial distribution of structural and chemical heterogeneities, (a) chemical order, (b) octahedral distortion, (c) octahedral tilt, (d) schematic of distortion types and their corresponding O-O patterns, (e) monoclinic-like distortion analysis, and (f) schematic patterns of rhombohedral-like and monoclinic-like distortion. From Ref[1] and reproduced with permission from Springer Nature.

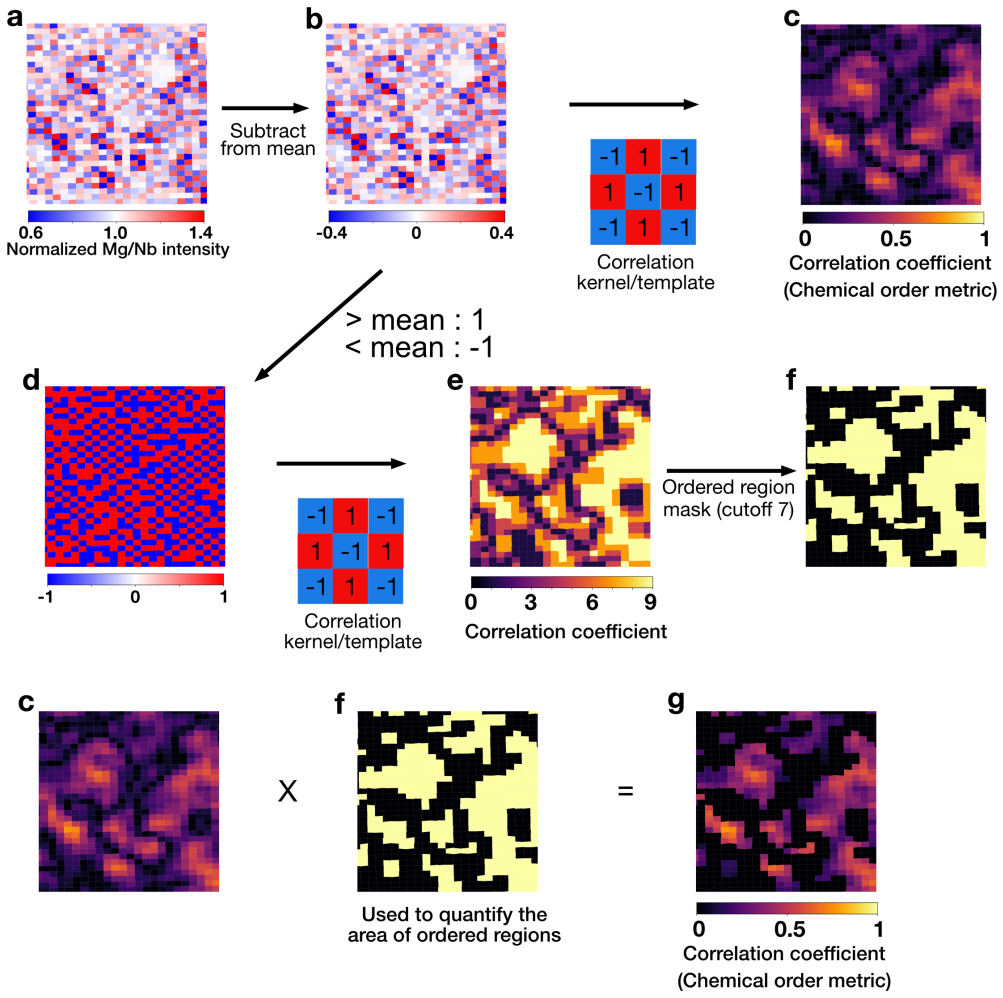

Figure 3-6: Schematic of the method used to determine the order metric and area of ordered regions in PMN. From Ref[1] and reproduced with permission from Springer Nature.

Pb is defined based on the region where nearest neighbor Pb atoms show displacement in opposite direction with respect to each other, eventually, leading to a decrease or cancel the local net Pb displacements. This is in agreement with the X-ray and neutron scattering features that are thought to originate from the anti-ferrodistortive displacement of Pb atoms that decreases with an increase in PT composition [15]. The STEM results are in agreement with this hypothesis as the CORs decrease with increased PT content.

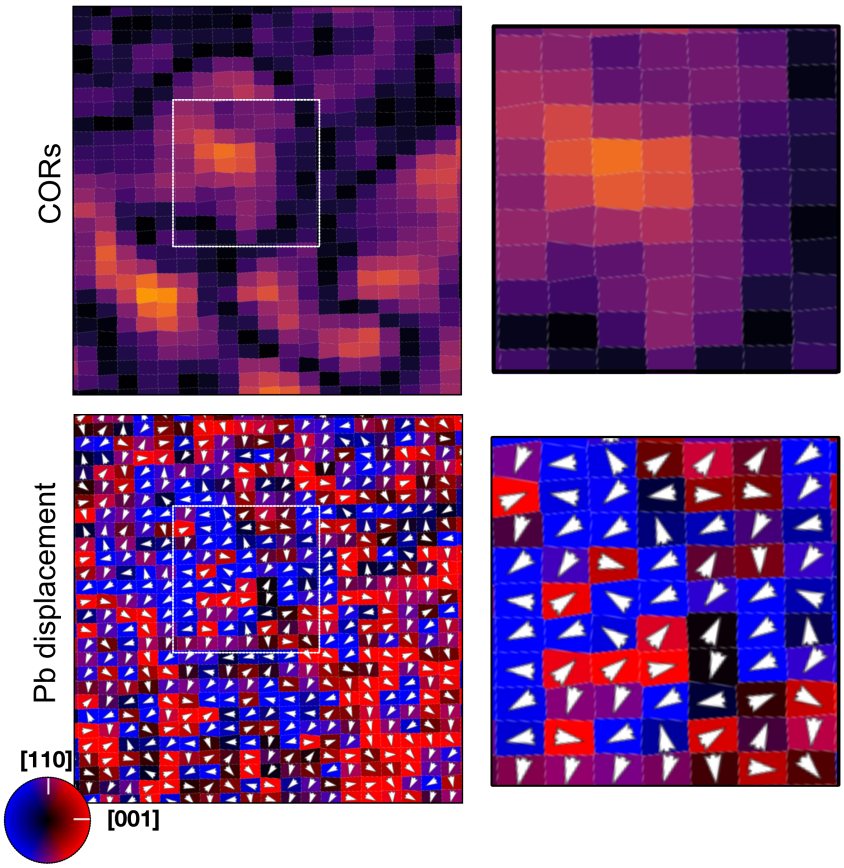

Figure 3-7: Anti-ferrodistortive Pb displacements occurring at CORs. From Ref[1] and reproduced with permission from Springer Nature.

3.2.2 Octahedral distortion and tilt order

As noted from recent X-ray and neutron scattering experiments, oxygen displacements may hold the key to understanding structure-property relationships in Pb-based relaxors [15]. To this end, oxygen octahedral distortion (expansion/compression) and tilting (schematically shown in Figure 3-5d) are determined from iDPC images, as in Figures 3-5b-c. At each composition, distortion and tilting exhibit local ordering, reminiscent of the CORs.

Similar correlation analysis for chemical order is used to determine the area fraction of octahedral distortion regions (ODRs), as shown in Figure 3-5b. In PMN, 21% of the projected area exhibits distortion ordering, with 63% overlapping the CORs and 27% at the COR boundaries.The overlap of the CORs and ODRs highlights the spatial correlation between octahedral distortion and chemical ordering. As PT con-

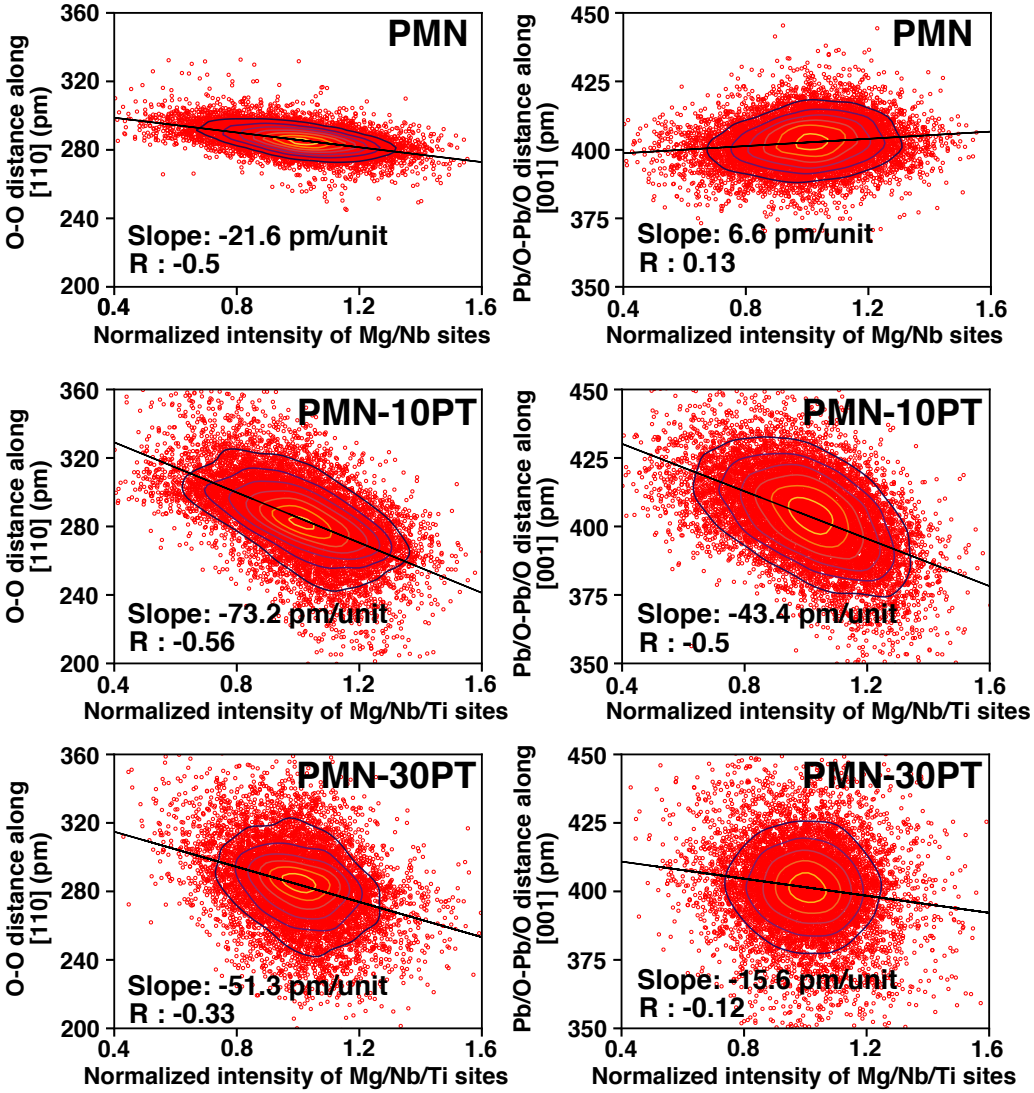

Figure 3-8: Correlation between the Mg/Nb/Ti normalized atom column intensity and the O-O distance along [110] or Pb/O-Pb/O distance along [001] as indicated. From Ref[1] and reproduced with permission from Springer Nature.

tent increases, the ODRs increase to 28% for PMN-10PT. Furthermore, a similar checkerboard octahedral distortion pattern is predicted for the chemically ordered PMN from density functional theory (DFT) [1].

At PMN-30PT, however, the distortion order changes. Rather than exhibiting the rhombohedral-like, checkerboard distortion pattern (see Figure 3-5f), the distortion becomes predominately striped on (110) planes, which indicates the formation of monoclinic-like unit cells as verified with STEM image simulations and agrees with prior diffraction studies [16]. The area fractions of rhombohedral- and monoclinic-like distortions were determined by use of the correlation analysis approach as discussed before. As Ti content increases so too does monoclinic-like distortion as shown in Figure 3-5e. Moreover, this type of local planar distortion should give rise to asymmetric diffuse scattering [90]. Importantly, Krogstad [15] found that the oxygen-mediated asymmetric diffuse scattering in neutron scattering was the only feature linked to the piezoelectric properties. The results presented here confirm that oxygen displacements are key and they originate in monoclinic-like regions. It is also important to note that due to the presence of gradients in local chemistry and structure, pure phases (rhombohedral or monoclinic) are not observed. From this, one can argue that such strong local structural variations and short correlation lengths give rise to local triclinic symmetry, which can facilitate the free rotation of polarization by small angles. This finding further supports the polar slush model's description of relaxors.

Beyond expansion and contraction, the oxygen octahedra also tilt with respect to [110], as shown in Figure 3-5c. Applying similar correlation analysis as for chemical order, 19% of the total projected area exhibits octahedral tilt ordering in PMN. Analysis of the B sub-lattice atom column intensities in and around these octahedral tilt regions (OTRs) shows that the atom column intensities are normally distributed. Thus the OTRs do not occur at the interior of the CORs, but that they form in close proximity to the boundary between CORs. Furthermore, these regions are rich in magnesium, as exhibited by the shift in mean column intensities towards lower values (Figure 3-10). Taken together with the DFT-determined bond length distributions, these findings suggest a mechanism for the OTRs. Specifically, Mg-O bond lengths

are much more strongly conserved than Nb-O bond lengths. As a result, Mg-O-Mg bonded octahedra would be more likely to tilt rather than stretch. Moreover, because Mg-O-Mg bonds can only exist in regions that are not chemically ordered , such tilting is expected to be especially pronounced in transition regions due to the change in local chemistry.

The anti-phase tilt pattern suggests the presence of local rhombohedral, $R3c$ local symmetry.[91] With increasing PT, the OTR area decreases from 11% to 5% for 10PT and 30PT, respectively. As the fraction of these features decreases with composition, their disappearance also explains another distinct diffuse scattering contribution noted by Krogstad that had both temperature-dependent and independent components. While the temperature-independent contribution is thought to originate from the CORs, the temperature-dependent part then arises from the octahedral tilt ordering that is disrupted by thermal fluctuations. The intensity of this type of diffuse scattering is found to decrease with PT content and follows the same trend as OTRs quantified from STEM.

3.3 Relating local chemistry and structure

Combining the ADF and iDPC STEM data, the change in B site chemistry measured with the Mg/Nb/Ti atom column intensity is also found to correlate to the O-O neighbor distance, as shown in Figure 3-8. In each case, the B sub-lattice intensity is negatively correlated with the O-O atom column distances [92].This shows that Mg/Ti expands the local oxygen sub-lattice, while Nb leads to contraction, which is consistent with the prior reports.[28, 93, 94]. In combination with the response of oxygen at the MPB where the O-O spread increases, the observed correlation indicates the key role of Ti to disrupt the lattice to stabilize the monoclinic-like distortion and increase the piezoelectric coefficient. The Pb/O-Pb/O atom column distances, in comparison, show a weak-to-no correlation with variation in B-site chemistry in PMN as shown in Figure 3-8, likely due to the dominant contribution of Pb on the observed atom column positions as discussed before.

PMN-10PT, in contrast, exhibits moderate, negative correlation as shown in Figure 3-8. At the MPB, PMN-30PT, significantly larger distortions are observed that correspond to the increased polarization and piezoelectric coefficient. This correlated structural variation in Pb displacement also explains the diffuse scattering feature found by Krogstad that correlates to the cation size mismatch. Furthermore, the above mentioned correlation is significant as nearly ≈10,000 atom columns are used in the analysis.

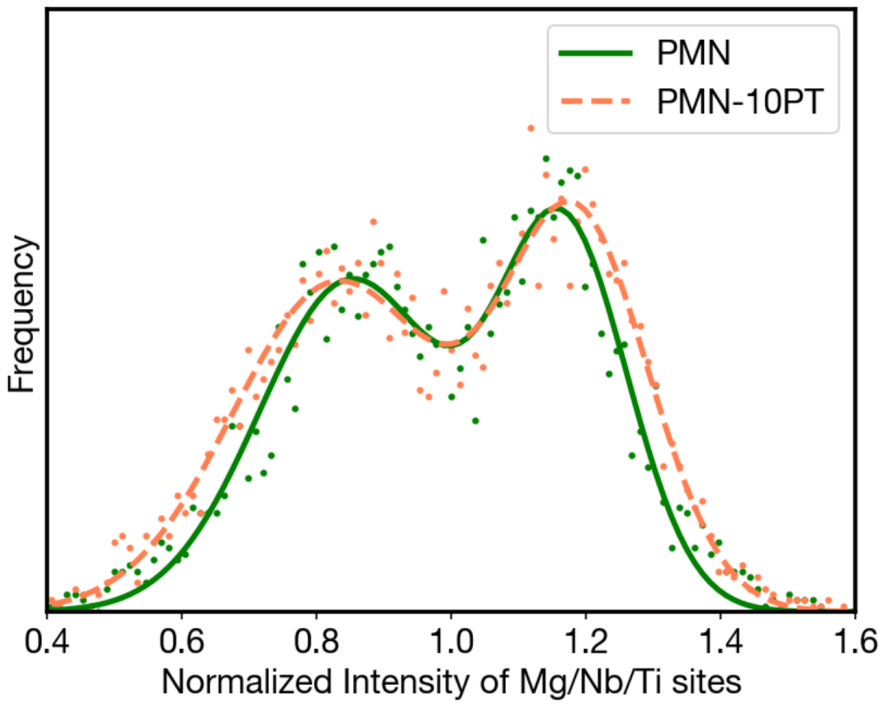

Figure 3-9: Distribution of Mg/Nb/Ti sub-lattice normalized intensity in the chemically ordered region in PMN and PMN-10PT. From Ref[1] and reproduced with permission from Springer Nature.

The distribution of Mg/Nb/Ti atom column intensities in the CORs varies with PT content. In contrast to PMN, for PMN-10PT the β_I normalized atom column intensity (0.84) is lower while β_{II} (1.18) higher, as shown in Figure 3-9. The atom column contrast in these regions thus increases compared to PMN. The intensity distribution of Mg/Nb/Ti sites in CORs, OTRs, and overlapping CORs and OTRs (CORs+OTRs) are mapped as a function of Ti content in Figure 3-10. Here, each

distribution is normalized with a total number of sampling points for each sample separately. This allows for the comparison of the distributions across samples differing in Ti content. The intensity distributions illustrate the decrease of CORs and OTRs in PMN-30PT as compared to those in PMN. Additionally, disordered regions are shown to increase for PMN-30PT as compared to PMN. Finally, octahedral tilt ordering is shown to be favored in the chemically disordered regions as OTRs exhibit a single peak.

Further analysis of the PMN-10PT β_I and β_{II} normalized intensities (Figure 3-9) also reveals that their intensity difference is enhanced with the introduction of Ti. This suggests that Ti initially replaces Nb in the mixed β_I sites of the CORs leading to a concomitant decrease in intensity for those atom columns and increased image contrast. The preferential incorporation of Ti to the CORs can be explained by the bond length preferred by titanium atoms as explained using DFT [1].

3.4 Linking polarization and heterogeneity

The heterogeneity distribution is also found to link directly with the local variation in polarization and domain walls. First, the inhomogeneity centers are obtained by finding the local maxima in the correlation map using the scikit-image python package, without adjusting any parameters between the inhomogeneity types. This approach is used to locate the inhomogeneities as their correlation values are not discrete, but they do exhibit distinct maxima that are sparsely distributed. An example is shown in Figure 3-11 for CORs in PMN. The distance between these inhomogeneity centers and the nearest domain wall is then calculated. From these distances, a first nearest neighbor cumulative distribution function (CDF) was constructed as shown in Figure 3-12. For the experiment, nearly 100% of the inhomogeneities occur within 2 unit cells of a domain wall in each composition.

To determine the significance of this observation, consider the null-hypothesis that heterogeneities are randomly distributed with respect to polarization. Taking 10,000 random sets of data equivalent to the experiment, but with random heterogeneity

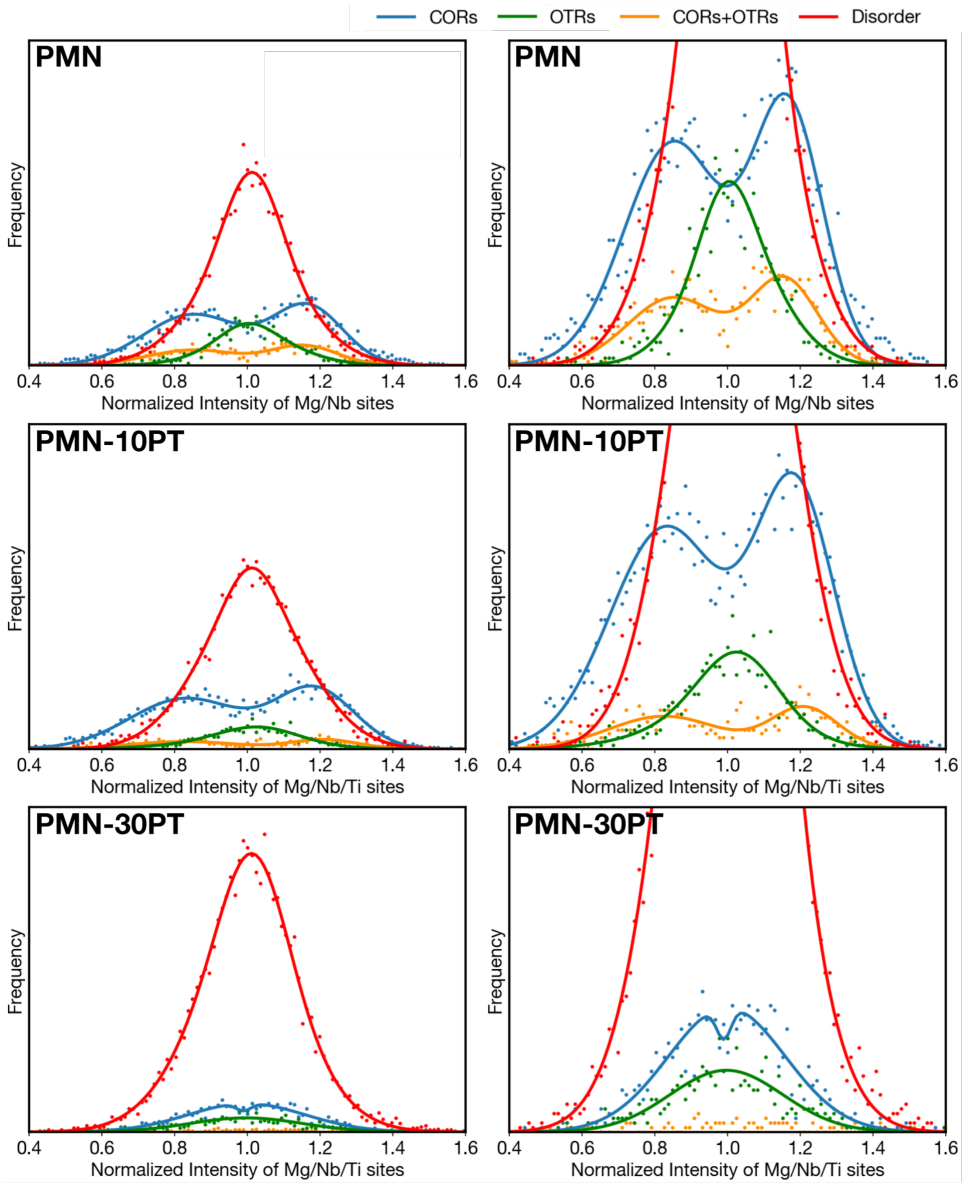

Figure 3-10: Distribution of normalized intensity of Mg/Nb/Ti sites in CORs and OTRs in PMN, PMN-10PT, and PMN-30PT. The figures on the right are rescaled versions of left to highlight the CORs, OTRs, and CORs+OTRs. From Ref[1] and reproduced with permission from Springer Nature.

locations, the 95% threshold is not reached until a distance two times larger than the experiment, see Figure 3-13d. Further highlighting the difference, the error bars indicate the maximum and minimum 95% distances for the 10,000 datasets at each composition. A result similar to the experiment is not found in any of the random data, indicating that p is significantly less than 0.05, safely discounting the null hy-

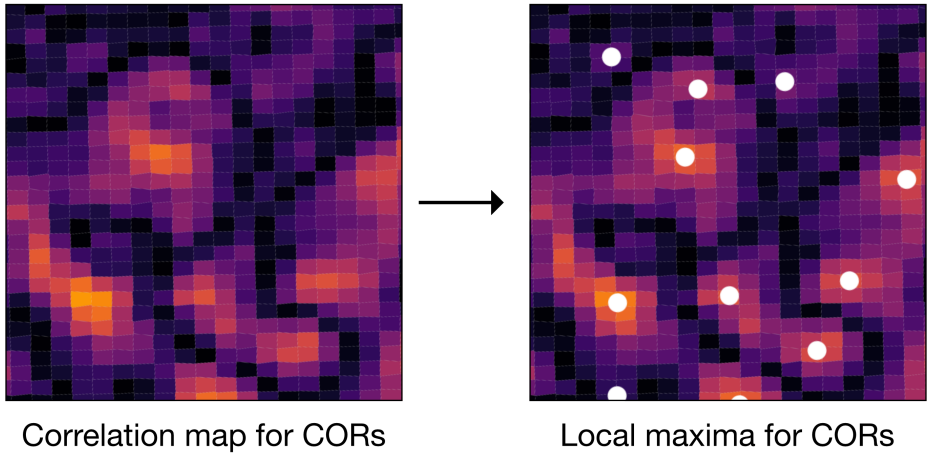

Figure 3-11: Example process of using a correlation map to locate the core of each inhomogeneity. From Ref[1] and reproduced with permission from Springer Nature.

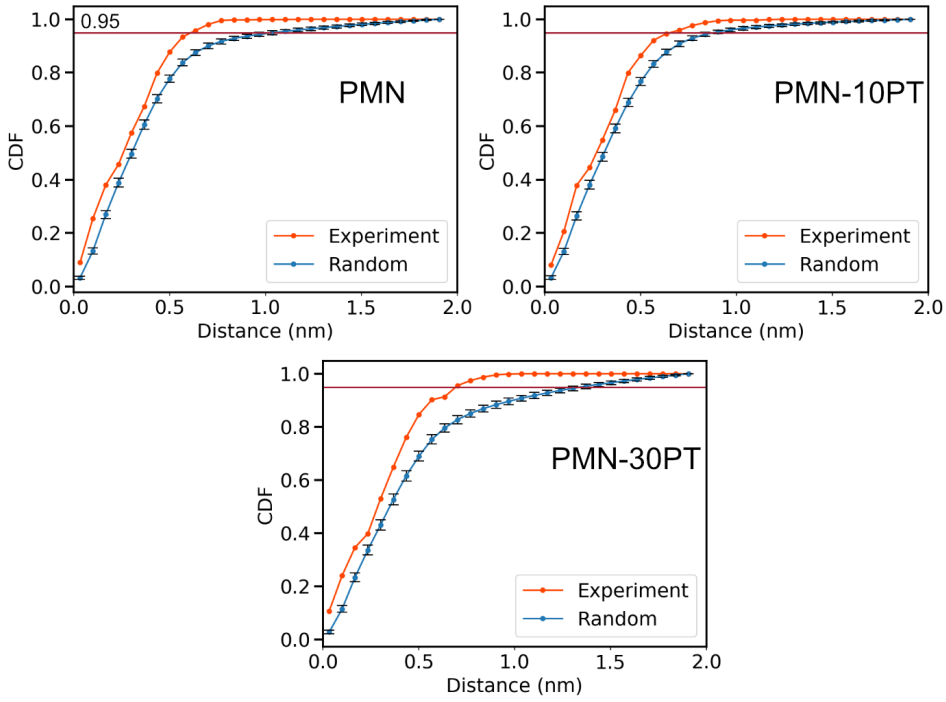

Figure 3-12: Cumulative distribution functions for nearest neighbor distances between local inhomogeneity maxima and domain walls. From Ref[1] and reproduced with permission from Springer Nature.

pothesis. As shown in Figure 3-13d, 95% of the heterogeneities are within a distance of 1.5-2 unit cells of the nearest domain wall regardless of PT content. Across the composition range investigated, 1/3 of CORs, 1/3 ODRs, and 1/3 OTRs are within

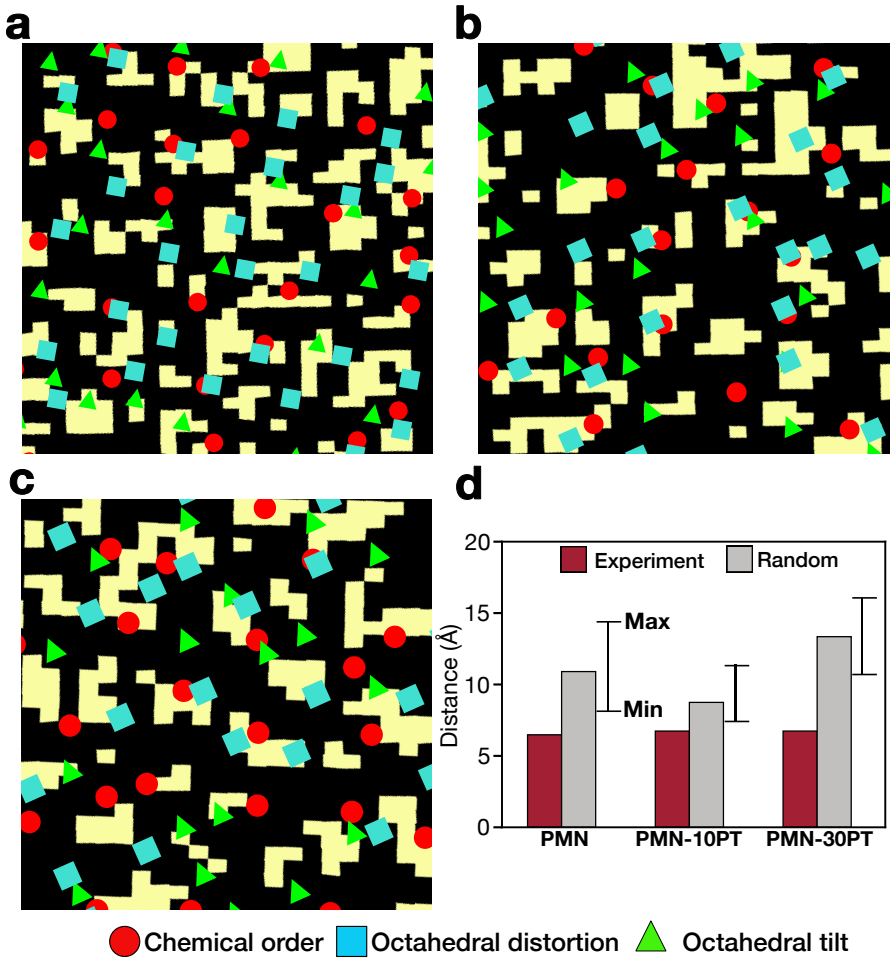

Figure 3-13: Positions of CORs, ODRs, OTRs, and domain walls for (a) PMN, (b) PMN-10PT, and (c) PMN-30PT. (d) Nearest distance between 95 % of heterogeneities maxima (random points) and domain wall for each PMN-xPT composition. Domain walls occur in the blocked, yellow regions. From Ref[1] and reproduced with permission from Springer Nature.

this distance of the domain walls. In addition, 1/3 of the domain walls have at least two nearby structural or chemical ordering types. This indicates that the polar domain walls cannot be explained by a single type of heterogeneity, but requires the consideration of all features identified. Taken together, the results presented here unambiguously reveal that chemical and structural heterogeneities are not randomly distributed with respect to polarization, but instead act as the mechanism to disrupt the formation of long-range polarization. Although this role of heterogeneity has been postulated[22, 95], its connection to generating low-angle domain walls has not been directly observed until now.

3.5 Conclusion

Direct quantification of cations and anion atom columns from STEM can reveal key relationships between polarization, structure, and chemistry in the prototypical relaxor ferroelectric system, PMN-PT. The presence of nanoscale domains exhibiting low-angle domain walls is in agreement with the recently proposed polar slush model[13]. The formation of nanoscale polar domain walls arises from the presence of short-range chemical and/or structural heterogeneity, which act to disrupt the long-range polarization. The introduction of Ti decreases the type and number of heterogeneities, which leads to cooperative alignment of polarization while also increasing the fraction of monoclinic-like distortion that enhances the piezoelectric coefficient.

Chapter 4

Chemical distribution and polar structure evolution in PMN-PT relaxor thin films

The main objective of this chapter is to determine the local chemical distribution and its role in polar structure evolution in PMN-PT relaxor thin films using scanning transmission electron microscopy. Epitaxial PMN-PT thin films grown with pulsed-laser deposition (PLD) show variation in nanoscale polar structure across the film. The evolution of polar structure correlates directly with the local chemical variation on the Mg/Nb/Ti sublattice as determined with imaging and spectroscopy. Further, the spatial distribution of inhomogeneities such as chemical, octahedral distortions, and tilt-ordered regions as found in bulk PMN-xPT (discussed in Chapter 3), are quantified across the thickness. Such inhomogeneities had been shown to be spatially correlated with polar domain walls in the case of the bulk PMN-xPT thus, indicating their influences on thin film polar structure. The local chemical distribution and structural changes during layer-by-layer growth in relaxor thin films are found due to the balance of epitaxial strain from the substrate and the chemical pressure. Further, critical thickness to stabilize relaxor behavior is determined. PMN-PT thin films grown with varying thickness show diminishing relaxor behavior and completely vanishes for 5 nm film. A decrease in out-of-plane and an increase in in-plane po-

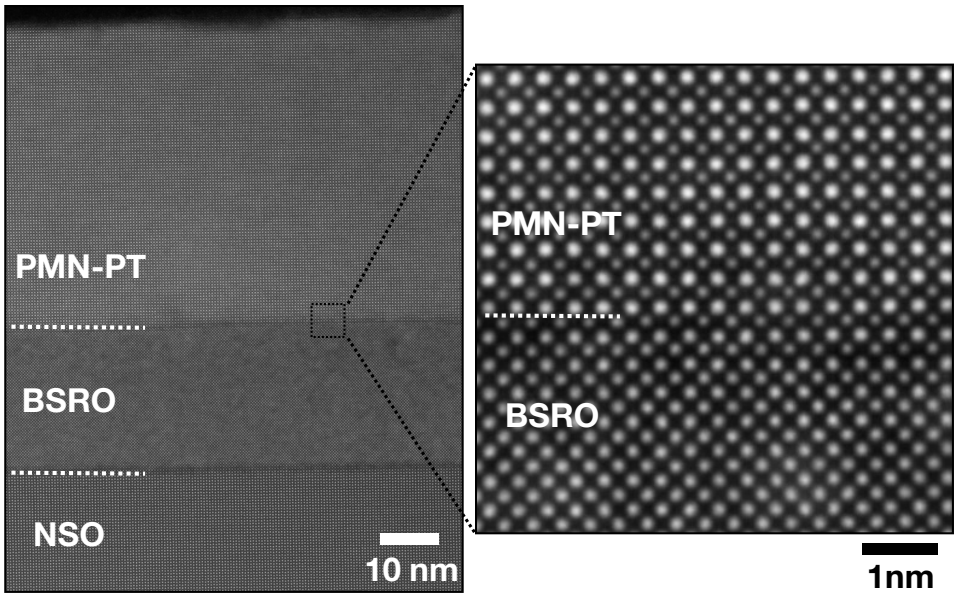

Figure 4-1: ADF STEM image of a heterostructure of PMN-PT/BSRO/NSO revealing defect-free epitaxial PMN-PT thin film with the bottom BSRO electrode

lar correlations with lower thickness relates to decreasing relaxor behavior along the growth direction. A mechanism based on the domination of random fields from local chemical variation and surface effects at lower thickness is proposed. Such atomic-scale understanding of relaxor thin films with varying thickness allows for engineering this compositionally complex system with desired chemistry and properties in the thin film form.

In this study, the PMN-PT thin films with thicknesses 5, 10, 25 & 55 nm were provided by Dr. Jieun Kim and Prof. Lane Martin at the University of California, Berkeley. The measurements of polarization with the applied electric field for PMN-PT thin films were performed by Dr. Jieun Kim under the guidance of Prof. Lane Martin.

4.1 Polar structure evolution

The structure of PLD-grown PMN-PT thin film heterostructure is determined using STEM imaging. Annular dark field (ADF)-STEM imaging of the cross-section of PMN-PT thin film heterostructures reveals that the PMN-PT films are grown

epitaxially with 25 nm of $Ba_{0.5}Sr_{0.5}RuO_3$(BSRO) bottom electrode/ $NdScO_3$ (NSO) substrate as shown in Figure 4-1. Misfit dislocations are not observed across the film, indicating a stable film structure with an in-plane -0.5 % compressive strain due to lattice misfit between film and the substrate. Simultaneous ADF and iDPC imaging were performed to obtain the intensities and positions of atomic columns of both cations (Pb, Mg/Nb/Ti) and anions (O). As discussed in chapter 3, polar displacements are calculated using iDPC images as the difference of the center of masses of atomic columns of cations with respect to the anions on a unit cell basis. The polarization (net displacement) map from the thin film reveals variation in polar structure across the thickness, as shown in Figure 4-2a. Polar ordering also shows the directional dependence across the film.

To determine the directional dependence of polar structure variation across the film, polar vector components are calculated along two perpendicular directions: out-of-plane (film growth direction [001]) and in-plane (parallel to the substrate [010]). The out-of-plane component map shows significant spatial variation across the thickness (Figure 4-2b), while the in-plane component map shows the minimal difference (Figure 4-2c). Out-of-plane polar domains show alternate polarity where negative direction (pointing downward towards the substrate) is marked with blue and positive direction (upward, away from the substrate) is marked with red. Three distinct 5, 25, and 20 nm thick regions across the thin film starting from the PMN-PT/BSRO bottom electrode interface show alternating out-of-plane polarity. While the out-of-plane component map shows domains with the alternate average polar directions along [001] (Figure 4-2b), the in-plane component map shows uniform distribution of opposite polarity domains across the film along [001] (Figure 4-2c).

The existence of larger polar domains with alternate polarity along [001] can be explained as a result of the combined effect of epitaxial strain and local chemistry. Polar domains are strongly affected by epitaxial strain; thus, compressive strain along the in-plane direction allows domains to grow unrestricted along [001], showing a larger size than in the in-plane component map. Polar displacement vectors also show directional dependence based on the local chemistry at the unit cell level. For example,

with compositions with less than 32% PT (morphotropic phase boundary), PMN-xPT shows rhombohedral symmetry with a polar vector along <111>. In contrast, with higher PT content, the unit cell shows a transformation to a tetragonal unit cell with a polar vector along <001> [96]. Thus, variation in polar vectors indicates the varying distribution of Ti content along [001].

The polar structure across the film thickness shows distinct regions with varying polar or net displacement vectors magnitude and angle. This is also visualized using polar plots for every 5 nm of the film starting from the BSRO interface (Figure 4-3). The mean displacement vectors show an increase in angle from 137° to 216° in the first 25 nm of the film thickness and then decrease to 107° towards the film surface. While displacement vector direction changes mean magnitude of the displacement vector remains constant from the PMN-PT/BSRO interface until 30 nm and then shows an increase towards the film surface from 15.4 to 20.6 pm. Such variation in polar structure along the growth direction indicates changes in local structure arising from local chemical variation, as in the case of bulk relaxors (as discussed in chapter 3) or strain relaxation effects. The in-plane lattice parameter was measured across the thin film with B sublattice distances, and their standard error indicates no major strain relaxation, as shown in Figure 4-4. This suggests local chemical variation leads to variation in polarization across the thickness.

4.2 Composition analysis

STEM- energy-dispersive X-ray spectroscopy (EDS) mapping was performed on PMN-PT thin films to obtain the chemical distribution across the thin film structures, as shown in Figure 4-5. The line profile from the elemental map of Ti indicates a titanium enriched region of about 5 nm from the PMN-PT/BSRO interface. Ti enrichment has been found to be at the expense of Mg. While Ti and Mg show spatial variation, Nb elemental maps reveal a uniform distribution across the thin film. No evidence of any metal oxide precipitates is found, as shown in Figure 4-5.

A Pb-deficient region is also identified near the film surface, indicating that such

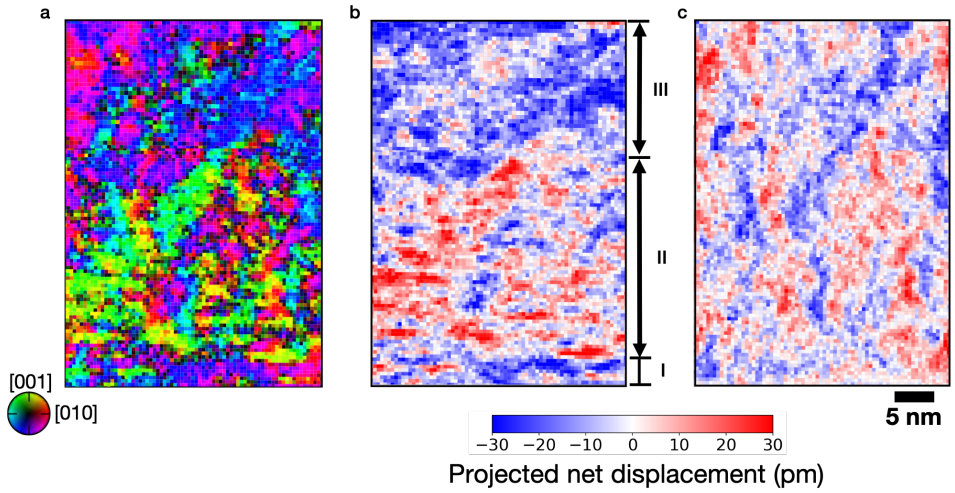

Figure 4-2: (a) Projected net displacement (polarization) map calculated across the PMN-PT thin film and polar net displacement vector component map calculated along (b) out-of-plane and (c) in-plane direction

PMN-PT thin films have Pb vacancies which could form due to Pb volatility during the film growth at elevated temperatures in pulsed laser deposition. An enhancement of net displacement/polarization magnitude is found near the surface, shown in Figure 4-6. The region with polarization enhancement is about 6-8 nm wide, which correlates with the Pb-deficient region (about 8 nm) as revealed from the EDS elemental profile. The presence of only Pb vacancies in PMN-PT had been found to suppress the polarization based on density functional theory calculations in literature [14]. Thus, higher polar displacements measured from STEM across Pb deficient region indicate that Pb vacancies near the surface of the film would lead to the variation in local chemistry at the B-sublattice, leading to the increase in polarization. This is evident in the Ti concentration profile, which shows an increase at the top of the film in a similar region of Pb-deficiency. Thus, increased Ti concentration could lead to an increase in polarization consistent with the observation in bulk PMN-PT samples where the addition of $PbTiO_3$ in PMN lead to an increase in polarization [1].

STEM electron energy-loss spectroscopy (EELS) was also performed to obtain Ti and O element distributions across the film with higher collection efficiency as compared to STEM-EDS. Figure 4-7 shows the EELS signal map, calculated after

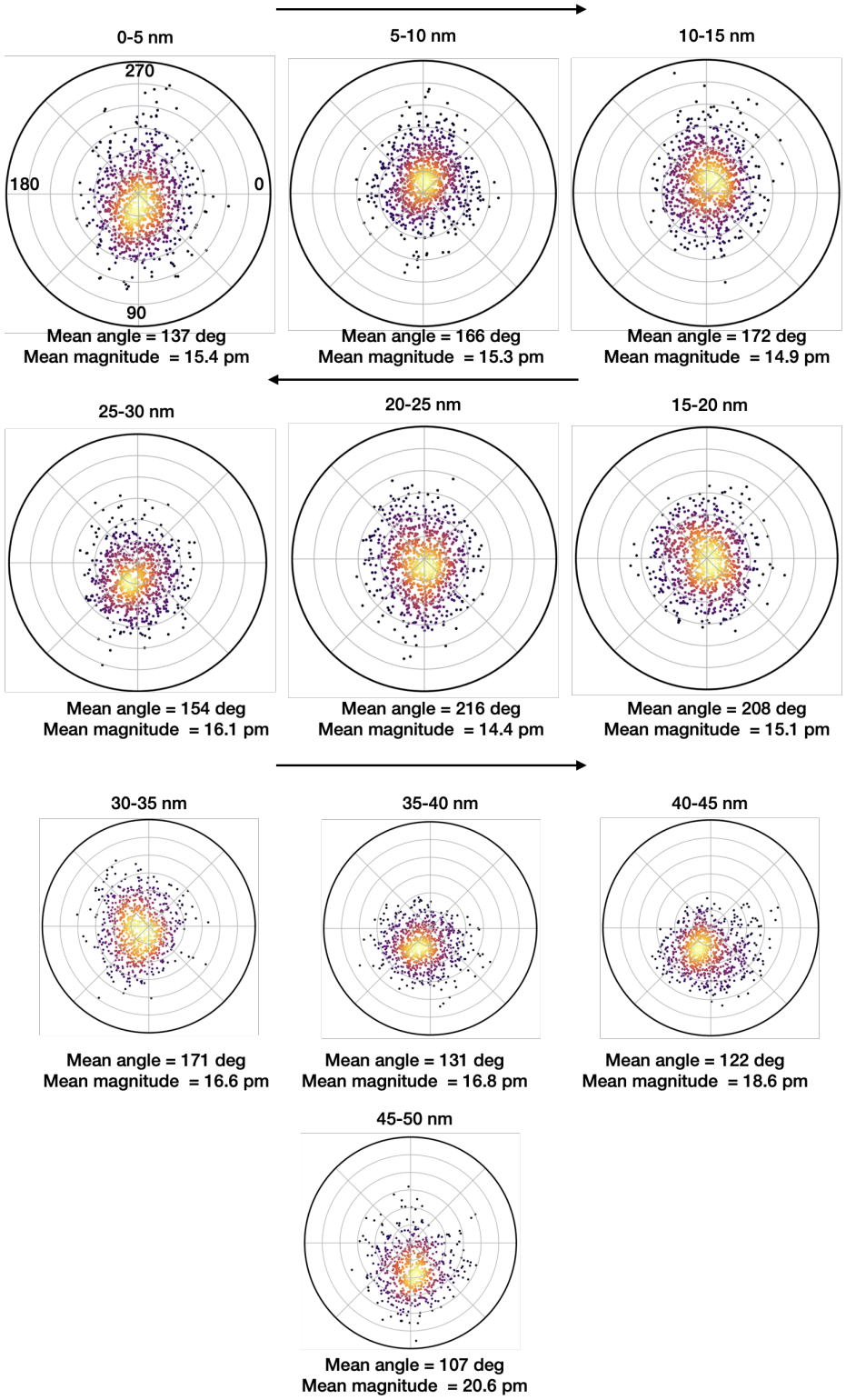

Figure 4-3: Polar plot of projected net displacement (polarization) from every 5 nm of the region starting from PMN-PT/BSRO bottom electrode

.

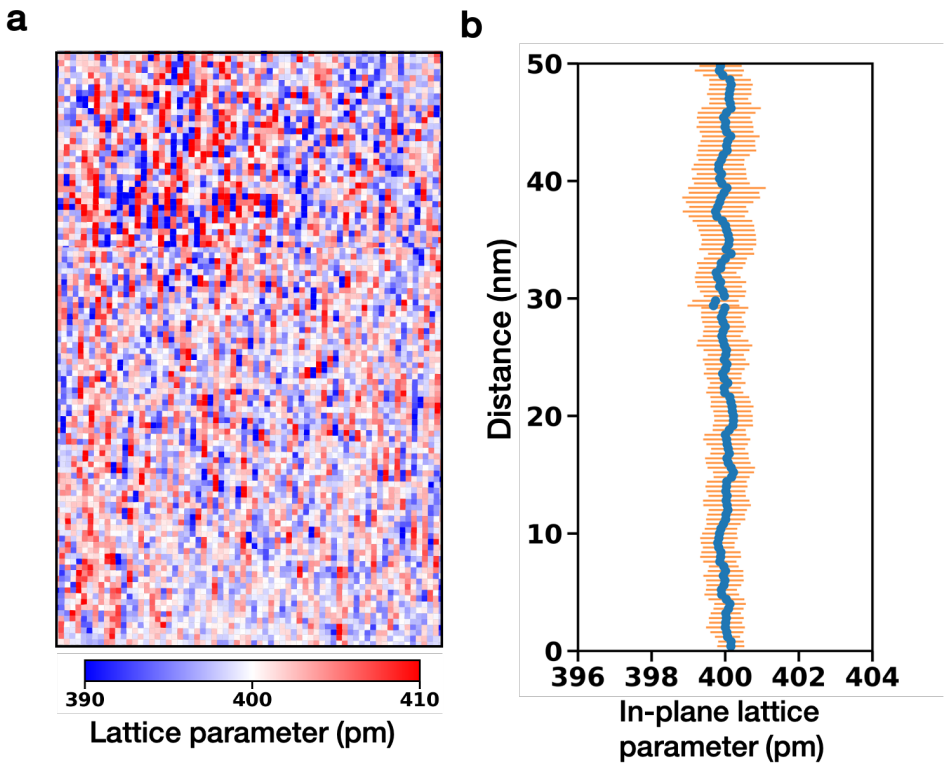

Figure 4-4: (a) In-plane lattice parameter map across PMN-PT thin film and (b) mean in-plane lattice parameter profile across the film thickness

.

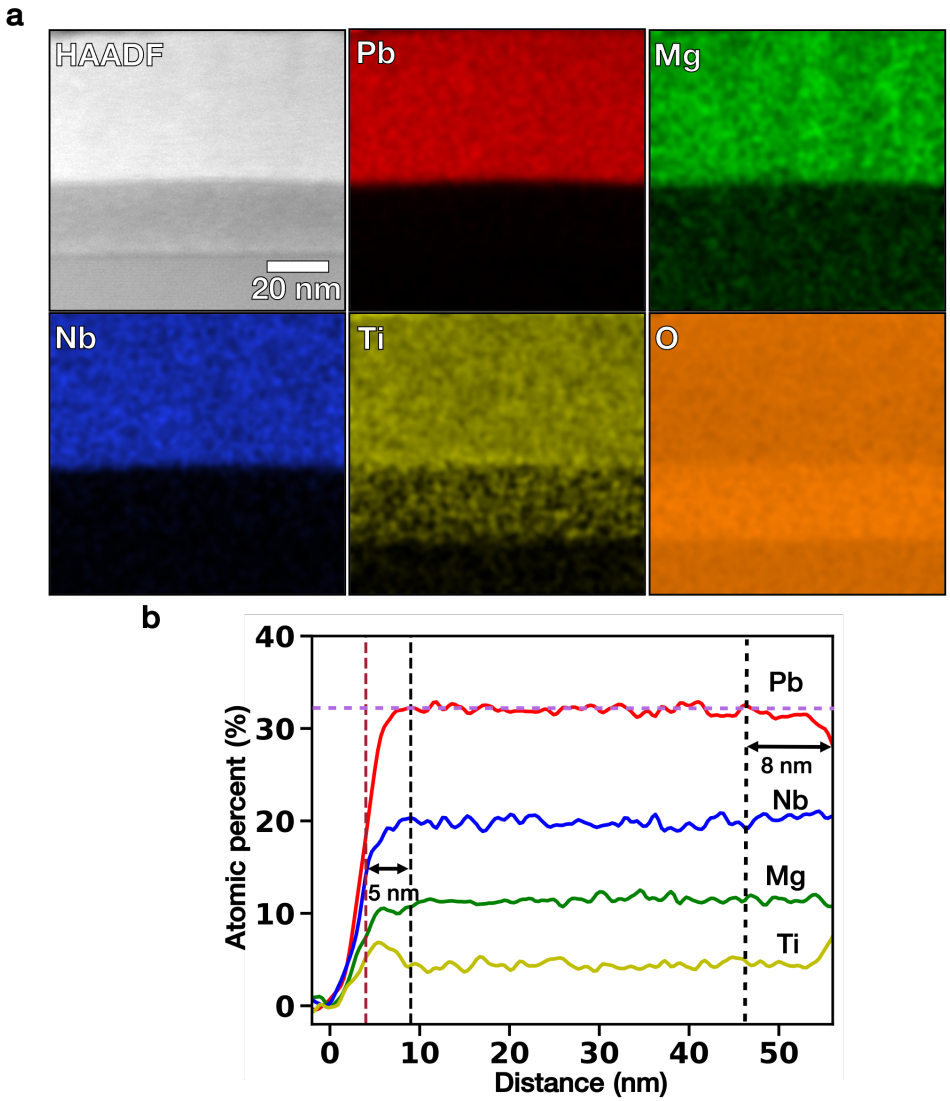

Figure 4-5: (a) STEM-EDS elemental maps of PMN-PT heterostructure in atomic percent and (b) line profile across EDS elemental map calculated with integrating map signal across the width

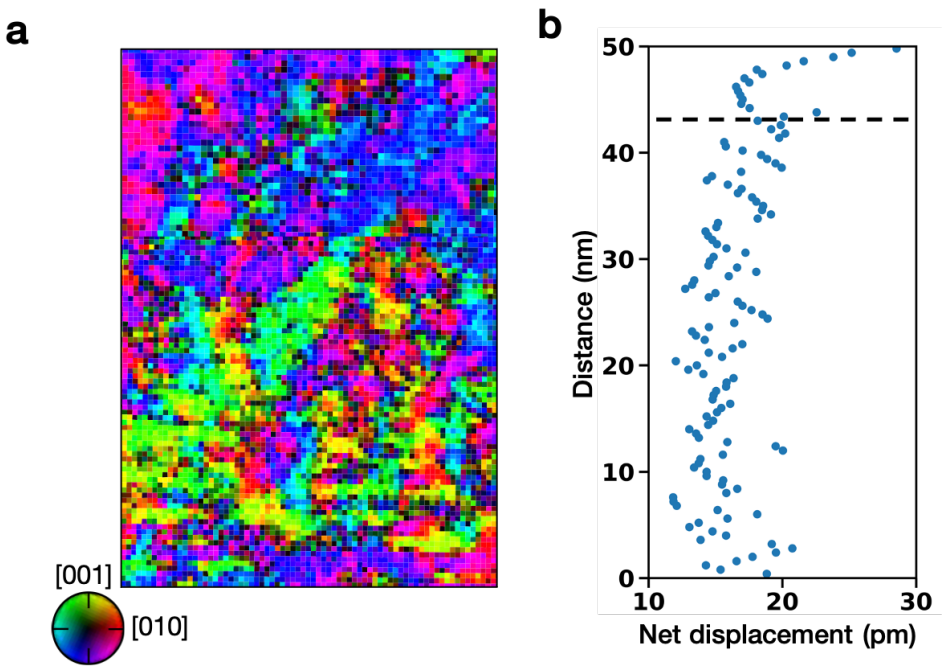

Figure 4-6: (a) Projected net displacement (polarization) map calculated across the PMN-PT thin film and (b) the average magnitude of net displacement (polarization) across the thin film

integrating the titanium L and oxygen k edges. The line profile across the integrated Ti signal map reveals an increase in Ti intensity for about 5 nm of the PMN-PT film starting from the PMN-PT/BSRO interface. The Ti L-edge intensity normalized with respect to the O K-edge intensity profile shows an increase in the same region, revealing the change in the local chemical environment in terms of Ti amount rather than thickness variation. This chemical variation is consistent with the EDS signal profile (Figure 4-5), indicating Ti-rich regions near the PMN-PT/BSRO interface.

Further, the spatially-varying polar structure is compared with the EELS intensity ratio of Ti and O along the growth direction of the thin film. The film region of about 7 nm from the PMN-PT/BSRO interface shows a higher ratio of Ti and O EELS intensity ratio > 1, where polarization mostly aligns down towards the bottom BSRO electrode (Figure 4-7), as evident in the polar plot from the 0-5 nm region shown in Figure 4-3. This indicates that increasing Ti content leads to larger polar order in the relaxor film. This is consistent with Ti content dependant polar structure behavior in bulk PMN-PT, where short polar order relaxor transforms to a normal ferroelectric

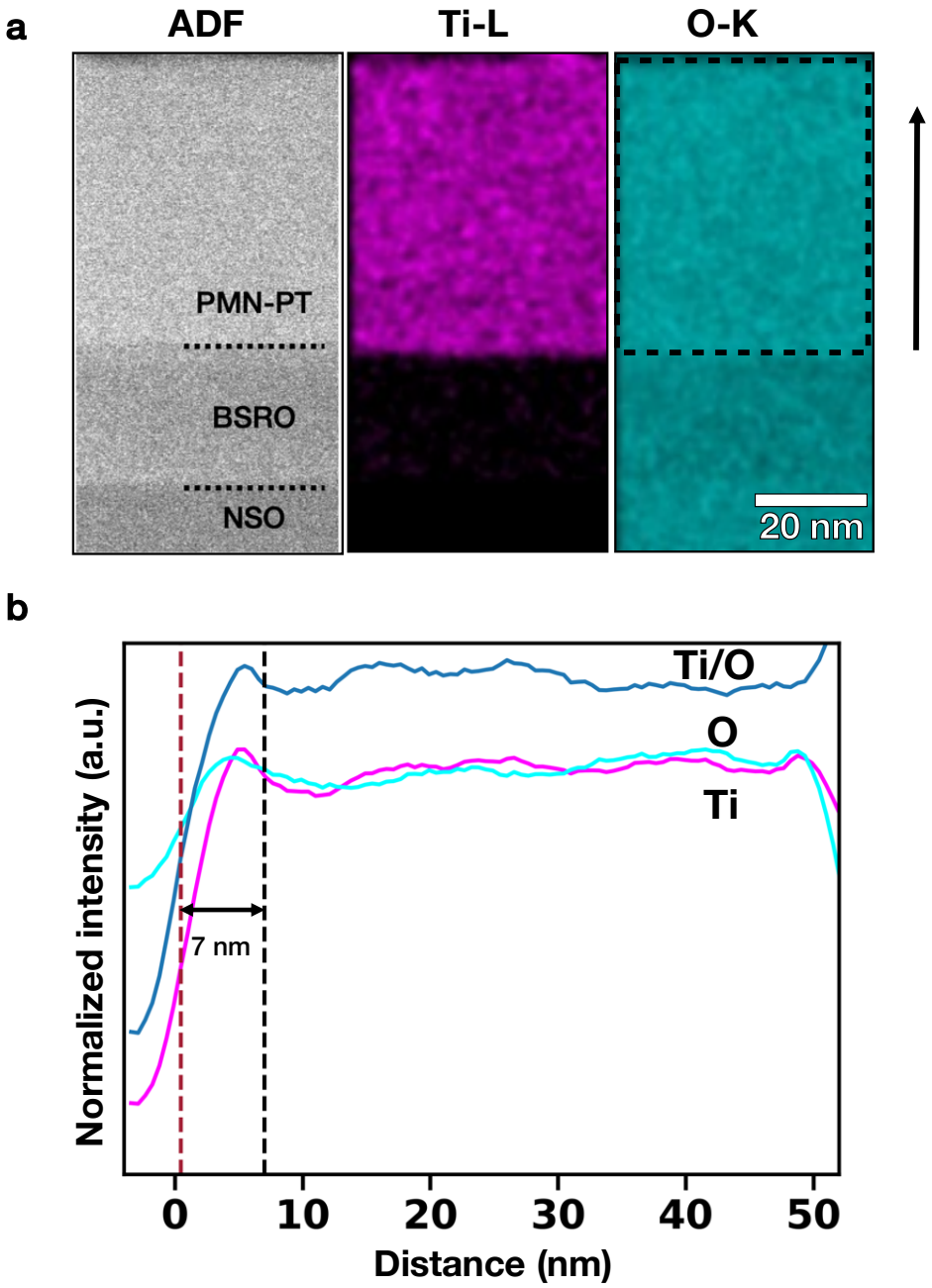

Figure 4-7: (a) STEM-EELS elemental maps of PMN-PT heterostructure obtained by integrating signal across Ti-L and O-K edge and (b) line profile of EELS integrated signal of Ti and O and their ratio

with large polar order with increasing Ti amount above 32 atomic % [16]. Short-range polar ordering is found in between 5-30 nm thick region, which can be attributed to the increase in local chemical randomness as indicated by fluctuations in Ti/O ratio. Above 30 nm, as the Ti and O EELS intensity ratio becomes more uniform, the polar structure also shows a larger domain structure with less polarization spread, as evident in the corresponding polar plots.

ADF intensities have shown sensitivity with the change in the type of elements occupied across the atomic columns and sample thickness [79]. ADF intensities are normalized to their first nearest neighbor, minimizing the effects of sample thickness variation [26]. Thus, normalized ADF intensity of Mg/Nb/Ti/O atomic columns on the [100] projected image is utilized to quantify the chemical disorder in B-sublattice occupancy across the film (Figure 4-8). The mean and standard deviation of these normalized atomic column intensities is calculated from unit cells along the in-plane direction [010]. The mean intensities fluctuate with different layers along the growth direction [001]. An average intensity greater than 1 indicates an Nb-rich layer, while one lower than 1 indicates an Nb-deficient layer. The standard deviation of normalized ADF intensities is obtained to reveal the disorder in chemical distribution, as shown in Figure 4-8. The standard deviation of ADF intensities shows a linear increase to 30 nm of thickness. This correlates with polar structure, as maximum polar variation is shown until 30 nm. Above 30 nm, a constant standard deviation in ADF intensities is found, indicating uniform composition in the B-sublattice's Mg, Nb, and Ti elemental distribution. This exhibits a direct correlation between local chemical and polar structure variation across the thickness for PMN-PT thin films.

The spatial variation of polar structure across the film can be explained based on the effect of chemical pressure during layer-by-layer growth [97]. As the BSRO bottom electrode is under in-plane compressive strain, thus ions that lead to local compressive strain will be favored. Ions with a smaller ionic radius will be preferred as they will allow local lattice to be compressively strained (decrease in lattice parameter) [98, 99]. B-sublattice cations (Mg/Nb/Ti) show ionic sizes of 72, 64, and 60 pm for Mg^{2+}, Nb^{5+} and Ti^{4+}, respectively [100]. Ti^{4+} shows the lowest ionic size, thus leading to

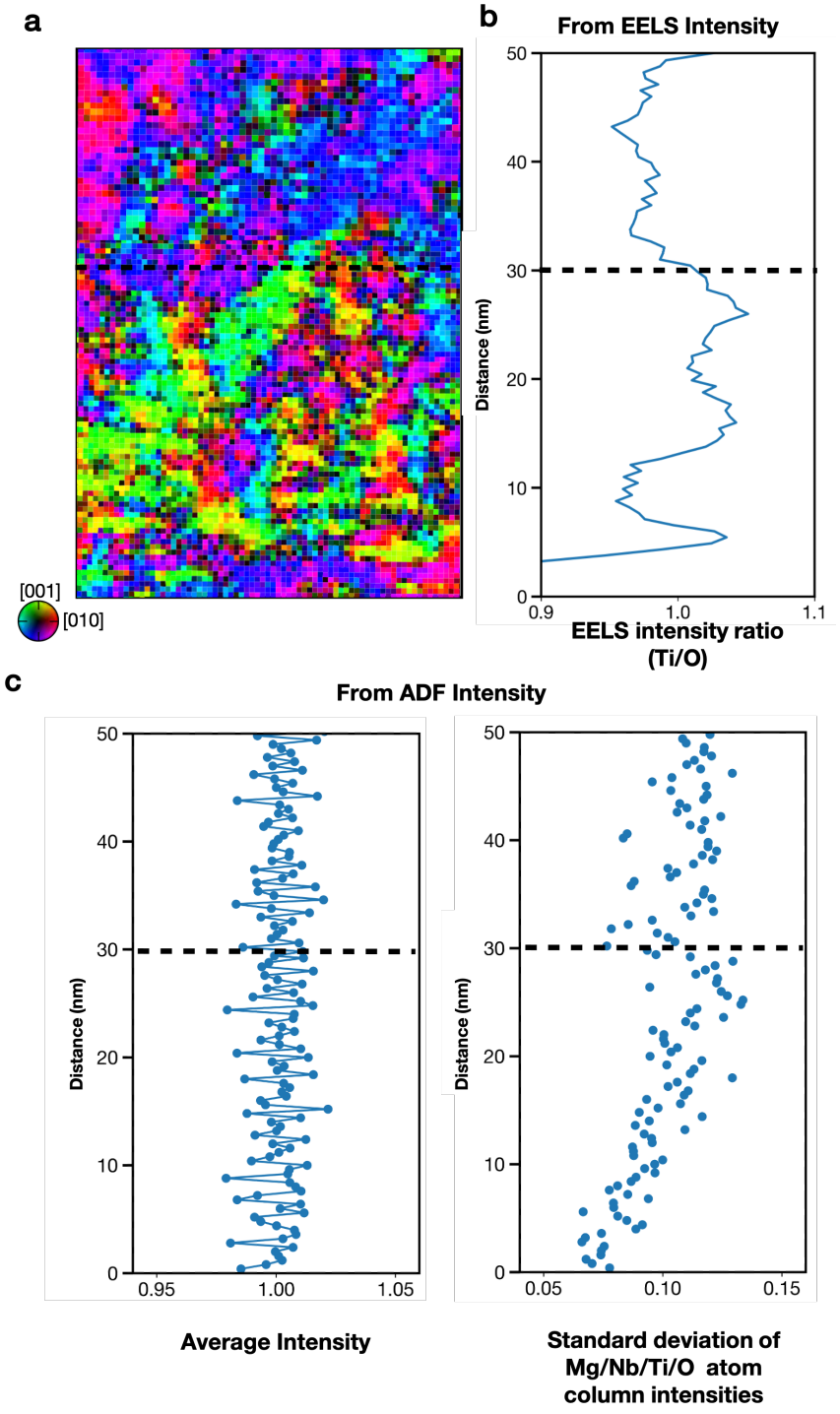

Figure 4-8: (a) Projected net displacement (projected polarization) map in PMN-PT thin film, (b) EELS integrated intensity ratio of Ti-L and O-K edge, (c) mean and standard deviation of ADF intensity of B sublattice, Mg/Nb/Ti/O atomic columns

the locally compressed lattice. Ti also shows a charge state of 4+ similar to Ru. The preferable ionic size and charge state of Ti, explain Ti enrichment near the PMN-PT/BSRO interface. As the thin film grows, random site occupancy prevails based on atomic diffusion.

4.3 Spatial distribution of inhomogeneities

As we observed in the bulk relaxors (discussed in chapter 3), inhomogeneities such as chemical order, octahedral tilt, and distortion-ordered regions act as polarization barriers leading to the formation of the nanoscale domain structure. Thus, spatial mapping of inhomogeneities across film thickness is required to fully understand polar domain structure evolution across the thin film. Chemical ordering of β_I (Mg-rich) and β_{II} (Nb-rich) atomic columns on {111} plane is not possible to visualize with [100] projected atomic column images due to projection effects [26]. Thus, samples along $\langle 1\bar{1}0 \rangle$ direction must be imaged to calculate the spatial distribution of inhomogeneities across the thickness.

Figure 4-9a shows normalized ADF intensities of Mg/Nb/Ti atomic columns, revealing variation across the thickness. Normalized ADF intensities from the B sublattice averaged along [110] (in-plane direction) in Figure 4-9b show fluctuations, indicating changes in local chemistry across the thin film. The thin-film region of about 8 nm thick from the PMN-PT/BSRO bottom electrode interface shows a lower variation in average intensity than the above. This is consistent with Ti enrichment in the region as found from STEM-EDS and EELS mapping, which leads to a decrease in chemical ordering along the {111} plane and thus less variation in ADF intensities. The standard deviation of the ADF intensity from the B-site atomic columns also shows thickness-dependent behavior (Figure 4-9c). A larger standard deviation in the ADF intensities is found above 30 nm of thin-film on $\langle 1\bar{1}0 \rangle$ projected images, thus indicating a larger local variation in chemistry. While in $\langle 100 \rangle$ projected images, the ADF intensity shows a constant standard deviation, in $\langle 1\bar{1}0 \rangle$ images, standard deviation increases, such disparity can be explained by increasing chemical ordering

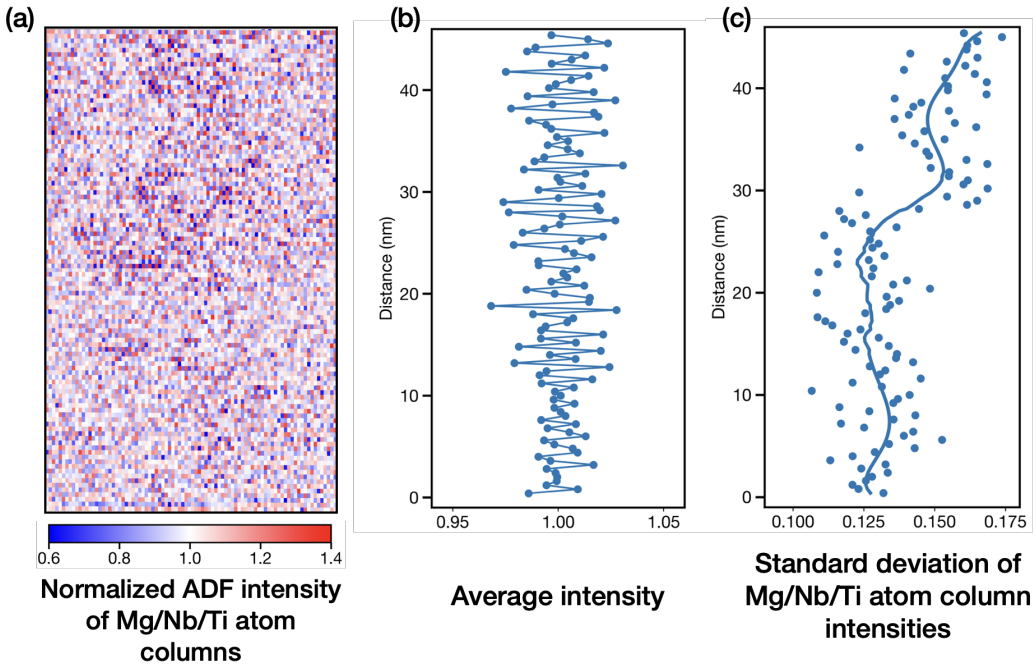

Figure 4-9: (a) Normalized intensity map of B sublattice, Mg/Nb/Ti atomic column (b) mean and (c) standard deviation of ADF intensity of B sublattice, Mg/Nb/Ti atomic columns from $\langle 1\bar{1}0 \rangle$ projection images

on {111} planes.

Further, to determine the chemically ordered regions across the thin film, a kernel correlation method is employed where a checkerboard pattern is used as a kernel on the normalized intensity map from B-sublattice atomic columns as described in chapter 3 for the case of bulk relaxor samples. Here, we define the chemical order metric based on the correlation coefficient (Figure 4-10 a). The average chemical order metric along [110] shows variation in ordering behavior across the film thickness. Higher chemical ordering is observed farther away from the PMN-PT/BSRO interface as indicated by a 5-10 % increment of unit cell within the chemical ordered region and mean of the order metric (figure 4-10 b & c). In the 10 nm region from the PMN-PT/BSRO interface, lower chemical ordering is found, consistent with the Ti-enriched region, leading to a similar decrease as in the bulk PMN-PT system [22]. An increase in chemical ordering is evident more towards the film surface. This is due to Pb vacancies, which promote chemical ordering, as shown in the literature in the case of the PST system [45].

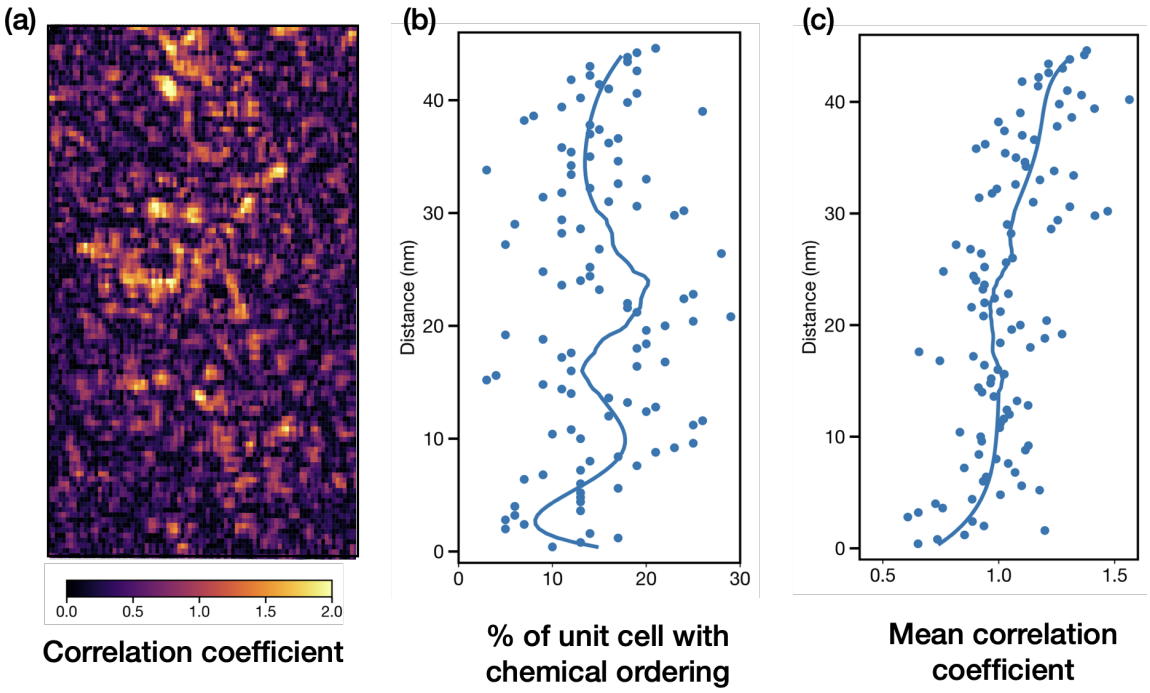

Figure 4-10: (a) Correlation coefficient map of chemical ordering calculated from normalized ADF intensity map (b) the percentage of the unit cell along [010], which favors chemical ordering, and (c) mean of chemical ordering correlation coefficients

To determine the octahedral distortion and tilt ordering, oxygen-oxygen distance and tilt are calculated across the thin film. The oxygen-Oxygen distance map reveals two distinct patterns similar to the bulk PMN-30PT sample: a checkerboard pattern with alternate higher and lower O-O distance with respect to the mean value along [111] planes, and a striped pattern that shows higher and lower O-O distance compared to the mean distance along [110] direction, as shown in Figure 4-11a. Such distinct O-O distance patterns are similar to those found in the bulk system as discussed in chapter 3, and correspond to the rhombohedral and monoclinic-like distortions. A larger variation in oxygen-oxygen distance is observed across the film, but the total deviation in O-O distance is almost constant along with the film thickness (Figure 4-11). A similar correlation method is used for chemical ordered regions to find the octahedral distortion ordering mainly with rhombohedral distortions. The map of the oxygen-oxygen distortion order metric reveals lower ordering in the first 10 nm of the thickness than above. As we found in the case of bulk relaxor system, O-O

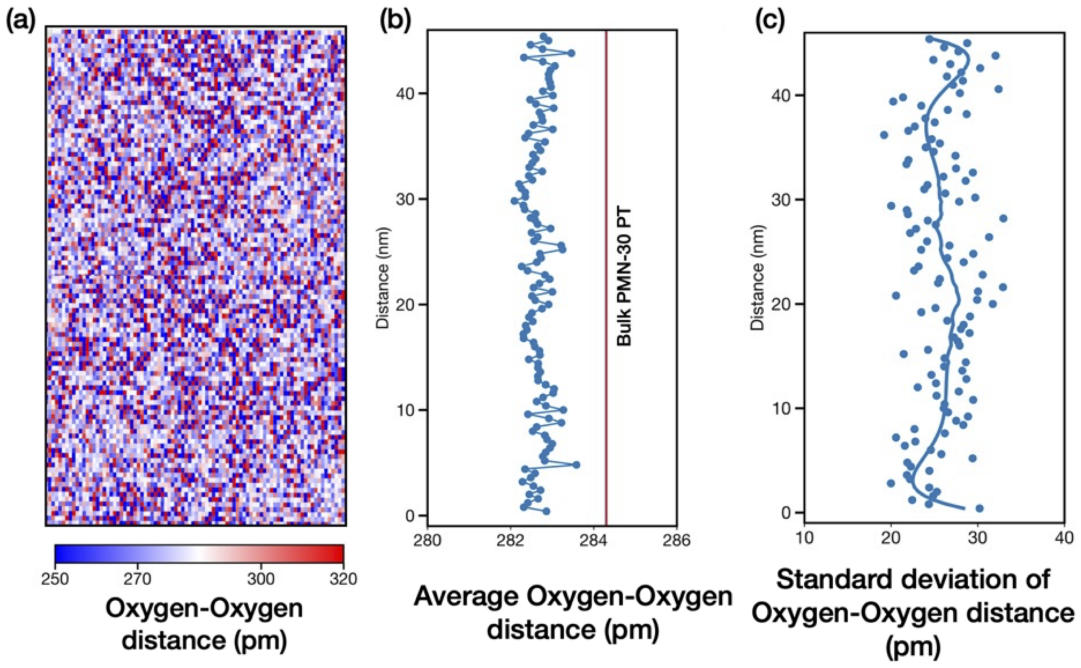

Figure 4-11: (a) Oxygen-Oxygen distortions along [110] (b) mean and (c) standard deviation of oxygen-oxygen distortions

distortion ordering is partially correlated with chemical ordering. Such behavior can be visualized in the thin film as well. Thus, Ti enrichment in the film region near the bottom BSRO electrode explains a lower oxygen distortion order metric, as an increase in Ti leads to a decrease in the chemical ordering.

Further, oxygen-oxygen (O-O) tilts along [110] are calculated across the film thickness. The O-O tilt shows a higher average value in the 2.5-3.5 deg range. across the film thickness as compared to the bulk PMN-PT, which has an average O-O tilt value of 1.7 deg. (Figure 4-13). An increase in O-O tilt value is either due to the effect of local chemical variation or the size confinement in the thin film form, as shown in the literature for other oxides under epitaxial strain [101, 102]. Plotting the O-O tilt average also reveals a higher value in the first 30 nm of the film region starting from the PMN-PT/BSRO interface than the film region towards the surface (Figure 4-13 b). Similar behavior is also found in the standard deviation of O-O tilt profile, indicating more chemical randomness between 5-30 nm of film, leading to an increase in the O-O tilt values in this region. The checkerboard pattern is also found in O-O

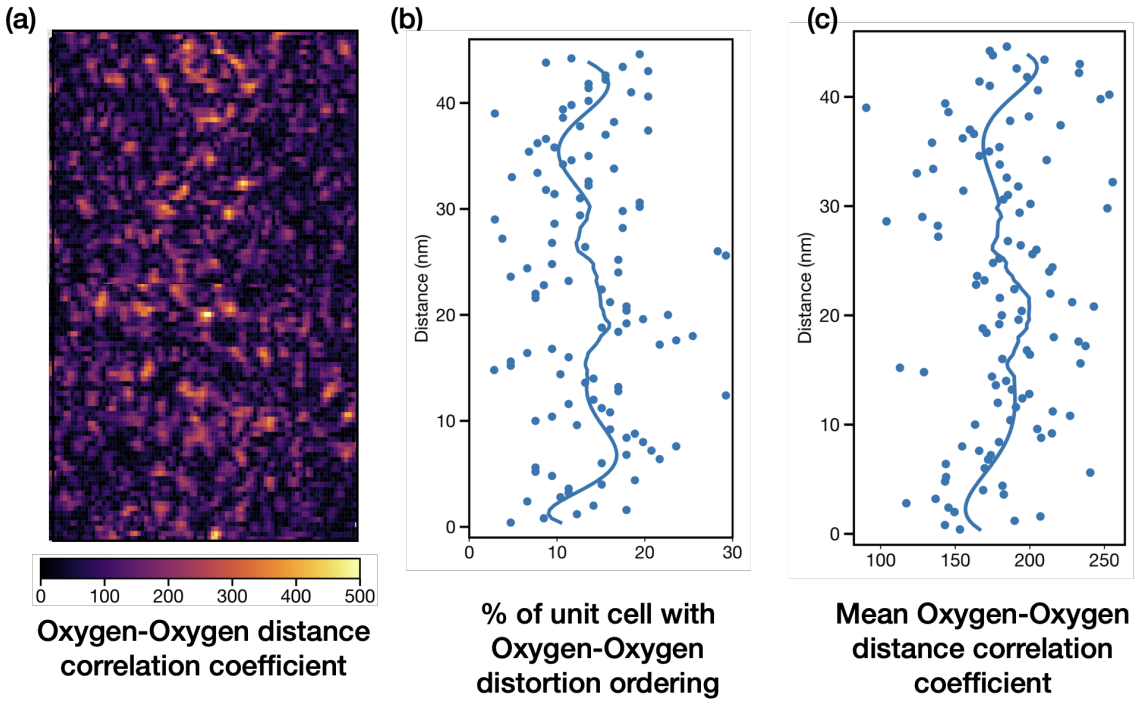

Figure 4-12: (a) Correlation coefficient map of oxygen octahedra distortion ordering (b) the percentage of the unit cell along [010], which favors oxygen-oxygen distortion ordering, and (c) mean of oxygen-oxygen distortion ordering correlation coefficients

tilt maps as previously seen in the bulk PMN-xPT system. Thus, O-O tilt ordered regions are determined using a similar correlation method with a checkerboard template highlighting areas of alternately positive and negative tilts (Figure 4-14 a). The percentage of unit cells with O-O tilt ordering along the in-plane direction is also calculated. This reveals that the amount of tilt ordering varies between 10-20 % of the unit cells along the film thickness. The amount of tilt-ordered regions is also found to decrease towards the film surface (Figure 4-14b). This is consistent with the result from the chemical order map, which shows an increase in chemical ordering towards the film surface, decreasing the probability of O-O tilt order as found in bulk PMN-PT. Figure 4-14c shows the extent of O-O tilt order, indicating an increase of order in the region above 30 nm of the film while the size of such ordered regions decreases.

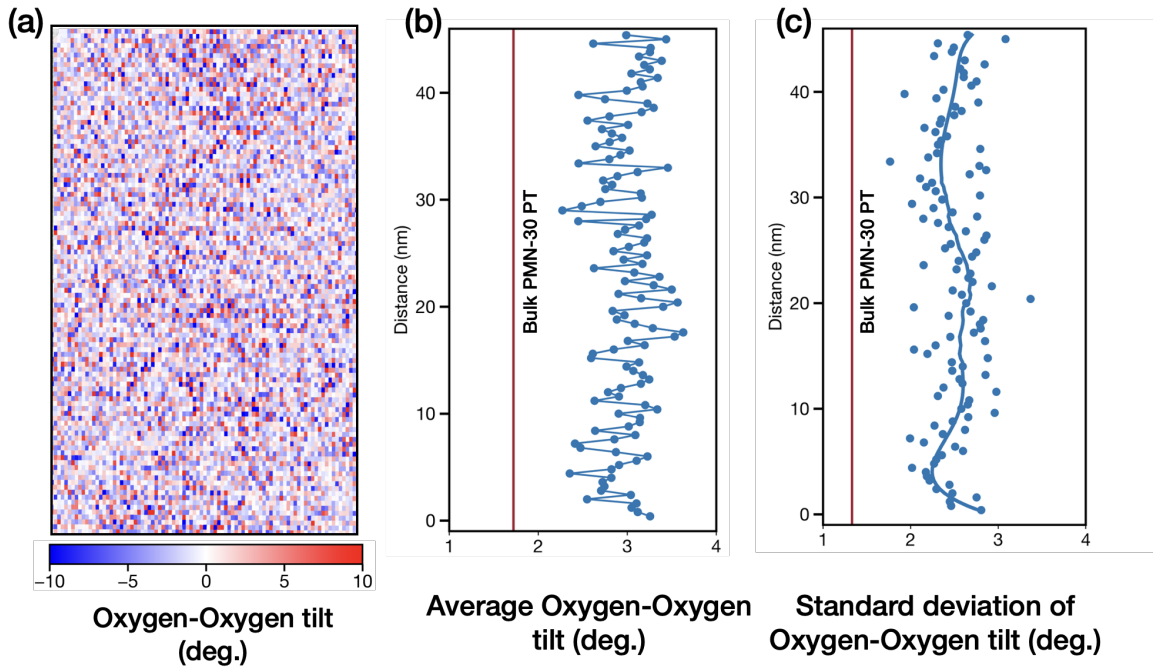

Figure 4-13: (a) Oxygen-Oxygen tilts along [110] (b) mean and (c) standard deviation of oxygen-Oxygen tilts

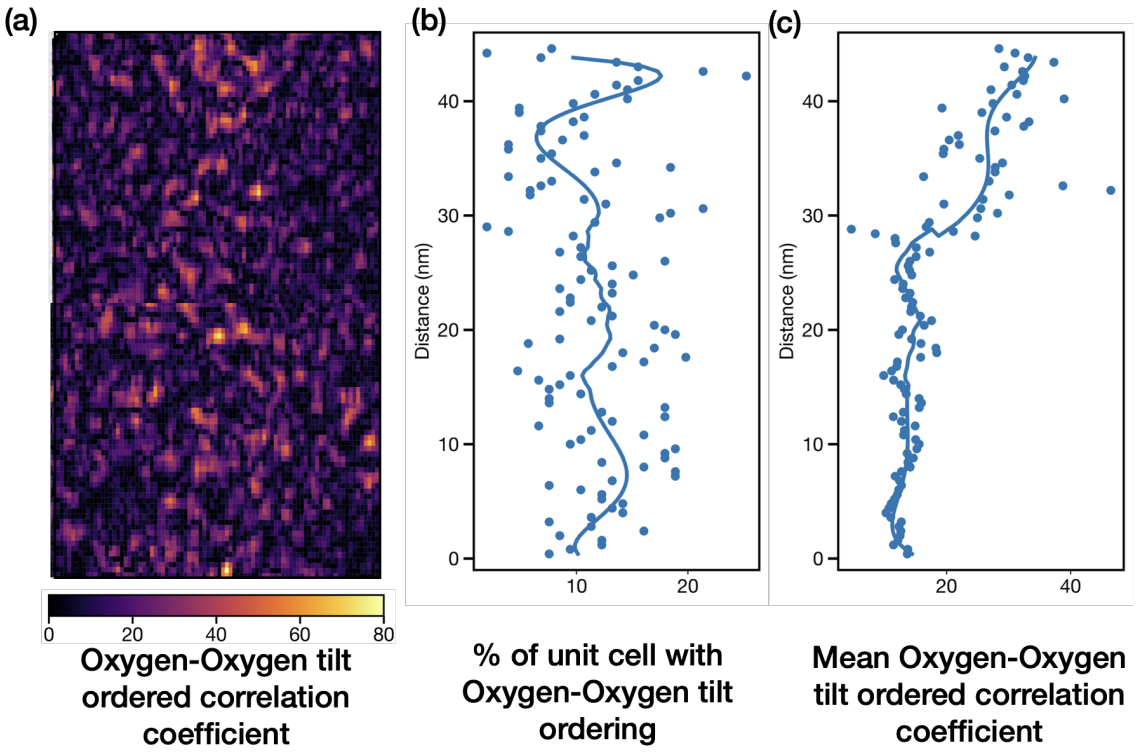

Figure 4-14: (a) Correlation coefficient map of oxygen-oxygen tilt ordering (b) the percentage of the unit cell along [010], which favors oxygen-oxygen tilt ordering, and (c) mean of oxygen-oxygen tilt ordering correlation coefficients

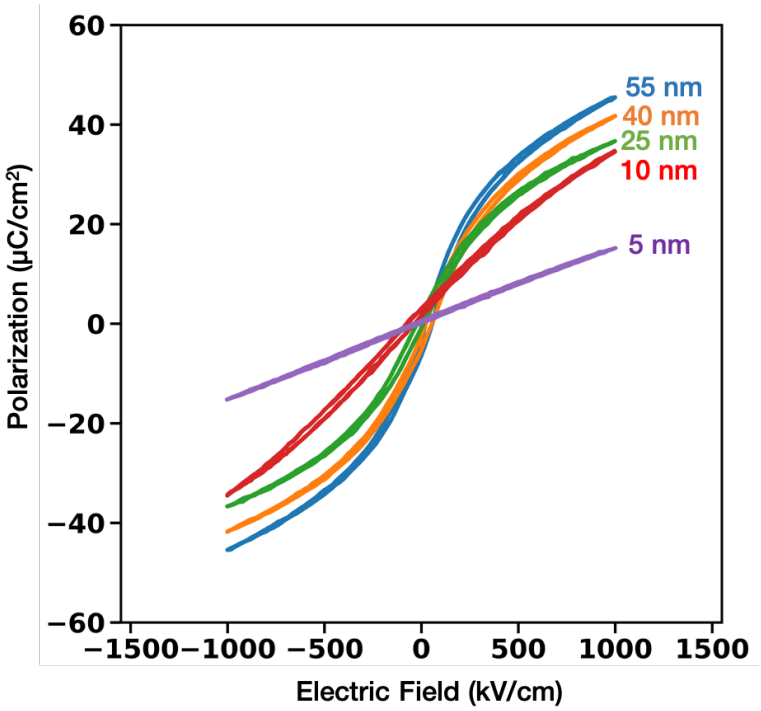

Figure 4-15: Measured polarization in PMN-PT thin films with thicknesses 5, 10, 25, 40, and 55 nm under an applied electric field at room temperature

4.4 Critical thickness in relaxor

Ferroelectricity in thin films diminishes due to the effects of the depolarization field at a critical thickness. This determines the minimum thickness for the ferroelectric film that can be used in devices. Thus, the critical thickness for compositionally heterogeneous relaxor films is necessary to determine before their applications. PMN-PT thin films were grown using pulsed laser deposition (PLD) with different thicknesses of about 5, 10, 25, 40, and 55 nm. All these thin films were grown on $NdScO_3$ substrate with a bottom $Ba_{0.5}Sr_{0.5}RuO_3$ electrode. Thus, all the films with varying thickness experience a similar -0.5%in-plane compressive epitaxial strain. The polarization measured from these films under an applied electric field show relaxor ferroelectric behavior vanishes below 10 nm, as shown in Figure 4-15. The saturation polarization also decreases with film thickness, similar to the behavior of normal ferroelectric thin films[103]. Diffuse scattering features in X-ray diffraction studies are also absent in films below 10 nm [104]. While in comparison to normal ferroelectric, the critical

thickness for relaxors is 8-10 times larger. In $BaTiO_3$ or $PbTiO_3$ thin films, the critical thickness is usually between 1-2 nm [103, 105]. The structural origin of larger critical thickness for relaxors needs to be determined.

Polar structure mapped across thin films with varying thickness reveals significant changes. To determine the effects of thickness variation in PMN-PT relaxors films, polar maps of thin films of the lower thickness of 5 and 25 nm are compared with similar thickness regions from 55 nm thick PMN-PT film as shown in Figure 4-16 & 4-17. Significant differences in polar structure have been revealed, shown in Figure 4-16 b & c. Such differences are found for both 5 and 25 nm films. Polar vector components along out-of-plane and in-plane directions also show variation in 25 and 5 nm film as compared to 55 nm (Figure 4-16 and 4-17 d & e). Figure 4-18 show the polar plot of net projected displacement vectors from multiple regions of 5 and 25 nm films. This reveals that overall the polar vector's in-plane contribution increases with decreasing the thickness. In the case of 5 nm film, the polar correlation increases along the in-plane direction in comparison to the similar region in thicker film, shown in Figure 4-17e. This is consistent with the molecular dynamics simulation results, which indicate that in-plane polar correlations increases at lower thicknesses [104]. This increase in in-plane or decrease in out-of-plane polar correlations relates to the diminishing relaxor behavior in these films.

Polar structure evolution and decreasing relaxor behavior with varying film thickness can be explained based on the depolarization field along out-of-plane direction [001]. The depolarization field can arise in relaxors due to incomplete charge balance due to heterogeneous chemical distribution along the growth direction. Mg, Nb and Ti are usually in +2, +5, and +4 charge states. In bulk or thicker thin, PMN-PT stays overall charge balance even with local charge imbalance. With varying thickness, the films with different net charges along growth direction [001] can be obtained. This could be the possible reason for decreasing polar correlation along the out-of-plane direction and increasing along the in-plane direction. This charge imbalance can arise due to the growth mechanism of these films, which influences due to chemical pressure, as discussed above. The effect of different compositions in

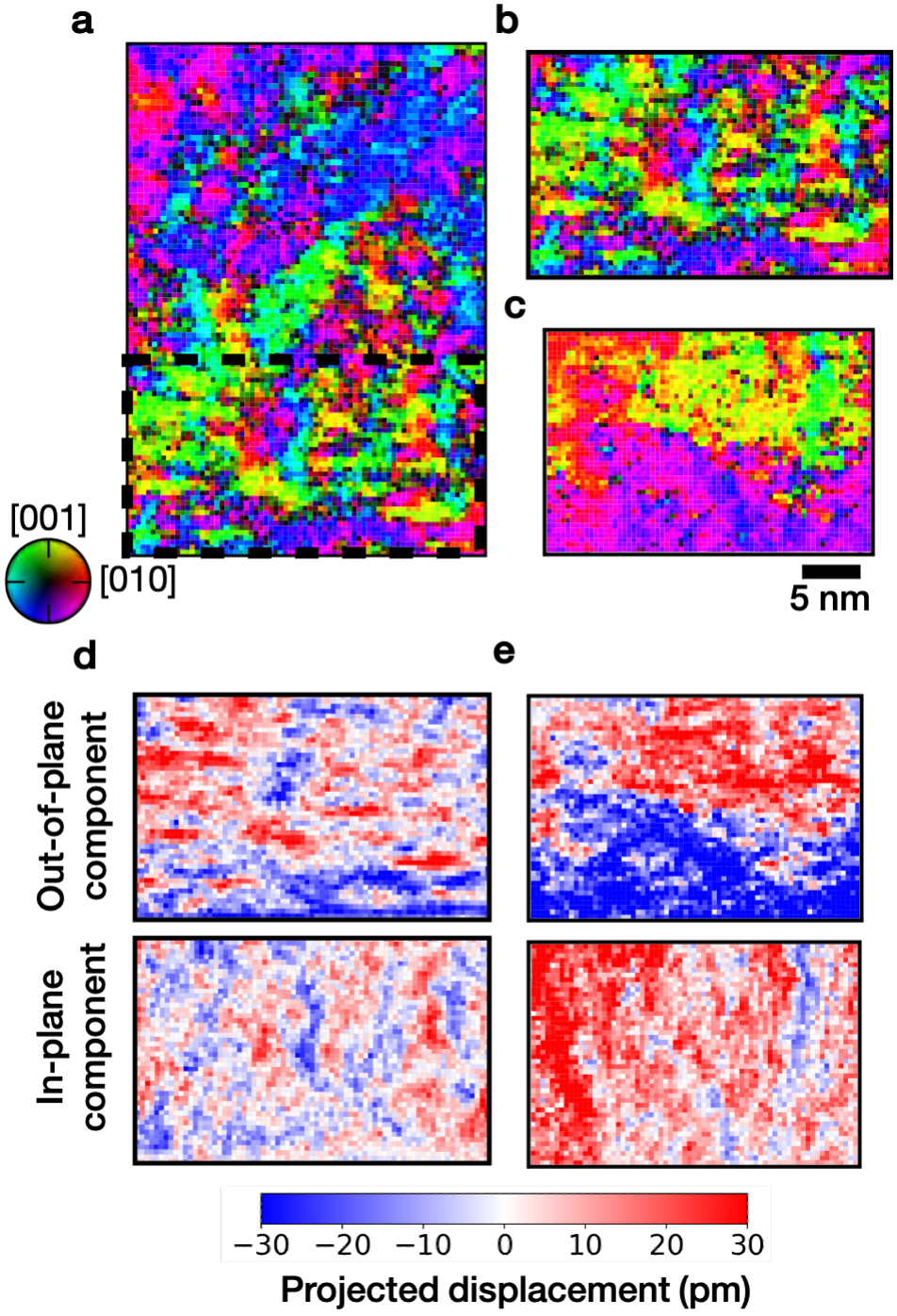

Figure 4-16: Polarization map of (a) as grown 55 nm film, (b) 25 nm sub-region of 55 nm film, and (c) as grown 25 nm film. (d) & (e) out-of-plane and in-plane component maps of polar vectors in 25 nm sub-region of 55 nm film and as grown 25 nm film, respectively.

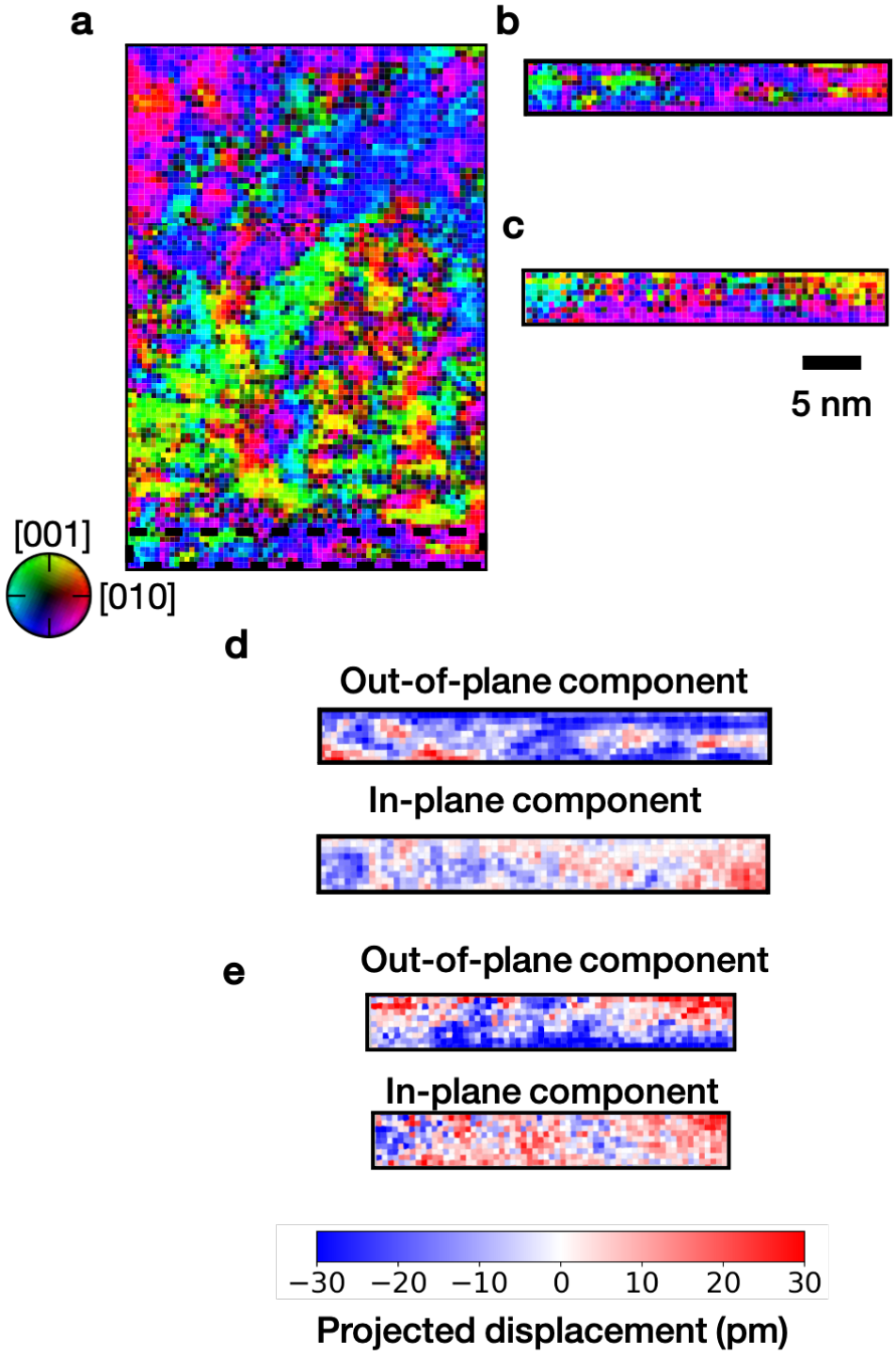

Figure 4-17: Polarization map of (a) as grown 55 nm film, (b) 5 nm sub-region of 55 nm film and (c) as grown 5 nm film. (d) & (e) out-of-plane and in-plane component maps of polar vectors in 5 nm sub-region of 55 nm film and as grown 5 nm film, respectively.

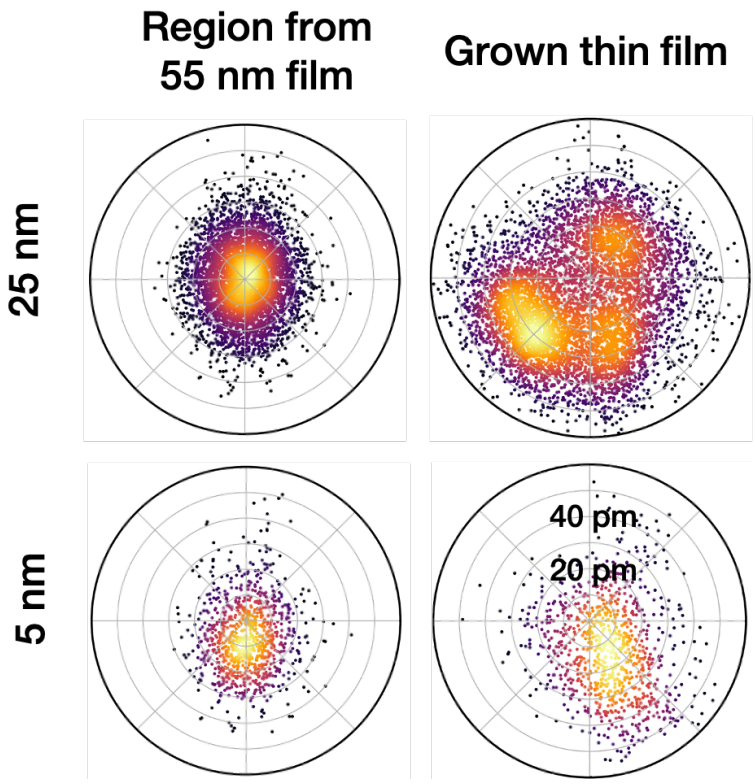

Figure 4-18: Polar plot of projected net displacement (polarization) for 25 and 5 nm as grown thin film and sub-region from 55 nm film

creating depolarization can be explored in the future to determine the atomic scale mechanism of this phenomenon.

4.5 Conclusions

The polar domain structure shows three distinct regions in terms of polar order change across the PMN-PT thin films. The bottom 5 nm region shows Ti enrichment, leading to an increase in polar order. A lower chemical order metric is consistent with a higher amount of Ti in the same region. An increasing chemical disorder found in the 25 nm region directly correlates with the maximum polar variation or smaller polar ordering. The chemical order metric map also shows maximum variations in this region, revealing more local chemistry disorders. Above 30 nm, this region shows an increase in the amount and extent of inhomogeneities which is attributed to the presence of Pb vacancies. This also leads to an increase in polar ordering. These thin films show no strain relaxation across the thickness. The variations in chemical and structural heterogeneities across the film thickness can be explained in terms of the surface chemistry of the BSRO bottom electrode, epitaxial strain from the substrate, and structural changes due to the local chemical environment. Finally, relaxor behavior vanishes for PMN-PT relaxor films below 10 nm. An increase in polar correlations along in-plane direction relates to diminishing relaxor behavior consistent with molecular dynamic simulations. A mechanism based on the depolarization field due to charge imbalance is proposed to explain the polar structure in PMN-PT thin films.

Chapter 5

Effect of epitaxial strain on relaxor behavior in PMN-PT thin films

in addition to the use fee itself and any other fees and charges specified."

This chapter aims to quantify the effects of epitaxial strain on the local chemistry and structure in PMN-PT relaxor thin films. PMN-PT thin films were grown on substrates with varying lattice parameters, enabling to apply in-plane biaxial compressive strain from -0.5 to -1 %. The polar structure across strained thin films shows significant variation with epitaxial strain. The polar domain size along the out-of-plane direction increases with strain. High-angle domain walls and an increased mean polar displacement magnitude at highly strained films indicate an increase in polar ordering with epitaxial strain. Further, the correlation between local lattice parameters and chemistry on a unit cell basis becomes weaker with increased strain. This decrease in local structure and chemistry coupling directly correlates with decreased relaxor strength with strain. Epitaxial strain also shows a prominent effect on the spatial distribution of chemical ordering across thin films. The size of chemical ordered regions increases with strain while the total amount of CORs remains constant. This indicates that increase in polar and chemical ordering are correlated consistently with the results from bulk relaxor samples, as discussed in chapter 3.

In this study, the PMN-PT thin films with -0.5, -0.75 & -1% epitaxial strain were provided by Dr. Jieun Kim and Prof. Lane Martin at University of California, Berkeley. The dielectric permittivity measurement as a function of temperature, Rutherford backscattering spectrometry and X-ray measurements were performed by Dr. Jieun Kim under the guidance of Prof. Lane Martin.

5.1 Polar domain structure

PMN-PT thin films were grown using pulsed laser deposition (PLD) on substrates with varying lattice parameters to determine the strain effects on relaxors. Substrates such as $NdScO_3$ (NSO), $Nd_0.5Sm_0.5ScO_3$ (NSSO), and $SmScO_3$ (SSO) (110) are used to obtain biaxial in-plane compressive strain of -0.5 %, -0.75% and -1% respectively. Annular dark-field (ADF) and integrated differential phase contrast (iDPC) STEM images are acquired simultaneously from the cross-section of the strained thin films

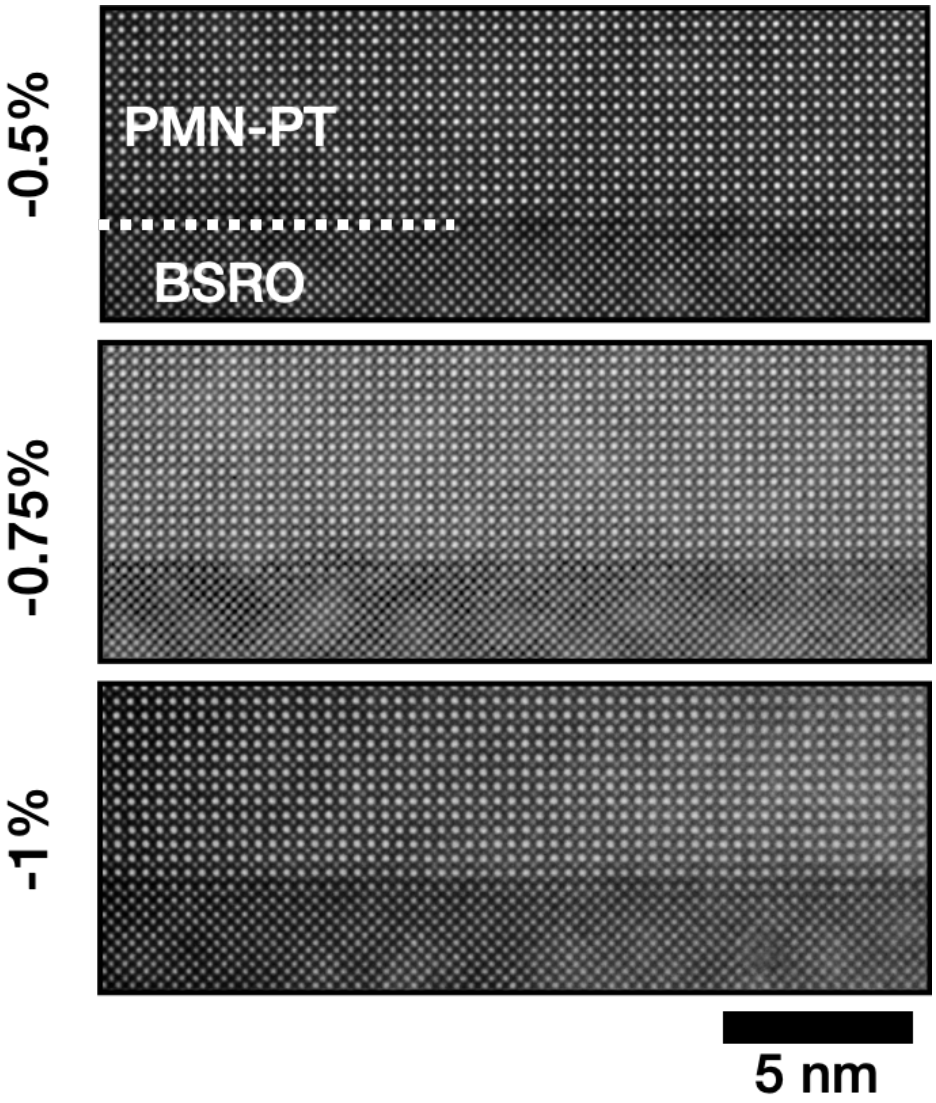

Figure 5-1: ADF-STEM images of PMN-PT/BSRO interfaces for -0.5%, -0.75% and -1% strained thin films

to reveal local chemical and structural variations. ADF-STEM images reveal PMN-PT thin films to be epitaxial with BSRO bottom electrode and the substrate in all strained films (Figure 5-1). No misfit dislocations are found across the strained films indicating these to be coherently strained. This is consistent with X-ray diffraction studies which revealed coherently strained PMN-PT thin films [55]. Rutherford backscattering spectrometry (RBS) measurements on these strained films reveal the overall composition remains the same across the strained thin film sample.

Further, iDPC-STEM images from these strained films are used to determine

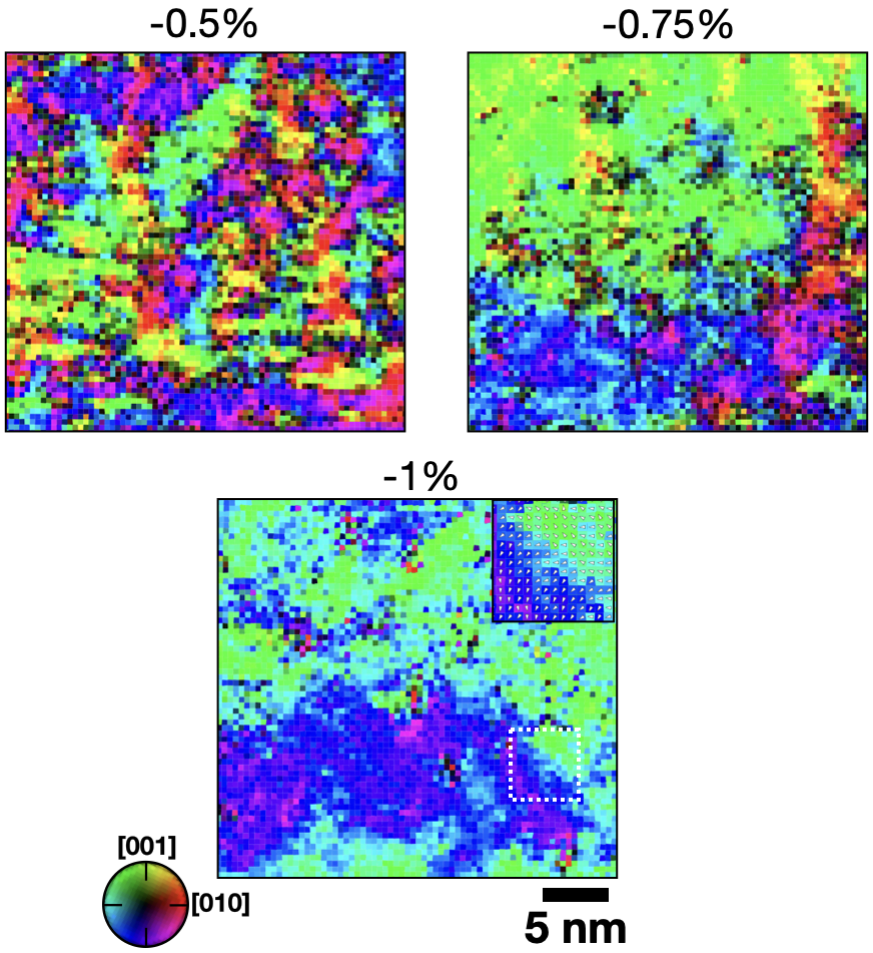

Figure 5-2: Projected net displacement(polarization) map determined using iDPC-STEM images for -0.5%, -0.75% and -1% strained thin films. The luminosity indicates the variation in projected net displacement magnitude from 1 to 15 pm

the projected polarization, i.e., the net displacement between the cation and anion atom columns on a unit cell basis (Figure 5-2). The film with -0.5% strain reveals asymmetric domains with elongated shapes along either [001] or [010] direction, as shown in Figure 5-2. Some of the elongated domains are also found to be inclined at $\sim 45°$. This indicates the formation of short-range nanoscale domains at lower strain, characteristics of a typical relaxor system. With an increase in strain to -1%, long-range polar order is found instead of elongated short-range polar ordered domains. The formation of high-angle ($\sim$135°) domain walls is also observed, similar to the polar structure in normal ferroelectrics. In the case of -0.75% coherently strained

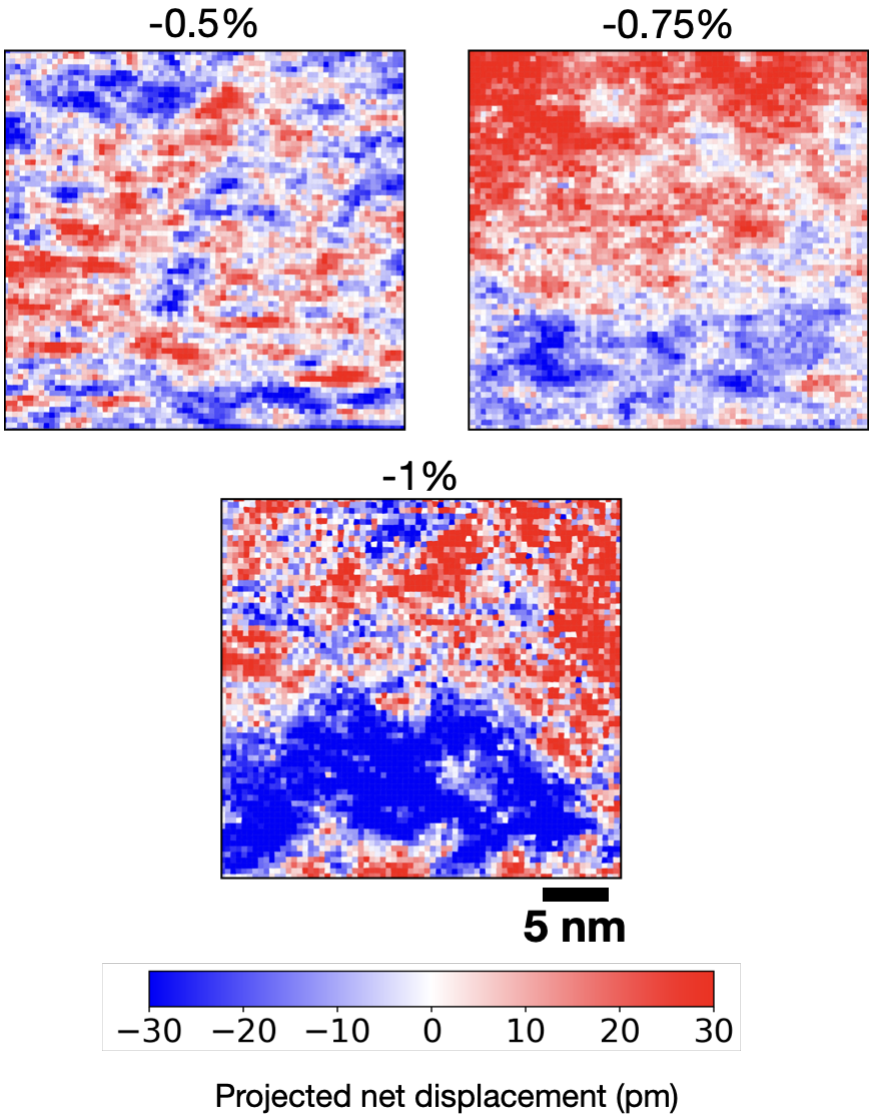

Figure 5-3: Polar net displacement vector component map calculated along out-of-plane [001] direction for -0.5%, -0.75% and -1% strained thin films

film, a mixture of inclined domains and long-range polar order is revealed, indicating the intermediate strained film attains a mixture of the polar domain structure of -0.5% and -1% strained film. These polar structure variations across strained films can be correlated with diffuse scattering features in the X-ray diffraction pattern (Figure 5-6) [55]. The -0.5% strained film reveals butterfly-shaped diffuse scattering features, while films with -1% strain show disc-shaped features. This allows associating the butterfly-shaped features to the short-range polar domains while increased ordering

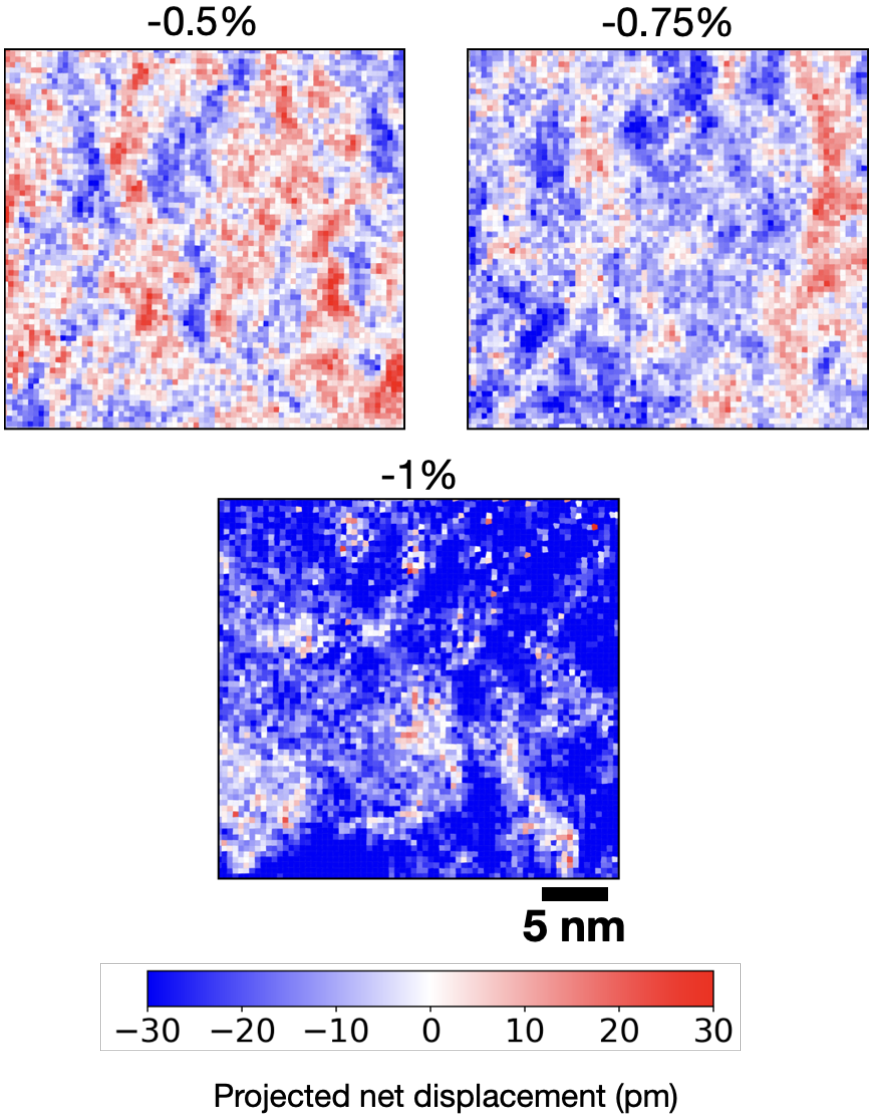

Figure 5-4: Polar net displacement vector component map calculated along in-plane [010] direction for -0.5%, -0.75% and -1% strained thin films

leads to disc-shaped diffuse scattering in diffraction patterns. Films with a -0.75% strain reveal a combination of butterfly and disc-shaped diffuse features consistent with real space polar domain structure, which show a mixture of structures of -0.5% and -1% strained thin films.

The polar structures across strained films show relation to their electromechanical response. Intermediate strained film (-0.75%) outperforms others by a factor of 1.5-2 times higher output strain with an applied electric field greater than 400 kV/cm. The

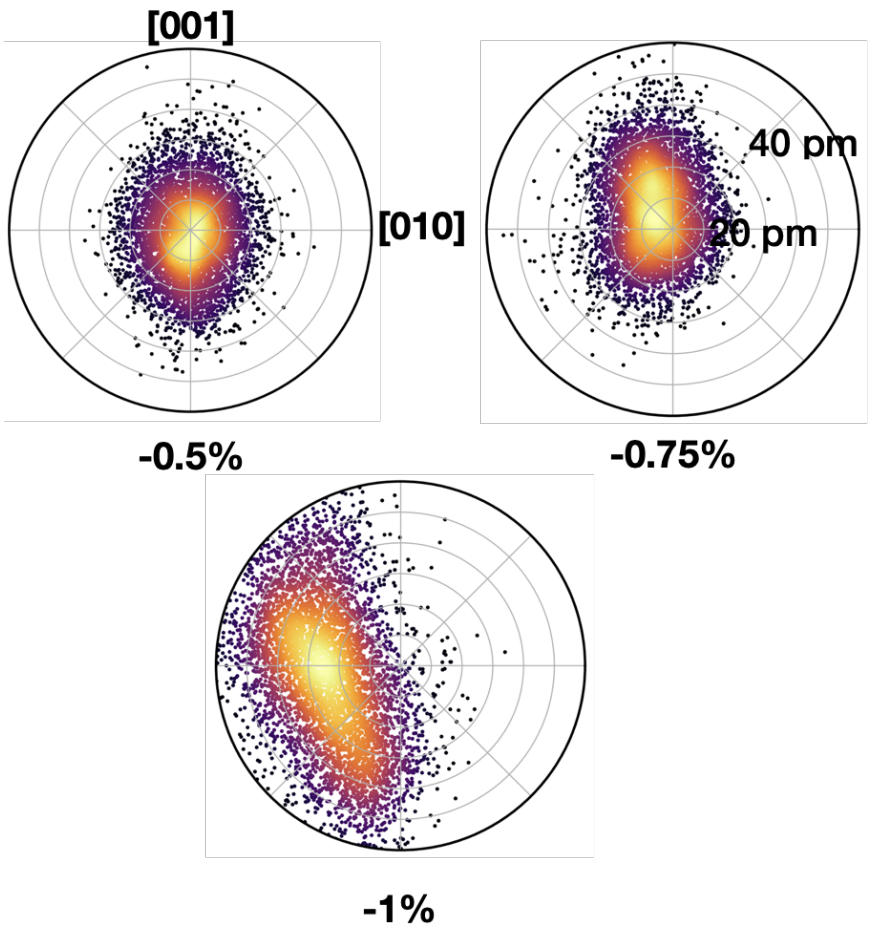

Figure 5-5: Polar vector plot of net displacement vectors for -0.5%, -0.75% and -1% strained thin films

output strain values from films under an applied electric field are calculated from the lattice parameter obtained in in-situ X-ray diffraction measurements. The polar structure from STEM imaging and diffuse scattering features from X-ray scattering indicate that a mixture of short and long-range polar order domains allows easier domain reorientations and thus leads to higher strain. An explanation based on crystal structure can also be proposed to explain the higher electromechanical response of the intermediate strained film. From X-ray measurements [104], -0.5% strained film shows an average rhombohedral structure while -1% has a dominant tetragonal structure. In the intermediate strain state, the monoclinic phase has been found predominantly, leading to a higher electromechanical response. This is similar to the bulk PMN-PT where the amount of monoclinic-like distortions correlates with the composition-

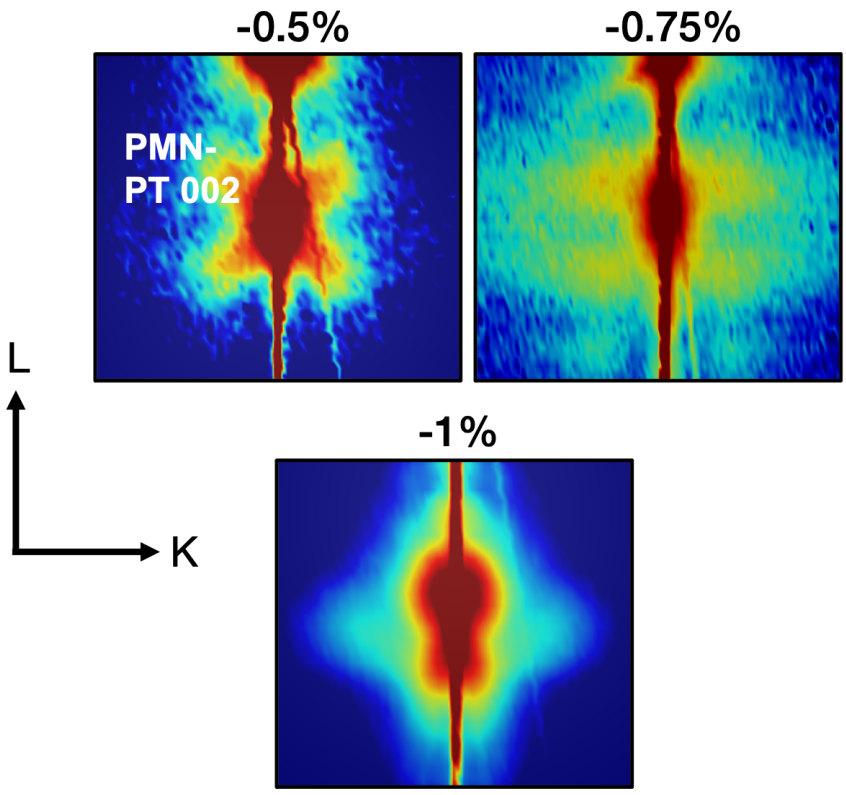

Figure 5-6: Diffuse scattering features across 002 diffraction peak obtained in reciprocal space mapping of PMN-PT thin films using X-ray scattering. K & L represent reciprocal lattice vectors 010 and 001, respectively. Used with permission of John Wiley & Sons - Books, from Ref. [55]; permission conveyed through Copyright Clearance Center, Inc. ©2019 WILEY-VCH Verlag GmbH & Co. KGaA, Weinheim

dependent electromechanical response in bulk PMN-xPT, as discussed in chapter 3.

Directional dependence of the polar structural changes is also determined based on differences in polar displacement components along out-of-plane [001] (Figure 5-3) and in-plane [010] (Figure 5-4) directions. Polar components along two directions show significant differences indicating strong directional dependence for polar structural evolution. The polar component along the out-of-plane direction [001] reveals an increase in the size of opposite polarity domains (indicated by red and blue) with higher strain along the growth direction [001]. The film with -0.5% strain shows either horizontally aligned domains of width 1-2 nm along [001] or $\sim 45^{\circ}$ inclined domains. At a higher strain of -1%, the width of the opposite polarity domain increases to 10-15 nm. Polar components along the in-plane [010] direction also revealed an increase in

domain size with strain but along the in-plane direction only. The in-plane domain size changes from 5-6 nm for -0.5% to 15-20 nm for -1% strained thin films.

Further, polar or net displacement vectors are visualized using polar plots to quantify the changes in polarization, as shown in Figure 5-5. The mean displacement magnitude becomes almost double from 15 to 35 pm, with an increase in strain from -0.5% to -1%. The doubling of mean magnitude is due to structural changes in the lattice with the strain, which favors the formation of long-range polar order. Despite the formation of long-range polar order in -1% strain, the angular distribution of the polar vectors shows a broad spread indicating the presence of small fluctuations in polarization within the long-range polar order.

As observed using STEM, polar structure evolution is also consistent with molecular dynamics simulation results for strained PMN-PT thin films [55]. MD simulation reveals a strong directional dependence of polar structure evolution similar to STEM results. An increase in polar domain size is observed along [001] with an increase in strain to -1% . The formation of long-range polar order with high-angle domain walls is also observed in MD simulated structure consistent with STEM results. The increase in polar ordering with strain also correlates to a decrease in strength of relaxor behavior as quantified by frequency-dependent shifts in temperature maxima of the dielectric permittivity curve [15]. The strength of a relaxor is parameterized by ΔT_{max} values which indicates the dielectric relaxational character of these relaxors [15]. The ΔT_{max} value decreases from 25 to 15 K with increased strain from -0.5% to -1% [55]. This indicates that highly strained PMN-PT films are weak relaxors, which correlate with an increase in polar ordering, as revealed from STEM results. This also provides evidence that polar correlations strongly influence the relaxational character existing in the materials. Thus, epitaxial strain from the substrate can be realized to modify the polar structure and eventually the strength of relaxational character (stronger or weaker) in PMN-PT thin films. Relaxors with controlled polar structures with varying strain will also allow studying correlations among electromechanical, electrocaloric, and optical responses of relaxors with their structure which is still missing.

5.2 Local structure Vs. Chemistry

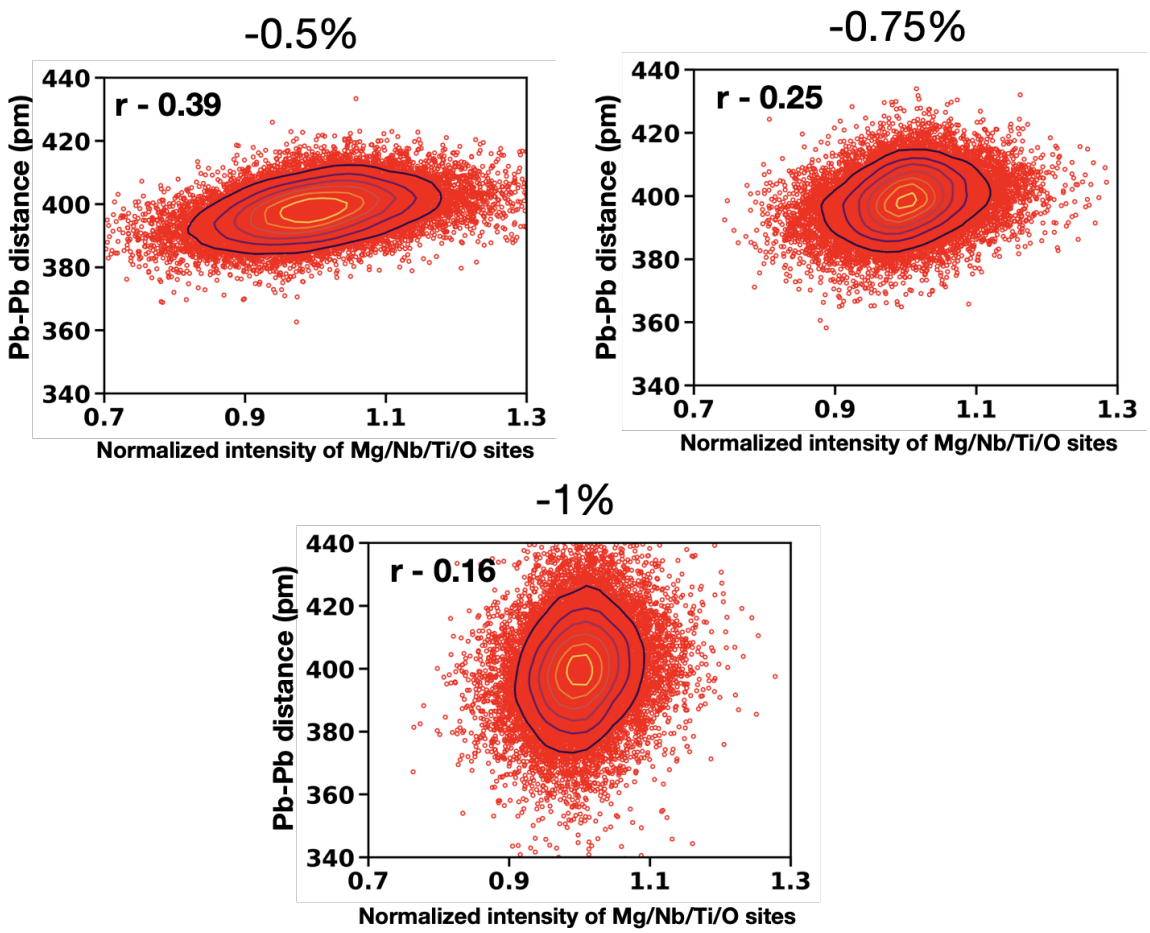

Figure 5-7: The plot of average Pb-Pb distance with normalized ADF-STEM image intensity of Mg/Nb/Ti/O sites for -0.5% and -1% strained PMN-PT thin films

The local distortions in relaxors have also been found to be correlated with the changes in the local distribution of constituent atoms, as observed in Chapter 3. To understand the effect of strain on the correlation between local distortion and local chemistry, the average lead-lead distances around each B-site sublattice position (containing magnesium, niobium, titanium, and oxygen in projection) are plotted with respect to its normalized intensity obtained from the chemically sensitive ADF images (Figure 5-7). Approximately 20,000 unit cells are used from each strained film for this analysis. Notably, for the -0.5% strained film, a correlation is found between the normalized B-site sublattice intensity and the nearest-like-neighbor lead-

lead distances with a Pearson correlation coefficient r = 0.39. As strain increases, the correlation shows a decrease (r = 0.25) for the intermediate -0.75% strain. No correlation (r = 0.16) is found for the -1.0% strained relaxor film. This decrease in the correlation between local chemistry and distortion with higher strain indicates that strain dominates the lead displacements regardless of variation in local chemistry. The decoupling of Pb displacements from local chemistry with higher strain also relates to the decreased strength of the relaxor (ΔT_{max}) in strained thin films. Both the Pearson correlation coefficient which quantifies the coupling among local structure and chemistry, and ΔT_{max}, which represents the strength of a relaxor, show a decreasing trend with an increase in strain. This suggests that the strength of local chemistry and structure coupling also plays a key role in determining the strength of relaxors, mainly in their dielectric relaxational character.

5.3 Chemical ordering

The effect of epitaxial strain has also been observed in local chemical distribution and chemical ordering in strained PMN-PT thin films. Chemical ordering of β_I (Mg-rich) and β_{II} (Nb-rich) atomic sites along 110 have been observed in PMN-xPT systems. As discussed in Chapter 3, in bulk PMN-PT samples, these chemical-ordered regions are found to create the polarization barrier, leading to the formation of a nanoscale domain structure. This chemical ordering also varies with chemical composition as these decrease with an increase in PT content in the system. In thin films grown using pulsed laser deposition, PMN-32PT shows chemical-ordered regions, as discussed in chapter 4. The spatial distribution of chemical ordered regions also shows variation with varying epitaxial strain. Chemical ordering observed in chemically sensitive high-angle annular dark field (HAADF) STEM along [110] projection is identified using a kernel correlation method as discussed in chapter 3. Chemical order maps are generated for -0.5% , -0.75 %, and -1% coherently strained thin films, shown in Figure 5-8. Thin film with -0.5 % strain reveals the chemical-ordered regions of size 2-3 nm. With an increase in strain, the size of these ordered regions increases to

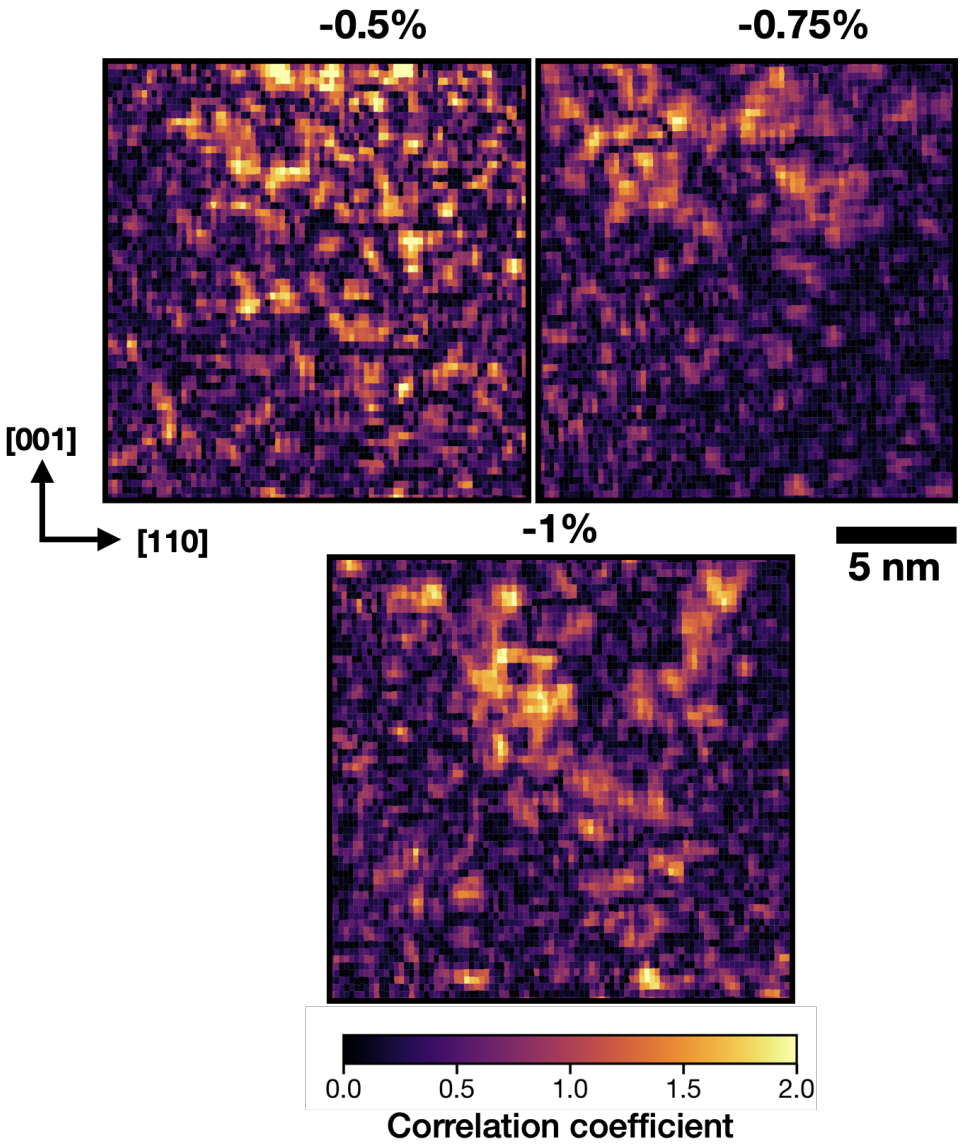

Figure 5-8: The correlation coefficient map of chemical ordering was calculated from the normalized HAADF intensity map for -0.5% and -1% strained PMN-PT thin films .

4-5 nm for -0.75 % strain film. At a higher strain of -1 %, the size and shape of these chemically ordered regions change. These ordered regions become asymmetric in shape with 6-8 nm length along the elongated direction. The total percentage of the projected area of the image covered by chemical ordering remains the same across all strained films. This indicates that total chemical ordered regions are determined by the overall composition of the film, which remains constant across all strained

films as measured from RBS.

The total projected area covered by chemical ordered regions remains constant, while the size of individual ordered regions suggests variation in spatial density of these ordered regions across strained films. Figure 5-8 shows a higher spatial density of these chemically ordered regions in -0.5% strained film than in -1% films. Chemically ordered regions at higher strained thin films reveal clustering of these ordered regions. This can be explained due to the distinct differences in electrostatic and mechanical behavior among order and disorder regions, as indicated in the literature[22]. While lower epitaxial strain favors the formation of randomly distributed smaller chemical ordered regions, with higher strain, these clusters to minimize the interfacial volume between ordered and disordered regions. This behavior of chemically ordered regions is similar to defect clustering in off-stoichiometric $SrTiO_3$ with higher local strain due to the distinct mechanical and electrostatic nature of individual defects [106]. An increase in chemical ordered regions also suggests an increase in polar ordering with strain as these correlate with domain walls (as discussed in chapter 3). Thus higher strained state would lead to fewer domain wall regions than -0.5%. This is consistent with polar structure observations that revealed the presence of long-range polar order with higher strain and thus a lower number of domain walls compared to -0.5% strained films. Such polar structural changes that arise from local chemical distribution also relate to the decreasing strength of the relaxor (ΔT_{max}) with the higher strain as obtained from dielectric measurements from these films. This indicates that local chemical distribution influences polar structure evolution, which eventually affects a relaxor's strength. Thus, this reveals that local chemistry, structure, and properties are coupled in these heterogeneous relaxor systems.

The extent of chemical ordering defined by order metric is calculated as correlation coefficients based on kernel correlation on normalized intensity map (discussed in chapters 3 & 4). The chemical order metric also varies with epitaxial strain, as shown in Figure 5-9. Thin film with -0.5% strain shows an increasing chemical order metric across the thickness. This is consistent with the variation of film composition across the thickness, as discussed in chapter 4. Higher Ti content near the PMN-PT/BSRO

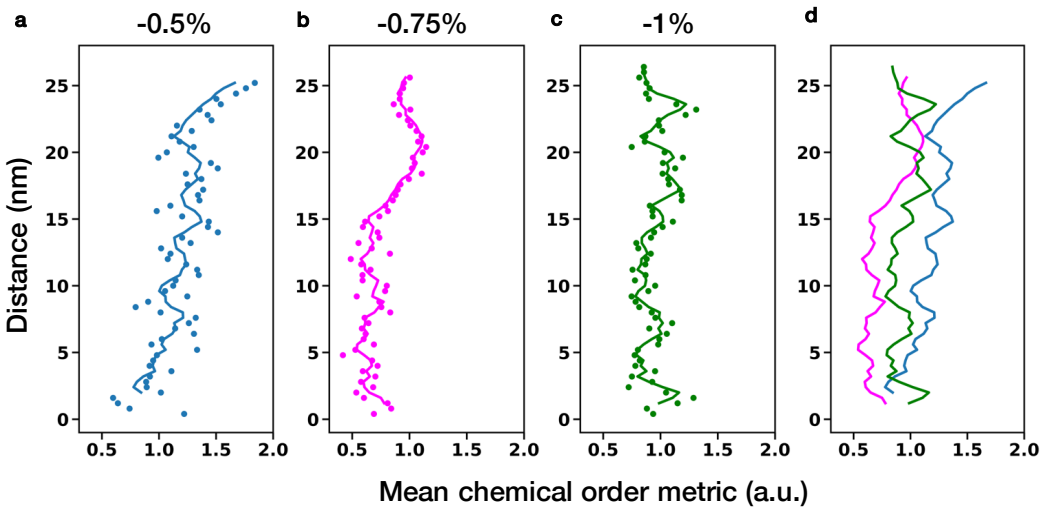

Figure 5-9: The plot of the mean chemical order metric across thickness in PMN-PT thin films with (a) -0.5%, (b) -0.75% , (c) -1% epitaxial strain and (d) combined moving average plots of mean chemical order metric from all strained films

interface favored by epitaxial strain leads to lower chemical ordering. Film regions away from the interface show higher chemical ordering due to random nucleation of these ordered regions. Higher strain film shows a lower order metric as compared to -0.5% film, shown in Figure 5-9d. This can arise from differences in the amount of Ti content in these ordered regions across strained films. Further, atomically resolved spectroscopy (EDS or EELS) measurements will be required in the future to confirm such variation in Ti distribution across ordered regions with varying strains. These preliminary results indicate that epitaxial strain also leads to variation in local chemistry in relaxors and polar structures.

5.4 Conclusions

In conclusion, the polar domain structure varies with epitaxial strain in PMN-PT relaxor thin films. Lower strained thin films (-0.5%) show asymmetric domains with short-range polar order. At a higher strain of -1%, the formation of long-range polar order is observed along with high-angle domain walls similar to normal ferroelectrics. Such polar structure evolution with strain as observed in STEM is consistent with

molecular dynamics simulations. A decrease in correlation among local lattice parameters and chemistry is also observed with an increase in strain value, indicating the decoupling of local lead displacements with chemistry at higher strain. Further, chemical ordering behavior also shows variation with epitaxial strain. The chemical ordered region size increases with strain while their spatial density decreases across higher strained films. This indicates that the distribution of local chemistry is also strongly influenced by epitaxial strain in films. The decrease in spatial density of chemical ordered regions with higher strain is consistent with the increase in polar ordering. In a bulk PMN-PT system, these chemically ordered regions are found to act as polarization barriers (as discussed in chapter 3) thus, creates domain walls. A decrease in spatial density of these ordered regions leads to fewer domain walls thus, increases the polar ordering. The polar ordering correlates with the strength of relaxor behavior obtained from dielectric measurements. An increase in polar ordering with strain as determined by the spatial distribution of inhomogeneities such as chemical ordered regions indicates to have weaker relaxational character. This suggests the complex coupling among local chemistry, polar structure and properties in terms of the strength of dielectric relaxational character in these epitaxially strained thin films. These strained films also enable tuning properties correlated with their polar structure in a controlled manner.

Chapter 6

Stoichiometric-controlled ferroelectricity in orthoferrite yttrium iron oxide thin films

Some figures and part of the text in this chapter is from ref[2] and reproduced with permission from Springer Nature as cited, "The author of articles published by Springer Nature do not usually need to seek permission for reuse of their material as long as the journal is credited with initial publication. Ownership of copyright in original research articles remains with the Author, and provided that, when reproducing the contribution or extracts from it or from the Supplementary Information, the Author acknowledges first and reference publication in the Journal". In this chapter, some figures and part of the text are also used with permission of John Wiley & Sons - Books, from ref. [3]; permission conveyed through Copyright Clearance Center, Inc as cited, " Use of proper copyright notice for a Work is required as a condition of any License granted under the Service. Unless otherwise provided in the Order Confirmation, a proper copyright notice will read substantially as follows "Used with permission of John Wiley & Sons - Books, from ref. [3] [Antisite Defects Stabilized by Antiphase Boundaries in $YFeO_3$ Thin Films, Abinash Kumar, Konstantin Klyukin, Shuai Ning, Cigdem Ozsoy-Keskinbora, Mikhail Ovsyanko, Felix van Uden, Ruud Krijnen, Bilge Yildiz, Caroline A. Ross, and James M. LeBeau, Adv. Funct. Mater.,

32, 9, 2021]; permission conveyed through Copyright Clearance Center, Inc." Such notice must be provided in a reasonably legible font size and must be placed either on a cover page or in another location that any person, upon gaining access to the material which is the subject of a permission, shall see, or in the case of republication Licenses, immediately adjacent to the Work as used (for example, as part of a by-line or footnote) or in the place where substantially all other credits or notices for the new work containing the republished Work are located. Failure to include the required notice results in loss to the Rightholder and CCC, and the User shall be liable to pay liquidated damages for each such failure equal to twice the use fee specified in the Order Confirmation, in addition to the use fee itself and any other fees and charges specified."

The main objective of this chapter is to determine the structural origin of unconventional ferroelectric behavior in orthoferrite $YFeO_3$ thin films obtained with stoichiometry control. Y-rich YFO (Y/Fe $>$ 1) thin films show ferroelectric ordering, while Fe-rich (Y/Fe $<$ 1) films reveal no ferroelectricity. Here, I identify the presence of antisites and antiphase boundaries (APBs) in ferroelectric Y-rich YFO thin films. STEM-EDS mapping shows Y_{Fe} antisites distributed across the ferroelectric thin films. Convergent beam electron diffraction indicates breaking of inversion symmetry in the presence of Y_{Fe} antisites in Y-rich film, stabilizing the ferroelectric ordering. In contrast, APBs in Y-rich films are found to host Fe_Y antisites that are not observed elsewhere in the film. These APBs reveal significant lattice relaxation. Using the structure observed from STEM images, density functional theory (DFT) predicts APBs with Fe_Y antisite also lead to bi-stable polar distortions with lower polarization switching barrier in YFO thin films. The lower density of APBs across Y-rich film as compared to the amount of Y_{Fe} antisites indicates antisites have significant contributions in determining the ferroelectric response from Y-rich YFO films.

In this study, the stoichiometry-controlled YFO thin films were provided by Dr. Shuai Ning and Prof. Caroline Ross at the Massachusetts Institute of Technology. The polarization measurements with applied electric field and switching spectroscopy

piezoresponse force microscopy on YFO thin films were performed by Dr. Shuai Ning under the guidance of Prof. Caroline Ross. The density functional theory calculations were performed by Dr. Konstantin Klyukin under the guidance of Prof. Bilge Yildiz at the Massachusetts Institute of Technology. The atomic resolved STEM-EDS maps from the antiphase boundary were collected by Dr. Cigdem Ozsoy-Keskinbora, Dr. Mikhail Ovsyanko, Dr. Felix van Uden and Dr. Ruud Krijnen at Thermo Fisher Scientific, Netherlands.

6.1 Stoichiometry-controlled YFO thin films

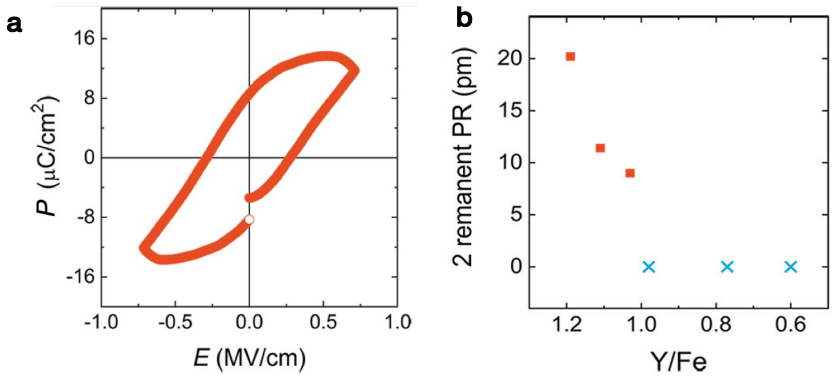

Figure 6-1: (a) Polarization–electric field hysteresis loop measured at room temperature from Y-rich YFO thin films (Y/Fe - 1.19) and (b) remanent piezoresponse on YFO films with varying Y/Fe ratio. From Ref[2] and reproduced with permission from Springer Nature.

Stoichiometry-controlled YFO thin films were grown by pulsed laser deposition on Nb-doped $SrTiO_3$ [2]. YFO thin films with varying compositions in terms of Y to Fe ratio from 0.6 to 1.19 were obtained. These film compositions were determined by X-ray photoelectron spectroscopy. Y-rich YFO thin film with Y/Fe of 1.19 shows ferroelectric polarization at room temperature, revealed by the hysteresis loop behavior of measured polarization with an applied electric field, shown in Figure 6-1a. A remanent polarization of 10 μ C/cm^2 and a coercive field of 0.3 MV/cm is found. No hysteresis loop is observed for Fe-rich YFO thin films. Ferroelectricity in YFO thin films with varying stoichiometry is further validated by switching spectroscopy

piezoresponse force microscopy (SS-PFM). This also reveals piezoelectric hysteresis for thin films with Y to Fe ratio > 1. The remanent piezoresponse measured from these films shows a gradual decrease with Y/Fe ratio, as shown in Figure 6-1b. This indicates clear dependence of ferroelectric behavior on the stoichiometry of the film.

YFO thin films were also grown on different substrates with varying lattice parameters, $DyScO_3$ (DSO), $La_{0.67}Sr_{0.33}MnO_3$ (LSMO)-buffered $(LaAlO_3)_{0.3}$–$(SrAl_{0.5}Ta_{0.5}O_3)_{0.7}$ (LSAT), and LSMO-buffered $LaAlO_3$ (LAO). This allows to apply epitaxial strain from the substrate due to differences between the lattice parameter of substrate and YFO. SS-PFM measurements on YFO thin films grown on different substrates still reveal ferroelectric behavior in Y-rich YFO films with even 2% strain. Films with varying thicknesses from 10-100 nm reveal similar ferroelectric responses in Y-rich films. This suggests a minor role of epitaxial strain and film thickness in determining ferroelectric behavior, thus requiring the atomic scale understanding to determine the structural origin of unconventional ferroelectricity in stoichiometry-controlled YFO thin films.

STEM imaging was performed on Y-rich and Fe-rich YFO thin films in cross-sections (Figure 6-2). Image contrast in HAADF and BF-STEM images reveal that both Y and Fe-rich YFO thin films show mosaicity and different orientations. To determine the overall film composition, STEM-EDS mapping was performed on YFO thin films, as shown in Figure 6-3. Y-rich thin films reveal uniform composition with a Y/Fe ratio of 1.21 while the Fe-rich sample shows compositional heterogeneity with regions having Y/Fe ratios of 0.528 and 1.09 and overall composition with a Y/Fe ratio of 0.99.

6.2 Y_{Fe} antisites

Atomically-resolved STEM EDS (Figure 6-4) collected on the YFO/NSTO sample with 20% excess Y reveals the presence of Y ions at Fe sites, i.e., Y_{Fe} defects. Based on the composition and the lamella thickness (11 nm), average 2-3 antisite defects are expected in each Fe-O atom column. As discussed in chapter 2, STEM-EDS has

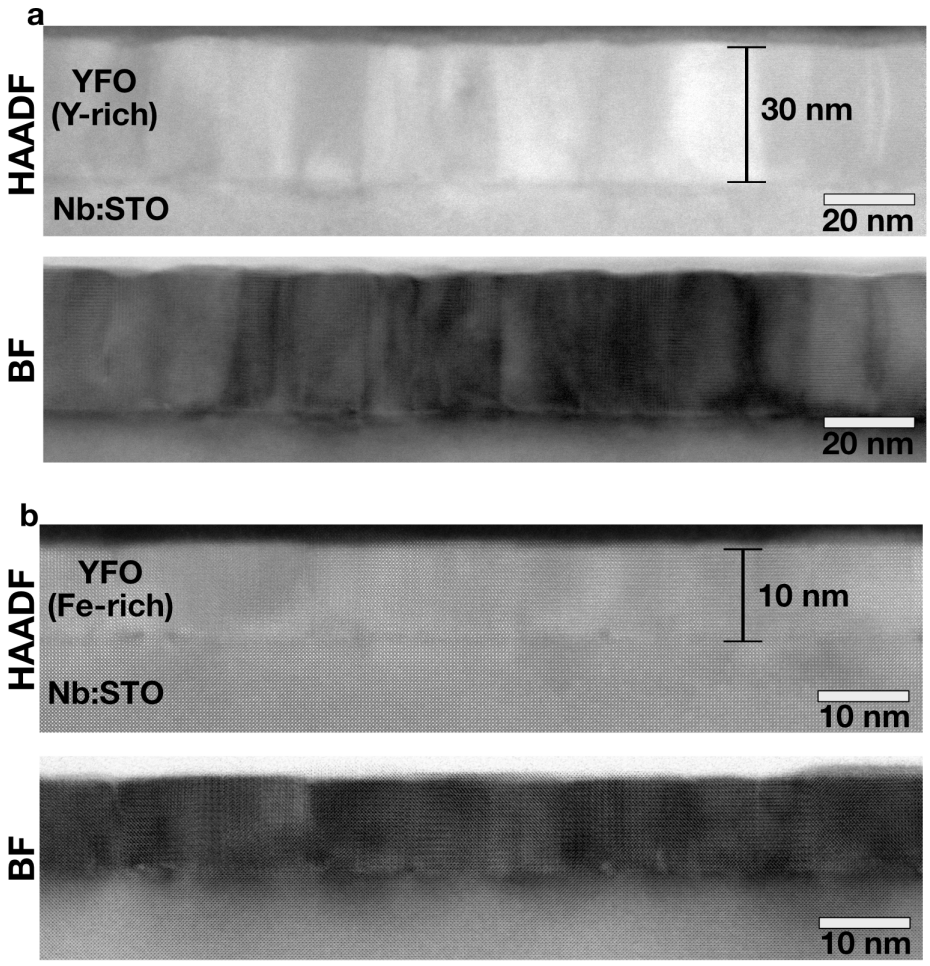

Figure 6-2: High-angle annular dark-field (HAADF) and bright-field (BF) STEM images of (a) Y-rich and (b) Fe-rich YFO thin films. From Ref[2] and reproduced with permission from Springer Nature.

lower collection efficiency and thus has lower sensitivity to resolve small numbers of antisite defects. This indicates that significant EDS intensity observed in the Y elemental map for Fe atom columns contains a statistically larger number of Y_{Fe} antisite. Further analysis of the simultaneously acquired, atomic number (Z) sensitive high-angle annular dark-field (HAADF) STEM reveals an increase in atom column intensity of 10-20% at these locations (Figure 6-5), confirming the presence of Y (Z=39) in the Fe (Z=26) sites. STEM-EDS from Fe-rich YFO films reveals no Y_{Fe} antisites. These also show lower EDS intensity at a few Y atomic columns indicating the presence of Y vacancies in the thin films.

Position-averaged convergent beam electron diffraction (PACBED) in STEM can

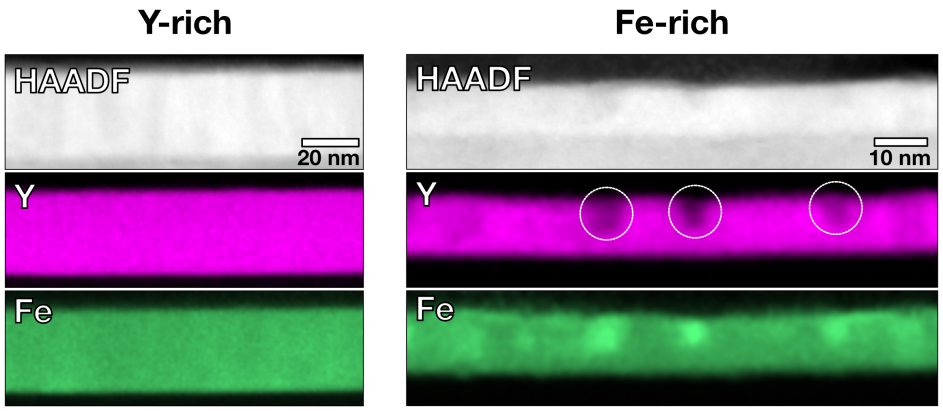

Figure 6-3: STEM EDS elemental map of Y-rich and Fe-rich YFO thin films. From Ref[2] and reproduced with permission from Springer Nature.

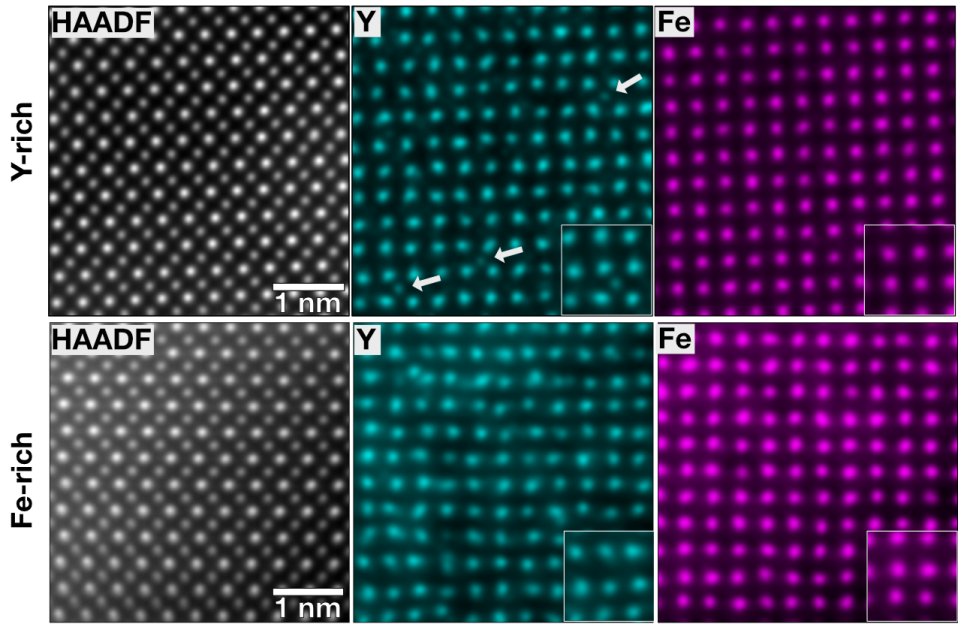

Figure 6-4: HAADF-STEM image and denoised atomic resolution STEM EDS elemental maps for Y and Fe-rich YFO thin films. From Ref[2] and reproduced with permission from Springer Nature.

reveal changes in the local symmetry of a crystal [107]. This also shows higher sensitivity to the inversion center symmetry breaking, thus used to confirm the crystallographic origins of ferroelectricity in Y-rich YFO thin films. The experimental PACBED pattern is compared to the simulated diffraction pattern from bulk centrosymmetric, Pbnm structure and non-centrosymmetric, R3c structure as predicted by density functional theory (DFT) due to Y_{Fe} antisites (Figure 6-6). The experimen-

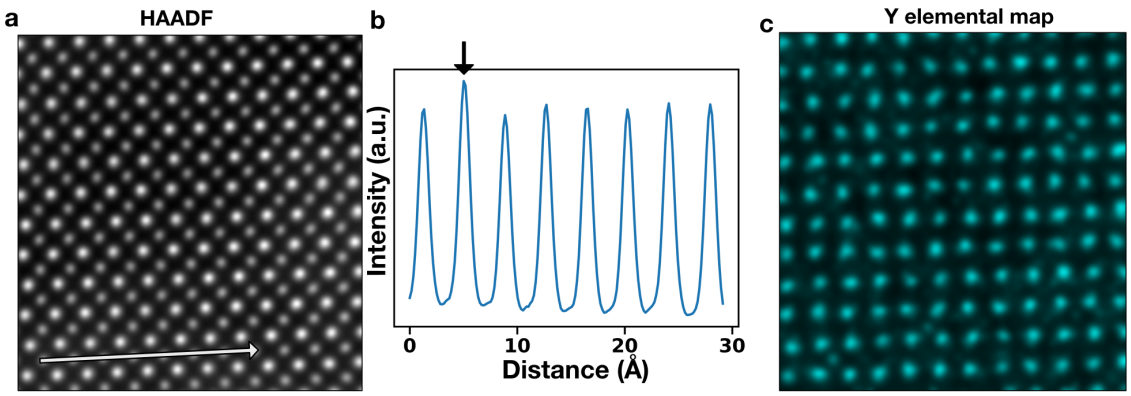

Figure 6-5: (a) HAADF-STEM image of the Y-rich YFO film, (b) HAADF STEM intensity profile along the line shown in (a), and (c) Y elemental map from STEM-EDS measurements. Increased intensity at Fe-O atom column, as highlighted by arrow contains Y_{Fe} defects. From Ref[2] and reproduced with permission from Springer Nature.

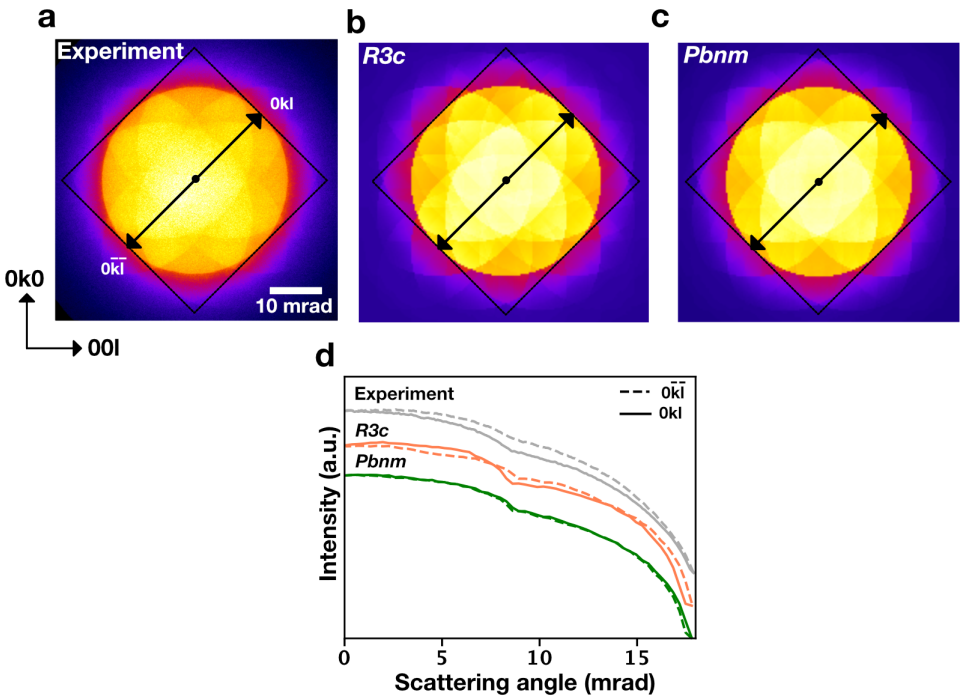

Figure 6-6: (a) Experimental PACBED patterns from Y-rich YFO thin films, (b) & (c) shows simulated patterns, using the DFT relaxed centrosymmetric Pbnm and non-centrosymmetric R3c structure respectively, and (d) intensity profiles, integrated across the PACBED pattern diagonals. From Ref[2] and reproduced with permission from Springer Nature.

tal pattern exhibits an asymmetric feature, i.e., a mismatch of intensity profiles be-

tween [0kk] and $[0\bar{k}\bar{k}]$ directions, as shown in Figure 6-6d. This is consistent with the simulated PACBED patterns from the non-centrosymmetric R3c structure but differs from the centrosymmetric Pbnm pattern where the intensity profile along [0kk] coincides exactly with that along $[0\bar{k}\bar{k}]$. This indicates that local structural changes from Y_{Fe} antisites lead to inversion symmetry breaking that can support ferroelectricity in Y-rich YFO thin films.

6.3 Antiphase boundaries

Annular dark-field (ADF) and differentiated differential phase contrast (dDPC) STEM imaging allow identifying defects across the thin films, as shown in Figure 6-7a,b. Two APBs, indicated by arrows at the top of Figures 6-7a,b, occur where the zigzagging of the Y atom columns is mirrored on either side of the boundaries (see chevron lines in Figure 6-7), and represents a translation of $\frac{c}{2}[001]$ in the (110) plane. Further, the APBs are found throughout the thin film with a lateral density of about 0.2 APB/nm. While interface misfit dislocations are observed, marked with the arrows in Figures 6-7a, and b, they do not correlate with APB formation. Misfit dislocations and the relaxed in-plane lattice parameter indicate that the formation of APBs is not directly related to the relaxation of strain but rather the selection of the growth plane based on the mismatch of the film with the STO substrate.

Unlike APBs in cubic perovskites, such as $SrTiO_3$, the APB defects seen here do not arise from off-stoichiometry in the film. The boundaries are generated by a half-unit-cell translation along the doubled pseudocubic unit cell direction, [001], and hence stoichiometry is maintained. Furthermore, the APBs do not correlate with substrate surface steps and the YFO d_{002} spacing is nearly that of STO, with a -2.7% lattice mismatch. Thus, an APB would not be required to accommodate steps on the $SrTiO_3$ surface [108]. Moreover, the APBs are found throughout the film occur at random positions. Only vertical APBs are found in the films, which originate at the film/substrate interface. Thus the density of such planar defects is not strongly affected by sample thickness. Instead, the density control is primarily governed by the

thin film nucleation and growth rate. For example, a previous YFO thin film growth study [109] showed that vertical planar defects initiated at the YFO/STO interface and extended through even an 800 nm thick film.

Further, nucleation of YFO on either $(001)_{\mathrm{YFO}}$ or $(002)_{\mathrm{YFO}}$ exhibits the lowest mismatch relative to STO. Specifically, growth on $\{110\}_{\mathrm{YFO}}$ would require the accommodation of -2.7% strain compared to -1.6% for $\{001\}_{\mathrm{YFO}}$ (Figure 6-7d). In addition, the $(001)_{\mathrm{YFO}}$ and $(002)_{\mathrm{YFO}}$ nuclei can be equivalently initiated on the STO substrate surface where only the Fe-oxygen octahedral tilts are different in the first Fe-O layer of YFO, as shown in Figure 6-7c. Thus, the vertical APBs in the YFO thin film are the product of the coalescence of regions nucleated on $(00L)_{\mathrm{YFO}}$ type planes during PLD.

6.4 Fe_Y antisites stabilized by antiphase boundaries

High-angle ADF (HAADF) and atomic resolution energy dispersive X-ray spectroscopy (EDS) confirm that the APBs are nominally composed of Y, as shown in Figures 6-8a,b as expected from the formation mechanism. Further, the Y EDS map shows that Y_{Fe} antisites form throughout the film, as discussed before. The Fe EDS map, on the other hand, indicates that Fe_Y resides at the APB, as in Figure 6-8c. Further, they are placed at every other Y atom column in the APB. This observation strongly suggests that while the formation energy of Fe_Y antisites is high in '*bulk*' [2], it is significantly decreased at the APBs. The background-subtracted Fe signal from EDS at the Y sub-lattice on APB suggests that an average of about 10% of Y atoms are replaced by Fe atoms. In a 10 nm thick TEM sample, this represents roughly 2-3 Y atoms replaced by Fe. This contrasts with a previous report of APBs in the orthomanganite $TbMnO_3$, where Mn replaced all (or nearly all) Tb and created a new 2D phase[110]. Also, no significant change in oxygen content is observed at the APBs based on the intensity of oxygen atom columns in the dDPC images as shown in Figure 6-7c and X-ray absorption spectroscopy (XAS) measurements show that Y and Fe are in 3+ charge states[2], consistent with oxygen stoichiometry.

To further explore the APBs, structural relaxations at the boundary are measured. The nearest-like-neighbor (NLN) distances for Y are shown in Figure 6-9a. Notably, the Y atom columns align vertically along $[001]_{YFO}$ at the APB in contrast to the zigzag to either side of the boundary. Furthermore, the in-plane Y-Y NLN distances alternate between expansion and contraction by 15% while the in-plane Fe-Fe NLN distances remain constant across the boundary. In contrast, the out-of-plane NLN distances for Y-Y are unchanged and the Fe-Fe distances alternately expand and contract by 7%. The oxygen atom positions also relax at the boundary, where along [001] the projected oxygen positions move towards the Y atom column within the expanded lattice environment, as shown in Figure 6-7c. These changes represent a significant departure from the 'pristine' crystal structure, and hence the bonding environment is considerably different at the APB.

The net cation displacements at the APB, measured as the difference between the position of a Fe atom column and the centroid of its four surrounding Y atom columns, reflect the departure from the bulk structure symmetry. The average net cation displacement magnitude in Figure 6-9c is 9±3 pm at the APB and only 6±3 pm away from the boundary. The net cation displacements can thus be understood as inversion symmetry breaking that leads to polarization at the APB. From these measurements of the projected structure, the APBs exhibit ferrodistortive displacements, with the largest component of polarization along the in-plane direction.

The combination of polar displacements and the presence of Fe_Y antisites strongly suggests that the properties differ significantly at the APBs. Exploring this further, DFT is used to relax the structure of the APB measured from the experiment, which was then used to estimate formation energies and local polarization with and without Fe antisites, Figures 6-10d,e. To confirm that the DFT APB structure agrees with the experiment, ADF STEM images are simulated using relaxed DFT structures, Figures 6-10f,g. The measured magnitude of the net cation displacement using the simulated APB images was 6 pm with and 9 pm without the Fe_Y antisite, respectively. Furthermore, the Y and Fe sublattices at the APB of the DFT-relaxed structure also expand and contract by 16% (along in-plane) and 8% (along out-plane). The DFT

structure is thus in excellent agreement with the experiment.

The formation energy of the observed APBs is found to be 130 mJ/m^2 from DFT, which is within the range typical for perovskite oxides (100-300 mJ/m^2) [111, 112]. The low boundary formation energy further supports the nucleation and growth model suggested above as the boundaries can form without a large energy penalty. Furthermore, the DFT calculations indicate that the Fe_Y antisites are stabilized by the APBs where the antisite formation energy is decreased ($\Delta E = -0.31$ eV) at the compressive strain locations (see Figure 6-10a). This is significant as at these Y positions, the Y-O distance is only 2.23 Å compared to 2.29 Å away from the boundary. Thus, the replacement of Y by Fe is favored here because of Fe's smaller ionic radius, which reduces the compressive strain energy. This is in contrast to the Y APB positions with tensile strain, where a significant increase ($\Delta E = 0.59$ eV) of the Fe_Y formation energy occurs. Furthermore, the DFT calculations also show that while the electronic structure of Fe-rich APB remains insulating, empty states associated with the Fe_Y defects (see Figure 6-10b) may serve as charge traps and promote p-type conductivity.

As with experiment, in-plane polarization induced by the APBs is also found in the first-principles simulations. The DFT structure shows that in-plane polarization originates from significant off-centering (0.71 Å) of the central Y atom at the APB as shown in Figure 6-10c, which polarizes adjacent layers and causes sizable octahedral distortions. The resulting bi-stable polarization is 19 μC/cm^2 along $[110]_{YFO}$ with a switching barrier of 0.44 eV/APB. Moreover, bi-stable APBs have also been shown to occur in other perovskite oxides [112]. When Fe_Y antisites are added to the APBs, the off-centering is reduced by more than a factor of three, 0.2 Å, which leads to a decreased ferroelectric polarization of 7.6 μC/cm^2 (Figure 6-10c). The smaller displacement along $[110]_{YFO}$ in the DFT relaxed structure is associated with the smaller ionic radius of Fe^{3+} compared to Y^{3+} and ultimately reduces the switching barrier to 0.15 eV/APB. This is significant as a boundary without Fe_Y antisites would exhibit a large switching barrier and could thus act to pin polarization, which can degrade switching behavior. Thus, although the YFO APBs are predicted to exhibit in-plane

polarization, their contribution to polarization is reduced by the Fe_Y antisites, and at the density, as observed here, APB is not the dominant contributor to the measured ferroelectric polarization. Instead, the out-of-plane ferroelectric response still remains dominated by the Y_{Fe} antisites in these YFO thin films.

6.5 Conclusion

The structural origin for unconventional ferroelectricity in stoichiometric-controlled YFO films is determined with STEM imaging and spectroscopy. Y_{Fe} antisites are found across YFO thin films with about 20% excess Y while absent in Fe-rich films. These antisites induce breaking of inversion symmetry in YFO and thus stabilize the ferroelectricity. Planar defects such as APBs are also found, which exhibit significant structural relaxation of the Y, Fe, and O sub-lattices at the boundary. The combination of STEM measurements with DFT calculations shows that the APBs provide a local structural and chemical environment that considerably lowers the formation energy of Fe_Y antisites. The local distortions at the APBs are also shown to be ferrodistortive (in-plane) in nature, which is modified by the presence of Fe_Y defects. APBs show significantly lower density across the YFO films indicating ferroelectricity in YFO films arises predominantly from Y_{Fe} antisites.

with

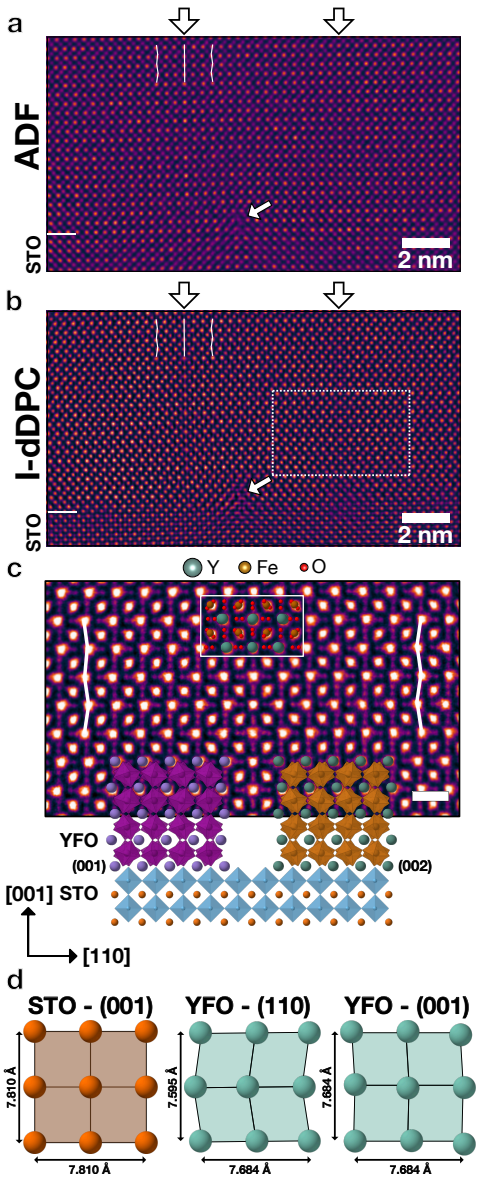

Figure 6-7: (a) ADF and (b) Inverted dDPC (I-dDPC) STEM images of the Y-rich YFO thin film grown on Nb:STO. The horizontal lines at the left mark the film/substrate interface, while the arrows and chevrons indicate the positions of APBs. The arrows inside the figure indicate a misfit dislocation. (c) An atomic resolution I-dDPC image highlighting the cation and anion positions across the APB, where the inset provides the DFT relaxed structure. The schematic shows that the (110) APB forms as a result of the initial growth plane [(001), left or (002), right] at the substrate. The arrow indicates positions where the projected O-O distance decreases at APB. The scale bar represents 500 pm. (d) Schematic of the cation arrangement in the (001) of STO, and the (110) and (001) of YFO. The distances between the doubled pseudocubic perovskite unit cells are shown in each case. Used with permission of John Wiley & Sons - Books, from Ref. [3]; permission conveyed through Copyright Clearance Center, Inc. ©2021 Wiley-VCH GmbH

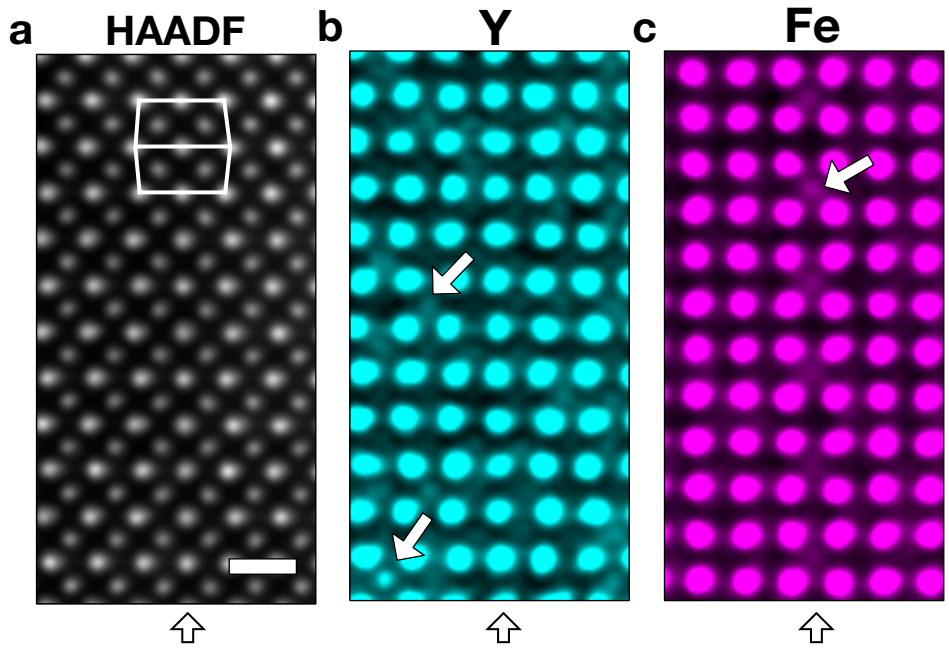

Figure 6-8: (a) HAADF STEM of an (110) antiphase boundary in YFO and corresponding (b) Y and (c) Fe STEM EDS maps. The scalebar represents 500 pm. The arrows in (b) and (c) point to atom columns containing Y_{Fe} and Fe_Y antisites, respectively. Used with permission of John Wiley & Sons - Books, from Ref. [3]; permission conveyed through Copyright Clearance Center, Inc. ©2021 Wiley-VCH GmbH

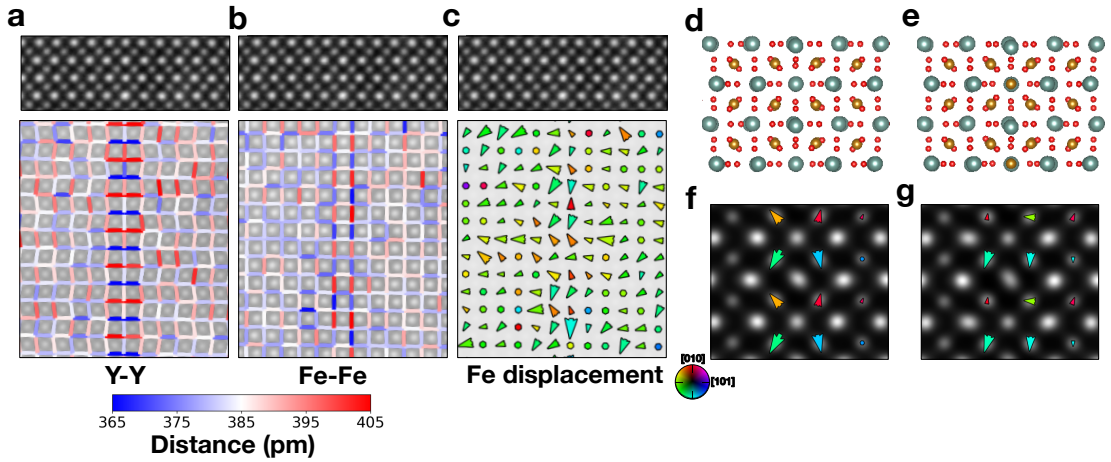

Figure 6-9: (a) Y-Y) and (b) Fe-Fe NLN distances from ADF STEM. (c) The net Fe displacement map was obtained from the atom column positions. (d, e) relaxed DFT structure of APB without and with a Fe_Y antisite respectively, (f, g) simulated ADF STEM image of APB relaxed DFT structure without and with a Fe_Y antisite, respectively. Used with permission of John Wiley & Sons - Books, from Ref. [3]; permission conveyed through Copyright Clearance Center, Inc. ©2021 Wiley-VCH GmbH

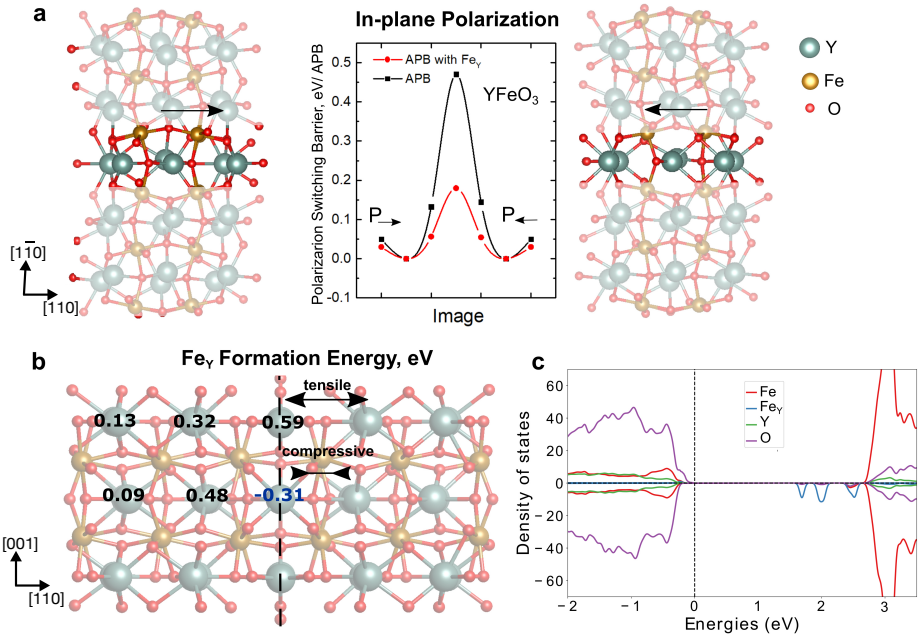

Figure 6-10: (a) The relative formation energies of Fe_Y defects (eV) at different Y positions across an APB. A Fe_Y in bulk YFO was used for the reference energy. (b) Projected density of states for Fe-rich APB of YFO where the Fermi level is set to zero. (c) DFT calculations demonstrating the bi-stable, polar nature of the (101) APB in YFO. Used with permission of John Wiley & Sons - Books, from Ref. [3]; permission conveyed through Copyright Clearance Center, Inc. ©2021 Wiley-VCH GmbH

Chapter 7

Conclusion and Future Work

7.1 Conclusion

In conclusion, my dissertation enables a quantitative method to determine the correlations among chemistry, structure, and properties in compositionally complex ferroelectrics, heterogeneous relaxors, and stoichiometry-controlled orthoferrites. First, the structural origin of relaxor behavior in Pb-based systems and their composition-dependent electromechanical coupling response is determined, which has been missing since their discovery (chapter 3). I utilize simultaneously acquired ADF and iDPC

STEM images to reveal the close connection between local chemistry and structure in relaxor ferroelectrics. Determining nanoscale polar structure from STEM images using cations and anions enables finding the spatial correlation of chemical and structural heterogeneities with low-angle domain walls. This suggests the presence of heterogeneities such as chemical, octahedral distortion, and octahedral tilt order create a polarization barrier, thus, stabilizing the nanoscale domain structure necessary for relaxor behavior. Such structural information about the origin of relaxor behavior will enable to induce relaxor behavior in new material systems by intentionally introducing heterogeneities to create polarization barriers across the material. This also allows developing materials growth and processing strategies to tune the existing relaxors to achieve higher electromechanical coupling/piezoelectric coefficients. This can be realized by balancing order (chemical and/or octahedral distortion/tilt) with the disorder, which is key to the composition-dependent electromechanical coupling response in relaxors. Further, relaxor ferroelectrics are desired in their thin film form to fulfill the extensive demand for the miniaturization of electronic devices. To achieve full control of properties in these thin films similar to bulk, two critical factors, thickness, and strain effects, need to be addressed (chapter 4 & 5). The polar structure shows variation across the film thickness, which is strongly influenced by the local chemical variation. These also show directional dependent evolution with increased polar ordering along the growth direction. A critical film thickness with stable relaxor behavior along growth direction is also determined. Thin films below 10 nm show no relaxor behavior along growth direction due to an increase in polar correlations along in-plane direction arising from a depolarization field. The strong effect of epitaxial strain on relaxor behavior is also explored, which shows a decrease in the coupling of polar displacement with local chemistry at higher strained films. An increase in polar ordering is also revealed with increasing strain. This explains the decreasing trend in the strength of relaxor response with strain which arises from an increased polar ordering. Chemical ordered regions also increase in size at higher strain while the overall amount remains constant. This indicates the variation in the distribution of local chemistry across the strained thin films while the overall com-

position remains the same. These results show thickness and strain effects on polar structure evolution, local chemistry, and relaxor properties in thin films. This enables to predict behavior of relaxor ferroelectric films desired in modern electronic devices at specific thickness and strain conditions. This also allows to develop the design principles to tune relaxor properties with extremely controlled growth conditions in thin films. For example, to achieve higher strength of relaxor at higher strain conditions, introduction of dopants, changing composition or controlled growth conditions to decrease polar correlations can be realized. Finally, the structural origin of unconventional ferroelectric behavior in stoichiometry-controlled orthoferrites and YFO thin films is determined. These YFO thin films show ferroelectric behavior in Y-rich YFO films while absent in Fe-rich films. Functional defects such as Y_{Fe} antisites and APBs with Fe_Y antisites are determined. The local structural changes due to Y_{Fe} antisites show the breaking of crystal inversion symmetry, thus stabilizing the ferroelectric order. APBs present in these films also shows strong structural relaxation. DFT predicts APBs with Fe_Y antisites to have bi-stable polar behavior. While these APBs can show ferroelectric behavior, their significantly lower density compared to Y_{Fe} antisites indicates the ferroelectric response in YFO predominantly arises from Y_{Fe} antisites. This enables to design of strategies based on functional defects such as antisites to induce ferroelectricity in other orthoferrite systems. As finding multiferroic behavior in a single material is rare, these orthoferrite films with defect-induced ferroelectricity can be used for multiferroic application.

7.2 Future work

As discussed in chapters 3, 4 & 5, STEM enables identifying chemical and structural heterogeneities across relaxor ferroelectrics. These show nanoscale domain structure due to heterogeneities that break the long-range polar order. This nanoscale domain structure has been proposed for slimmer hysteresis P-E loop and also temperature dependant dielectric response but missing information about changes in domain configuration under an electric field and across temperature variation. An in-situ mi-

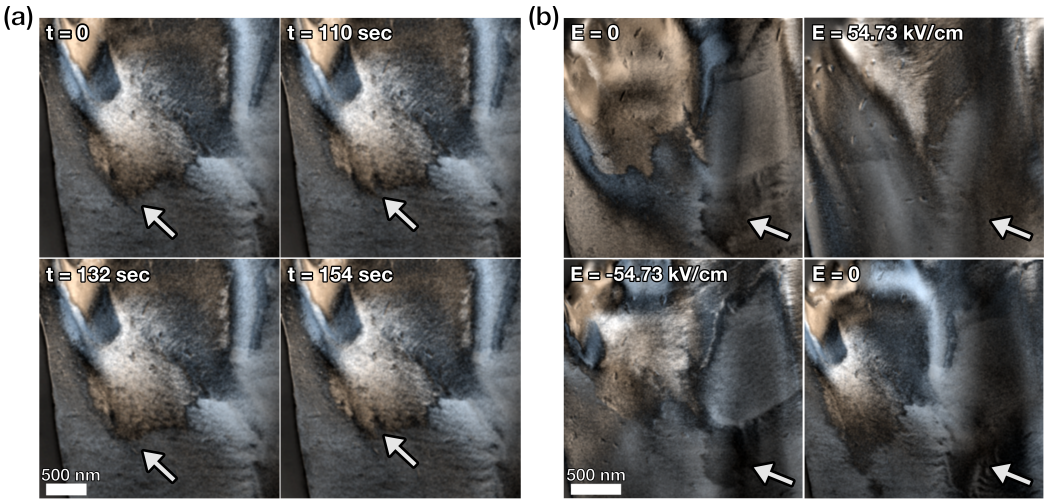

Figure 7-1: DPC images of PMN-PT (a) exposed to the electron beam without an applied electric field and (b) at the electric fields indicated. From ref. [113] and reprinted with permission from Cambridge University Press. ©Microscopy Society of America 2019

croscopy study of relaxors under biasing, heating, and cooling conditions will connect the nanoscale polar domain response to hysteresis and dielectric behavior.

Preliminary results show significant domain reorientation in PMN-PT relaxor ferroelectrics under an electric field, as shown in Figure 7-1 [113]. An electron beam was found to cause only the domain walls to flicker without any large-scale changes, as shown in Figure 7-1. The projected polarization mapped for the same unit cells at different applied fields reveals some polar nano regions try to align to the electric field but reside within a microscale ferroelectric domain that does not switch (Figure 7-2). This initial observation with in-situ STEM imaging raises several key questions about the mechanism for significant domain reorientations under an external electric field in relaxors. Simultaneous ADF and iDPC imaging along $\langle 1\bar{1}0 \rangle$ projection at different biasing conditions will enable a complete understanding of the role of inhomogeneities such as chemical, octahedral distortion, and tilt in determining the overall response of relaxor ferroelectrics.

Relaxors show a broad temperature-dependent dielectric response compared to a sharp peak in normal ferroelectrics. Phase transformations are usually associated with the sharp peak in the dielectric response from normal ferroelectrics. No phase

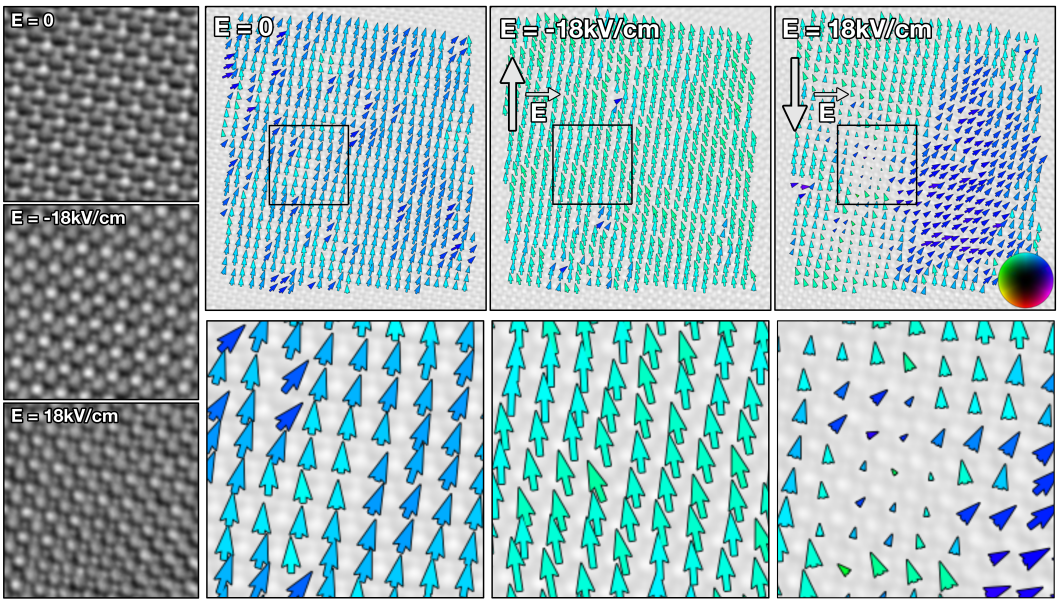

Figure 7-2: (left) iDPC images from the square regions marked in the polarization maps. Projected polarization is determined from the cation and anion positions for the indicated electric fields. From ref. [113] and reprinted with permission from Cambridge University Press. ©Microscopy Society of America 2019

change is found in relaxors around temperature at maximum dielectric permittivity. The nanoscale domains also froze at lower temperatures. Two different responses of domains have been proposed below freezing temperature. The polar slush model proposes an increased correlation of polar displacements instead of domain growth, as indicated by previous dark-field TEM observations. For relaxors, heating and cooling experiments inside an electron microscope will allow finding the domain response at varying temperatures. This will also enable the connection of the role of local chemical and structural variation with nanoscale domain behavior with temperature variation.

As Pb toxicity from electronic devices has been a major concern, extensive research is ongoing to obtain Pb-free relaxors with similar properties as of Pb contained materials. STEM enables finding the origin of nanoscale domains in Pb-based relaxors, allowing design experiments to control materials structure. A similar STEM study is necessary for Pb-free relaxors in bulk and thin film forms to determine all the chemical and structural inhomogeneities, allow to tune their properties significantly.

Bibliography

1. Kumar, A. *et al.* Atomic-resolution electron microscopy of nanoscale local structure in lead-based relaxor ferroelectrics. *Nature Materials* **20,** 62–67 (2021).
2. Ning, S. *et al.* An antisite defect mechanism for room temperature ferroelectricity in orthoferrites. *Nature Communications* **12,** 4298 (2021).
3. Kumar, A. *et al.* Antisite Defects Stabilized by Antiphase Boundaries in YFeO3 Thin Films. *Advanced Functional Materials* **32,** 1–7 (2022).
4. Scott, J. F. Applications of modern ferroelectrics. *Science* **315,** 954–959 (2007).
5. Ronald E. Cohen. Origin of ferroelectricity in perovskite oxides. *Nature* **358,** 136–138 (1992).
6. Cohen, R. E. Relaxors go critical. *Nature* **441,** 941–942 (2006).
7. Park, S.-E. & Shrout, T. R. Ultrahigh strain and piezoelectric behavior in relaxor based ferroelectric single crystals. *Journal of Applied Physics* **82,** 1804 (1997).
8. Zhang, S. & Li, F. High performance ferroelectric relaxor-$PbTiO_3$ single crystals: Status and perspective. *Journal of Applied Physics* **111,** 031301 (2012).
9. Zhang, S. *et al.* Advantages and challenges of relaxor-$PbTiO_3$ ferroelectric crystals for electroacoustic transducers - A review. *Prog Mater Sci.* **68,** 1–66 (2015).
10. Burns, G. & Dacol, F. H. Glassy polarization behavior in ferroelectric compounds $Pb(Mg_{1/3}Nb_{2/3})O_3$ and $Pb(Zn_{1/3}Nb_{2/3})O_3$. *Solid State Communications* **48,** 853–856 (1983).
11. Burns, G. & Dacol, F. H. Crystalline ferroelectrics with glassy polarization behavior. *Phys. Rev. B* **28,** 2527–2530 (1983).
12. Yang, L. *et al.* Relaxor ferroelectric behavior from strong physical pinning in a Poly(vinylidene fluoride-co-trifluoroethylene-co-chlorotrifluoroethylene) random terpolymer. *Macromolecules* **47,** 8119–8125 (2014).
13. Takenaka, H., Grinberg, I., Liu, S. & Rappe, A. M. Slush-like polar structures in single-crystal relaxors. *Nature* **546,** 391–395 (2017).
14. Li, F. *et al.* Giant piezoelectricity of Sm-doped $Pb(Mg_{1/3}Nb_{2/3})O_3$-$PbTiO_3$ single crystals. *Science* **364,** 264–268 (2019).
15. Krogstad, M. J. *et al.* The relation of local order to material properties in relaxor ferroelectrics. *Nature Materials* **17,** 718–724 (2018).

16. Singh, A. K., Pandey, D. & Zaharko, O. Powder neutron diffraction study of phase transitions in and a phase diagram of (1-x) $[Pb(Mg_{1/3}Nb_{2/3})O_3]$-$xPbTiO_3$. *Phys. Rev. B* **74,** 024101 (2006).

17. Singh, A. K. & Pandey, D. Evidence for M_B and M_C phases in the morphotropic phase boundary region of (1-x) $[Pb(Mg_{1/3}Nb_{2/3})O_3]$-$xPbTiO_3$: A Rietveld study. *Phys. Rev. B* **67,** 064102 (2003).

18. Thomas, N. W., Ivanov, S. A., Ananta, S., Tellgren, R. & Rundlof, H. New evidence for rhombohedral symmetry in the relaxor ferroelectric $Pb(Mg_{1/3}Nb_{2/3})O_3$. *Journal of the European Ceramic Society* **19,** 2667–2675 (1999).

19. Kim, K. H., Payne, D. A. & Zuo, J. M. Symmetry of piezoelectric (1-x) $[Pb(Mg_{1/3}Nb_{2/3})O_3]$-$xPbTiO_3$ (x=0.31) single crystal at different length scales in the morphotropic phase boundary region. *Phys. Rev. B* **86,** 184113 (2012).

20. Cowley, R. A., Gvasaliya, S. N., Lushnikov, S. G., Roessli, B. & Rotaru, G. M. Relaxing with relaxors: A review of relaxor ferroelectrics. *Advances in Physics* **60,** 229–327 (2011).

21. Davis, M. Picturing the elephant: Giant piezoelectric activity and the monoclinic phases of relaxor-ferroelectric single crystals. *Journal of Electroceramics* **19,** 25–47 (2007).

22. Randall, C. A. & Bhalla, A. S. Nanostructural-Property Relations in Complex Lead Perovskites. *Japanese Journal of Applied Physics* **29,** 327–333 (1990).

23. Randall, C. A., Bhalla, A. S., Shrout, T. R. & Cross, L. E. Classification and consequences of complex lead perovskite ferroelectrics with regard to B-site cation order. *Journal of Materials Research* **5,** 829–834 (1990).

24. Takesue, N. *et al.* Effects of B-site ordering/disordering in lead scandium niobate. *Journal of Physics: Condensed Matter* **11,** 8301–8312 (1999).

25. Goossens, D. J. Local ordering in lead-based relaxor ferroelectrics. *Acc. Chem. Res.* **46,** 2597–2606 (2013).

26. Cabral, M. J., Zhang, S., Dickey, E. C. & LeBeau, J. M. Gradient chemical order in the relaxor $Pb(Mg_{1/3}Nb_{2/3})O_3$. *Appl. Phys. Lett.* **112,** 082901 (2018).

27. Kopecký, M., Kub, J., Fábry, J. & Hlinka, J. Nanometer-range atomic order directly recovered from resonant diffuse scattering. *Phys. Rev. B* **93,** 054202 (2016).

28. Eremenko, M. *et al.* Local atomic order and hierarchical polar nanoregions in a classical relaxor ferroelectric. *Nat Commun* **10,** 2728 (2019).

29. Rosenfeld, H. D. & Egami, T. Short and intermediate range structural and chemical order in the relaxor ferroelectric lead magnesium niobate. *Ferroelectrics* **164,** 133–141 (1995).

30. Keen, D. A. & Goodwin, A. L. The crystallography of correlated disorder. *Nature* **521,** 303–309 (2015).

31. Xu, G., Wen, J., Stock, C. & Gehring, P. M. Phase instability induced by polar nanoregions in a relaxor ferroelectric system. *Nature Materials* **7,** 562–566 (2008).

32. Shang, M. *et al.* The multiferroic perovskite $YFeO_3$. *Applied Physics Letters* **102,** 062903 (2013).

33. Shang, M., Wang, C., Chen, Y., Sun, F. & Yuan, H. The multiferroic epitaxial thin film $YFeO_3$. *Materials Letters* **175,** 23–26 (2016).

34. Muñoz-García, A. B., Pavone, M. & Carter, E. A. Effect of antisite defects on the formation of oxygen vacancies in Sr_2FeMoO_6: Implications for ion and electron transport. *Chemistry of Materials* **23,** 4525–4536 (2011).

35. Lee, D. *et al.* Emergence of room-temperature ferroelectricity at reduced dimensions. *Science* **349,** 1314–1317 (2015).

36. Gao, R. *et al.* Ferroelectricity in $Pb_{1+\delta}ZrO_3$ Thin Films. *Chemistry of Materials* **29,** 6544–6551 (2017).

37. Van Aert, S. *et al.* Direct observation of ferrielectricity at ferroelastic domain boundaries in $CaTiO_3$ by electron microscopy. *Advanced Materials* **24,** 523–527 (2012).

38. Morikawa, D. & Tsuda, K. Local crystal symmetry and structure at $CaTiO_3$ twin boundaries Local crystal symmetry and structure at CaTiO3 twin boundaries. *Appl. Phys. Lett.* **118,** 092901 (2021).

39. McKenna, K. P. *et al.* Atomic-scale structure and properties of highly stable antiphase boundary defects in Fe_3O_4. *Nature Communications* **5,** 5740 (2014).

40. Alpay, S. P., Mantese, J., Trolier-Mckinstry, S., Zhang, Q. & Whatmore, R. W. Next-generation electrocaloric and pyroelectric materials for solid-state electrothermal energy interconversion. *MRS Bulletin* **39,** 1099–1109 (2014).

41. Kutnjak, Z., Petzelt, J. & Blinc, R. The giant electromechanical response in ferroelectric relaxors as a critical phenomenon. *Nature* **441,** 956–959 (2006).

42. Eric Cross, L. Relaxor ferroelecirics. *Ferroelectrics* **76,** 241–267 (1987).

43. Mandal, A. & Nigam, M. K. A Transition From Relaxor To Normal Ferroelectric: An Overview Band. *International Journal of Engineering Research & Technology* **1,** 46–54 (2018).

44. Pramanick, A. & Nayak, S. Perspective on emerging views on microscopic origin of relaxor behavior. *Journal of Materials Research* (2020).

45. Hilton, A. D., Barber, D. J., Randall, C. A. & Shrout, T. R. On short range ordering in the perovskite lead magnesium niobate. *Journal of Materials Science* **25,** 3461–3466 (1990).

46. Ahn, C. W. *et al.* A brief review on relaxor ferroelectrics and selected issues in lead-free relaxors. *Journal of the Korean Physical Society* **68,** 1481–1494 (2016).

47. Forsbergh, P. W. Domain structures and phase transitions in barium titanate. *Physical Review* **76,** 1187–1201 (1949).

48. Samara, G. A. Pressure and temperature dependence of the dielectric properties and phase transitions of the ferroelectric perovskites: Pbtio3 and batio3. *Ferroelectrics* **2,** 277–289 (1971).

49. Glinchuk, M. D. & Farhi, R. A random field theory based model for ferroelectric relaxors. *Journal of Physics Condensed Matter* **8,** 6985–6996 (1996).

50. Cross, L. E. Relaxor ferroelectrics: an overview. *Ferroelectrics* **151,** 305–320 (1994).

51. Jin, L., Li, F. & Zhang, S. Decoding the fingerprint of ferroelectric loops: Comprehension of the material properties and structures. *Journal of the American Ceramic Society* **97,** 1–27 (2014).

52. Al-Aaraji, M. N., Hasan, W. N. & Al-Marzoki, K. Progress in Lead Free- Relaxor Ferroelectrics for Energy Storage Applications. *Journal of Physics: Conference Series* **1973** (2021).

53. Burton, B. P., Cockayne, E. & Waghmare, U. V. Correlations between nanoscale chemical and polar order in relaxor ferroelectrics and the lengthscale for polar nanoregions. *Physical Review B,* 064113 (2005).

54. Welberry, T. R. One hundred years of diffuse x-ray scattering. *Metallurgical and Materials Transactions A: Physical Metallurgy and Materials Science* **45,** 75–84 (2014).

55. Kim, J. *et al.* Epitaxial Strain Control of Relaxor Ferroelectric Phase Evolution. *Adv. Mater.* **31,** 1901060 (2019).

56. Bosak, A., Chernyshov, D., Vakhrushev, S. & Krisch, M. Diffuse scattering in relaxor ferroelectrics: True three-dimensional mapping, experimental artefacts and modelling. *Acta Crystallographica Section A: Foundations of Crystallography* **68,** 117–123 (2012).

57. Burkovsky, R. G. *et al.* Structural heterogeneity and diffuse scattering in morphotropic lead zirconate-titanate single crystals. *Physical Review Letters* **109,** 1–4 (2012).

58. Smolensky, G. Ferroelectrics with diffuse phase transition. *Ferroelectrics* **53,** 129–135 (1984).

59. Pirc, R. & Blinc, R. Freezing dynamics of relaxor ferroelectrics and dipolar glasses. *Ferroelectrics* **379,** 30–34 (2009).

60. Viehland, D., Jang, S. J., Cross, L. E. & Wuttig, M. Freezing of the polarization fluctuations in lead magnesium niobate relaxors. *Journal of Applied Physics* **68,** 2916–2921 (1990).

61. Ben Ishai, P., De Oliveira, C. E., Ryabov, Y., Feldman, Y. & Agranat, A. J. Glass-forming liquid kinetics manifested in a KTN: Cu crystal. *Physical Review B - Condensed Matter and Materials Physics* **70,** 3–6 (2004).

62. Westphal, V., Kleemann, W. & Glinchuk, M. D. DifFuse Phase Transitions and Random-Field-Induced Domain States of the "Relaxor" Ferroelectric $PbMg_{1/3}Nb_{2/3}O_3$. *Physical Review Letters* **68,** 847–850 (1992).

63. Kleemann, W. Random Fields in Relaxor Ferroelectrics — a Jubilee Review. *Journal of Advanced Dielectrics* **02,** 1241001 (2012).

64. Ortega, N., Kumar, A., Scott, J. F. & Katiyar, R. S. Multifunctional magnetoelectric materials for device applications. *Journal of Physics Condensed Matter* **27** (2015).

65. Cheng, Y., Peng, B., Hu, Z., Zhou, Z. & Liu, M. Recent development and status of magnetoelectric materials and devices. *Physics Letters, Section A: General, Atomic and Solid State Physics* **382,** 3018–3025 (2018).

66. Fusil, S., Garcia, V., Barthélémy, A. & Bibes, M. Magnetoelectric devices for spintronics. *Annual Review of Materials Research* **44,** 91–116 (2014).

67. Cheong, S. W. & Mostovoy, M. Multiferroics: A magnetic twist for ferroelectricity. *Nature Materials* **6,** 13–20 (2007).

68. Hill, N. A. Why are there so few magnetic ferroelectrics? *Journal of Physical Chemistry B* **104,** 6694–6709 (2000).

69. Spaldin, N. A. & Ramesh, R. Advances in magnetoelectric multiferroics. *Nature Materials* **18,** 203–212 (2019).

70. Lee, J. H. & Rabe, K. M. Epitaxial strain induced multiferroicity in $SrMnO_3$ from first principles. *Physical Review Letters* **104,** 2–5 (2010).

71. Rushchanskii, K. Z. *et al.* A multiferroic material to search for the permanent electric dipole moment of the electron. *Nature Materials* **9,** 649–654 (2010).

72. Oh, Y. S., Luo, X., Huang, F. T., Wang, Y. & Cheong, S. W. Experimental demonstration of hybrid improper ferroelectricity and the presence of abundant charged walls in $(Ca,Sr)_3Ti_2O_7$ crystals. *Nature Materials* **14,** 407–413 (2015).

73. Qin, W., Xu, B. & Ren, S. An organic approach for nanostructured multiferroics. *Nanoscale* **7,** 9122–9132 (2015).

74. Sharma, P. *et al.* Structural and magnetocaloric properties of rare-earth orthoferrite perovskite: $TmFeO_3$. *Chemical Physics Letters* **740,** 137057 (2020).

75. Shang, M. *et al.* The multiferroic perovskite $YFeO_3$. *Applied Physics Letters* **102,** 2–5 (2013).

76. Acharya, S., Mondal, J., Ghosh, S., Roy, S. K. & Chakrabarti, P. K. Multiferroic behavior of lanthanum orthoferrite ($LaFeO_3$). *Materials Letters* **64,** 415–418 (2010).

77. Cabral, M. J. *Quantifying Short-Range Chemical and Structural Order in Complex Oxides via Scanning Transmission Electron Microscopy* PhD thesis (North Carolina State University, 2018).

78. David B. Williams, C. B. C. *Transmission Electron Microscopy-A Textbook for Materials Science* **6** (2009).

79. LeBeau, J. M., Findlay, S. D., Allen, L. J. & Stemmer, S. Quantitative atomic resolution scanning transmission electron microscopy. *Phys. Rev. Lett.* **100,** 206101 (2008).

80. Lazić, I., Bosch, E. G. & Lazar, S. Phase contrast STEM for thin samples: Integrated differential phase contrast. *Ultramicroscopy* **160,** 265–280 (2016).

81. Yücelen, E., Lazić, I. & Bosch, E. G. Phase contrast scanning transmission electron microscopy imaging of light and heavy atoms at the limit of contrast and resolution. *Scientific Reports* **8,** 1–10 (2018).

82. Shibata, N. *et al.* Differential phase-contrast microscopy at atomic resolution. *Nature Physics* **8,** 611–615 (2012).

83. De Graaf, S., Momand, J., Mitterbauer, C., Lazar, S. & Kooi, B. J. Resolving hydrogen atoms at metal-metal hydride interfaces. *Science Advances* **6,** eaay4312 (2020).

84. Sang, X. & LeBeau, J. M. Revolving scanning transmission electron microscopy: Correcting sample drift distortion without prior knowledge. *Ultramicroscopy* **138,** 28–35 (2014).

85. Sang, X., Oni, A. A. & Le Beau, J. M. Atom column indexing: Atomic resolution image analysis through a matrix representation. *Microsc. Microanal.* **20,** 1764–1771 (2014).

86. Salmon, J., Harmany, Z., Deledalle, C. A. & Willett, R. Poisson noise reduction with non-local PCA. *Journal of Mathematical Imaging and Vision* **48,** 279–294 (2014).

87. Yankovich, A. B. *et al.* Non-rigid registration and non-local principle component analysis to improve electron microscopy spectrum images. *Nanotechnology* **27** (2016).

88. Kirkland, E. J. *Advanced Computing in electron microscopy* **6,** 243–260 (2010).

89. Sato, Y. *et al.* 3D Multi-Scale Line Filter for Segmentation and Visualization of Curvilinear Structures in Medical Images. *Medical Image Analysis* **2,** 143–168 (1998).

90. Kreisel, J. *et al.* High-pressure x-ray scattering of oxides with a nanoscale local structure: Application to $Na_{1/2}Bi_{1/2}TiO_3$. *Phys. Rev. B* **68,** 014113 (2003).

91. Glazer, A. M. The classification of tilted octahedra in perovskites. *Acta Cryst.* **B28,** 3384–3392 (1972).

92. Sang, X., Grimley, E. D., Niu, C., Irving, D. L. & Lebeau, J. M. Direct observation of charge mediated lattice distortions in complex oxide solid solutions. *Appl. Phys. Lett.* **106,** 061913 (2015).

93. Kvyatkovskii, O. E. Oxygen Position in $Pb(Mg_{1/3}Nb_{2/3})O_3$ from ab initio Cluster Calculations. *Ferroelectrics* **299,** 55–57 (2004).

94. Sepliarsky, M. & Cohen, R. E. First-principles based atomistic modeling of phase stability in PMNxPT. *J. Phys.: Condens. Matter* **23,** 435902 (2011).

95. Fu, D. *et al.* Relaxor $Pb(Mg_{1/3}Nb_{2/3})O_3$: A Ferroelectric with Multiple Inhomogeneities. *Phys. Rev. Lett.* **103,** 207601 (2009).

96. Guo, Y. *et al.* The phase transition sequence and the location of the morphotropic phase boundary region in (1-x)[$Pb(Mg_{1/3}Nb_{2/3})O_3$]-x$PbTiO_3$ single crystal. *Journal of Physics Condensed Matter* **15** (2003).

97. Lin, K. *et al.* Chemical pressure in functional materials. *Chemical Society Reviews* **51,** 5351–5364 (2022).

98. Kumar, S. *et al.* Effect of lattice strain on structural and magnetic properties of Ca substituted barium hexaferrite. *Journal of Magnetism and Magnetic Materials* **458,** 30–38 (2018).

99. Hong, S. J. & Virkar, A. V. Lattice Parameters and Densities of Rare-Earth Oxide Doped Ceria Electrolytes. *Journal of the American Ceramic Society* **78,** 433–439 (1995).

100. SHANNON, R. D. Revised Effective Ionic Radii and Systematic Studies of Interatomie Distances in Halides and Chaleogenides. *Acta Cryst.* **32,** 751 (1976).

101. Lee, Y. *et al.* Flexible Ferroelectric Sensors with Ultrahigh Pressure Sensitivity and Linear Response over Exceptionally Broad Pressure Range. *ACS Nano* **12,** 4045–4054 (2018).

102. Song, D. *et al.* Observation of oxygen pyramid tilting induced polarization rotation in strained BiFeO3 thin film. *Journal of the American Ceramic Society* **103,** 2828–2834 (2020).

103. Shaw, T. M. and Trolier-McKinstry, S. and McIntyre, P. C. THE PROPERTIES OF FERROELECTRIC FILMS AT SMALL DIMENSIONS. *Annu. Rev. Mater. Sci* **30,** 263–298 (2000).

104. Kim, J. *Structure-Property Relationships in Relaxor Ferroelectric Thin Films* PhD thesis (2021), 1–120.

105. Fong, D. D. *et al.* Ferroelectricity in ultrathin perovskite films. *Science* **304,** 1650–1653 (2004).

106. Breckenfeld, E., Shah, A. B. & Martin, L. W. Strain evolution in non-stoichiometric heteroepitaxial thin-film perovskites. *Journal of Materials Chemistry C* **1,** 8052–8059 (2013).

107. LeBeau, J. M., Findlay, S. D., Allen, L. J. & Stemmer, S. Position averaged convergent beam electron diffraction: Theory and applications. English. *Ultramicroscopy* **110,** 118–125 (2010).

108. Wang, Z. *et al.* Designing antiphase boundaries by atomic control of heterointerfaces. *Proceedings of the National Academy of Sciences of the United States of America* **115,** 9485–9490 (2018).

109. Scola, J. *et al.* Microstructure and self-exchange coupling in a $YFeO_3$ film. *Journal of Applied Physics* **110,** 043928 (2011).

110. Farokhipoor, S. *et al.* Artificial chemical and magnetic structure at the domain walls of an epitaxial oxide. *Nature* **515,** 379–383 (2014).

111. Hirel, P., Marton, P., Mrovec, M. & Elsässer, C. Theoretical investigation of {110} generalized stacking faults and their relation to dislocation behavior in perovskite oxides. *Acta materialia* **58,** 6072–6079 (2010).

112. Wei, X. K. *et al.* Ferroelectric translational antiphase boundaries in nonpolar materials. *Nature Communications* **5,** 3031 (2014).

113. Kumar, A., Dhall, R. & LeBeau, J. M. In Situ Ferroelectric Domain Dynamics Probed with Differential Phase Contrast Imaging. *Microscopy and Microanalysis* **25,** 1838–1839 (2019).

CCC Marketplace™

This is a License Agreement between Abinash Kumar, Massachusetts Institute of Technology ("User") and Copyright Clearance Center, Inc. ("CCC") on behalf of the Rightsholder identified in the order details below. The license consists of the order details, the Marketplace Order General Terms and Conditions below, and any Rightsholder Terms and Conditions which are included below.

All payments must be made in full to CCC in accordance with the Marketplace Order General Terms and Conditions below.

Order Date	25-Jul-2022	**Type of Use**	Republish in a thesis/dissertation
Order License ID	1250888-1		
ISSN	1521-4095	**Publisher**	Wiley-VCH
		Portion	Chart/graph/table/figure

LICENSED CONTENT

Publication Title	Advanced materials	**Publication Type**	e-Journal
Article Title	Epitaxial Strain Control of Relaxor Ferroelectric Phase Evolution.	**Start Page**	1901060
		Issue	21
		Volume	31
Date	01/01/1998	**URL**	http://deposit.ddb.de/cgi-bin/dokserv?idn=971150583
Language	German		
Country	Germany		
Rightsholder	John Wiley & Sons - Books		

REQUEST DETAILS

Portion Type	Chart/graph/table/figure	**Distribution**	Worldwide
Number of charts / graphs / tables / figures requested	2	**Translation**	Original language of publication
		Copies for the disabled?	No
Format (select all that apply)	Print, Electronic	**Minor editing privileges?**	Yes
Who will republish the content?	Academic institution	**Incidental promotional use?**	No
Duration of Use	Life of current edition	**Currency**	USD
Lifetime Unit Quantity	More than 2,000,000		
Rights Requested	Main product		

NEW WORK DETAILS

Title	Structure-property correlations in compositionally complex ferroelectrics	**Institution name**	Massachusetts Institute of Technology
		Expected presentation date	2022-07-31
Instructor name	Abinash Kumar		

ADDITIONAL DETAILS

The requesting person / organization to appear on the license	Abinash Kumar, Massachusetts Institute of Technology

REUSE CONTENT DETAILS

Title, description or numeric reference of the portion(s)	Figure 1& 2	**Title of the article/chapter the portion is from**	Epitaxial Strain Control of Relaxor Ferroelectric Phase Evolution.
Editor of portion(s)	Chung, Linh; Damodaran, Anoop R.; Fernandez, Abel; Gao, Ran; Kim, Jieun; Martin, Lane W.; McCarter, Margaret R.; Qi, Yubo; Rappe, Andrew M.; Saremi, Sahar; Takenaka, Hiroyuki	**Author of portion(s)**	Chung, Linh; Damodaran, Anoop R.; Fernandez, Abel; Gao, Ran; Kim, Jieun; Martin, Lane W.; McCarter, Margaret R.; Qi, Yubo; Rappe, Andrew M.; Saremi, Sahar; Takenaka, Hiroyuki
Volume of serial or monograph	31	**Publication date of portion**	2019-05-01
Page or page range of portion	1901060		

RIGHTSHOLDER TERMS AND CONDITIONS

No right, license or interest to any trademark, trade name, service mark or other branding ("Marks") of WILEY or its licensors is granted hereunder, and you agree that you shall not assert any such right, license or interest with respect thereto. You may not alter, remove or suppress in any manner any copyright, trademark or other notices displayed by the Wiley material. This Agreement will be void if the Type of Use, Format, Circulation, or Requestor Type was misrepresented during the licensing process. In no instance may the total amount of Wiley Materials used in any Main Product, Compilation or Collective work comprise more than 5% (if figures/tables) or 15% (if full articles/chapters) of the (entirety of the) Main Product, Compilation or Collective Work. Some titles may be available under an Open Access license. It is the Licensors' responsibility to identify the type of Open Access license on which the requested material was published, and comply fully with the terms of that license for the type of use specified Further details can be found on Wiley Online Library http://olabout.wiley.com/WileyCDA/Section/id-410895.html.

Marketplace Order General Terms and Conditions

The following terms and conditions (“General Terms”), together with any applicable Publisher Terms and Conditions, govern User’s use of Works pursuant to the Licenses granted by Copyright Clearance Center, Inc. (“CCC”) on behalf of the applicable Rightsholders of such Works through CCC’s applicable Marketplace transactional licensing services (each, a “Service”).

1) **Definitions.** For purposes of these General Terms, the following definitions apply:

"License" is the licensed use the User obtains via the Marketplace platform in a particular licensing transaction, as set forth in the Order Confirmation.

"Order Confirmation" is the confirmation CCC provides to the User at the conclusion of each Marketplace transaction. "Order Confirmation Terms" are additional terms set forth on specific Order Confirmations not set forth in the General Terms that can include terms applicable to a particular CCC transactional licensing service and/or any Rightsholder-specific terms.

"Rightsholder(s)" are the holders of copyright rights in the Works for which a User obtains licenses via the Marketplace platform, which are displayed on specific Order Confirmations.

"Terms" means the terms and conditions set forth in these General Terms and any additional Order Confirmation Terms collectively.

"User" or "you" is the person or entity making the use granted under the relevant License. Where the person accepting the Terms on behalf of a User is a freelancer or other third party who the User authorized to accept the General Terms on the User's behalf, such person shall be deemed jointly a User for purposes of such Terms.

"Work(s)" are the copyright protected works described in relevant Order Confirmations.

2) **Description of Service.** CCC's Marketplace enables Users to obtain Licenses to use one or more Works in accordance with all relevant Terms. CCC grants Licenses as an agent on behalf of the copyright rightsholder identified in the relevant Order Confirmation.

3) **Applicability of Terms.** The Terms govern User's use of Works in connection with the relevant License. In the event of any conflict between General Terms and Order Confirmation Terms, the latter shall govern. User acknowledges that Rightsholders have complete discretion whether to grant any permission, and whether to place any limitations on any grant, and that CCC has no right to supersede or to modify any such discretionary act by a Rightsholder.

4) **Representations; Acceptance.** By using the Service, User represents and warrants that User has been duly authorized by the User to accept, and hereby does accept, all Terms.

5) **Scope of License; Limitations and Obligations.** All Works and all rights therein, including copyright rights, remain the sole and exclusive property of the Rightsholder. The License provides only those rights expressly set forth in the terms and conveys no other rights in any Works

6) **General Payment Terms.** User may pay at time of checkout by credit card or choose to be invoiced. If the User chooses to be invoiced, the User shall: (i) remit payments in the manner identified on specific invoices, (ii) unless otherwise specifically stated in an Order Confirmation or separate written agreement, Users shall remit payments upon receipt of the relevant invoice from CCC, either by delivery or notification of availability of the invoice via the Marketplace platform, and (iii) if the User does not pay the invoice within 30 days of receipt, the User may incur a service charge of 1.5% per month or the maximum rate allowed by applicable law, whichever is less. While User may exercise the rights in the License immediately upon receiving the Order Confirmation, the License is automatically revoked and is null and void, as if it had never been issued, if CCC does not receive complete payment on a timely basis.

7) **General Limits on Use.** Unless otherwise provided in the Order Confirmation, any grant of rights to User (i) involves only the rights set forth in the Terms and does not include subsequent or additional uses, (ii) is non-exclusive and non-transferable, and (iii) is subject to any and all limitations and restrictions (such as, but not limited to, limitations on duration of use or circulation) included in the Terms. Upon completion of the licensed use as set forth in the Order Confirmation, User shall either secure a new permission for further use of the Work(s) or immediately cease any new use of the Work(s) and shall render inaccessible (such as by deleting or by removing or severing links or other locators) any further copies of the Work. User may only make alterations to the Work if and as expressly set forth in the Order Confirmation. No Work may be used in any way that is defamatory, violates the rights of third parties (including such third

parties' rights of copyright, privacy, publicity, or other tangible or intangible property), or is otherwise illegal, sexually explicit, or obscene. In addition, User may not conjoin a Work with any other material that may result in damage to the reputation of the Rightsholder. User agrees to inform CCC if it becomes aware of any infringement of any rights in a Work and to cooperate with any reasonable request of CCC or the Rightsholder in connection therewith.

8) **Third Party Materials.** In the event that the material for which a License is sought includes third party materials (such as photographs, illustrations, graphs, inserts and similar materials) that are identified in such material as having been used by permission (or a similar indicator), User is responsible for identifying, and seeking separate licenses (under this Service, if available, or otherwise) for any of such third party materials; without a separate license, User may not use such third party materials via the License.

9) **Copyright Notice.** Use of proper copyright notice for a Work is required as a condition of any License granted under the Service. Unless otherwise provided in the Order Confirmation, a proper copyright notice will read substantially as follows: "Used with permission of [Rightsholder's name], from [Work's title, author, volume, edition number and year of copyright]; permission conveyed through Copyright Clearance Center, Inc." Such notice must be provided in a reasonably legible font size and must be placed either on a cover page or in another location that any person, upon gaining access to the material which is the subject of a permission, shall see, or in the case of republication Licenses, immediately adjacent to the Work as used (for example, as part of a by-line or footnote) or in the place where substantially all other credits or notices for the new work containing the republished Work are located. Failure to include the required notice results in loss to the Rightsholder and CCC, and the User shall be liable to pay liquidated damages for each such failure equal to twice the use fee specified in the Order Confirmation, in addition to the use fee itself and any other fees and charges specified.

10) **Indemnity.** User hereby indemnifies and agrees to defend the Rightsholder and CCC, and their respective employees and directors, against all claims, liability, damages, costs, and expenses, including legal fees and expenses, arising out of any use of a Work beyond the scope of the rights granted herein and in the Order Confirmation, or any use of a Work which has been altered in any unauthorized way by User, including claims of defamation or infringement of rights of copyright, publicity, privacy, or other tangible or intangible property.

11) **Limitation of Liability.** UNDER NO CIRCUMSTANCES WILL CCC OR THE RIGHTSHOLDER BE LIABLE FOR ANY DIRECT, INDIRECT, CONSEQUENTIAL, OR INCIDENTAL DAMAGES (INCLUDING WITHOUT LIMITATION DAMAGES FOR LOSS OF BUSINESS PROFITS OR INFORMATION, OR FOR BUSINESS INTERRUPTION) ARISING OUT OF THE USE OR INABILITY TO USE A WORK, EVEN IF ONE OR BOTH OF THEM HAS BEEN ADVISED OF THE POSSIBILITY OF SUCH DAMAGES. In any event, the total liability of the Rightsholder and CCC (including their respective employees and directors) shall not exceed the total amount actually paid by User for the relevant License. User assumes full liability for the actions and omissions of its principals, employees, agents, affiliates, successors, and assigns.

12) **Limited Warranties.** THE WORK(S) AND RIGHT(S) ARE PROVIDED "AS IS." CCC HAS THE RIGHT TO GRANT TO USER THE RIGHTS GRANTED IN THE ORDER CONFIRMATION DOCUMENT. CCC AND THE RIGHTSHOLDER DISCLAIM ALL OTHER WARRANTIES RELATING TO THE WORK(S) AND RIGHT(S), EITHER EXPRESS OR IMPLIED, INCLUDING WITHOUT LIMITATION IMPLIED WARRANTIES OF MERCHANTABILITY OR FITNESS FOR A PARTICULAR PURPOSE. ADDITIONAL RIGHTS MAY BE REQUIRED TO USE ILLUSTRATIONS, GRAPHS, PHOTOGRAPHS, ABSTRACTS, INSERTS, OR OTHER PORTIONS OF THE WORK (AS OPPOSED TO THE ENTIRE WORK) IN A MANNER CONTEMPLATED BY USER; USER UNDERSTANDS AND AGREES THAT NEITHER CCC NOR THE RIGHTSHOLDER MAY HAVE SUCH ADDITIONAL RIGHTS TO GRANT.

13) **Effect of Breach.** Any failure by User to pay any amount when due, or any use by User of a Work beyond the scope of the License set forth in the Order Confirmation and/or the Terms, shall be a material breach of such License. Any breach not cured within 10 days of written notice thereof shall result in immediate termination of such License without further notice. Any unauthorized (but licensable) use of a Work that is terminated immediately upon notice thereof may be liquidated by payment of the Rightsholder's ordinary license price therefor; any unauthorized (and unlicensable) use that is not terminated immediately for any reason (including, for example, because materials containing the Work cannot reasonably be recalled) will be subject to all remedies available at law or in equity, but in no event to a payment of less than three times the Rightsholder's ordinary license price for the most closely analogous licensable use plus Rightsholder's and/or CCC's costs and expenses incurred in collecting such payment.

14) **Additional Terms for Specific Products and Services.** If a User is making one of the uses described in this Section 14, the additional terms and conditions apply:

a) ***Print Uses of Academic Course Content and Materials (photocopies for academic coursepacks or classroom handouts).*** For photocopies for academic coursepacks or classroom handouts the following additional terms apply:

i) The copies and anthologies created under this License may be made and assembled by faculty members individually or at their request by on-campus bookstores or copy centers, or by off-campus copy shops and other similar entities.

ii) No License granted shall in any way: (i) include any right by User to create a substantively non-identical copy of the Work or to edit or in any other way modify the Work (except by means of deleting material immediately preceding or following the entire portion of the Work copied) (ii) permit "publishing ventures" where any particular anthology would be systematically marketed at multiple institutions.

iii) Subject to any Publisher Terms (and notwithstanding any apparent contradiction in the Order Confirmation arising from data provided by User), any use authorized under the academic pay-per-use service is limited as follows:

A) any License granted shall apply to only one class (bearing a unique identifier as assigned by the institution, and thereby including all sections or other subparts of the class) at one institution;

B) use is limited to not more than 25% of the text of a book or of the items in a published collection of essays, poems or articles;

C) use is limited to no more than the greater of (a) 25% of the text of an issue of a journal or other periodical or (b) two articles from such an issue;

D) no User may sell or distribute any particular anthology, whether photocopied or electronic, at more than one institution of learning;

E) in the case of a photocopy permission, no materials may be entered into electronic memory by User except in order to produce an identical copy of a Work before or during the academic term (or analogous period) as to which any particular permission is granted. In the event that User shall choose to retain materials that are the subject of a photocopy permission in electronic memory for purposes of producing identical copies more than one day after such retention (but still within the scope of any permission granted), User must notify CCC of such fact in the applicable permission request and such retention shall constitute one copy actually sold for purposes of calculating permission fees due; and

F) any permission granted shall expire at the end of the class. No permission granted shall in any way include any right by User to create a substantively non-identical copy of the Work or to edit or in any other way modify the Work (except by means of deleting material immediately preceding or following the entire portion of the Work copied).

iv) Books and Records; Right to Audit. As to each permission granted under the academic pay-per-use Service, User shall maintain for at least four full calendar years books and records sufficient for CCC to determine the numbers of copies made by User under such permission. CCC and any representatives it may designate shall have the right to audit such books and records at any time during User's ordinary business hours, upon two days' prior notice. If any such audit shall determine that User shall have underpaid for, or underreported, any photocopies sold or by three percent (3%) or more, then User shall bear all the costs of any such audit; otherwise, CCC shall bear the costs of any such audit. Any amount determined by such audit to have been underpaid by User shall immediately be paid to CCC by User, together with interest thereon at the rate of 10% per annum from the date such amount was originally due. The provisions of this paragraph shall survive the termination of this License for any reason.

b) ***Digital Pay-Per-Uses of Academic Course Content and Materials (e-coursepacks, electronic reserves, learning management systems, academic institution intranets).*** For uses in e-coursepacks, posts in electronic reserves, posts in learning management systems, or posts on academic institution intranets, the following additional terms apply:

i) The pay-per-uses subject to this Section 14(b) include:

A) **Posting e-reserves, course management systems, e-coursepacks for text-based content,** which grants authorizations to import requested material in electronic format, and allows electronic access to this material to members of a designated college or university class, under the direction of an instructor designated by the college or university, accessible only under appropriate electronic controls (e.g., password);

B) **Posting e-reserves, course management systems, e-coursepacks for material consisting of photographs or other still images not embedded in text,** which grants not only the authorizations described in Section 14(b)(i)(A) above, but also the following authorization: to include the requested material in course materials for use consistent with Section 14(b)(i)(A) above, including any necessary resizing, reformatting or modification of the resolution of such requested material (provided that such modification does not alter the underlying editorial content or meaning of the requested material, and provided that the resulting modified content is used solely within the scope of, and in a manner consistent with, the particular authorization described in the Order Confirmation and the Terms), but not including any other form of manipulation, alteration or editing of the requested material;

C) **Posting e-reserves, course management systems, e-coursepacks or other academic distribution for audiovisual content,** which grants not only the authorizations described in Section 14(b)(i)(A) above, but also the following authorizations: (i) to include the requested material in course materials for use consistent with Section 14(b)(i)(A) above; (ii) to display and perform the requested material to such members of such class in the physical classroom or remotely by means of streaming media or other video formats; and (iii) to "clip" or reformat the requested material for purposes of time or content management or ease of delivery, provided that such “clipping” or reformatting does not alter the underlying editorial content or meaning of the requested material and that the resulting material is used solely within the scope of, and in a manner consistent with, the particular authorization described in the Order Confirmation and the Terms. Unless expressly set forth in the relevant Order Conformation, the License does not authorize any other form of manipulation, alteration or editing of the requested material.

ii) Unless expressly set forth in the relevant Order Confirmation, no License granted shall in any way: (i) include any right by User to create a substantively non-identical copy of the Work or to edit or in any other way modify the Work (except by means of deleting material immediately preceding or following the entire portion of the Work copied or, in the case of Works subject to Sections 14(b)(1)(B) or (C) above, as described in such Sections) (ii) permit "publishing ventures" where any particular course materials would be systematically marketed at multiple institutions.

iii) Subject to any further limitations determined in the Rightsholder Terms (and notwithstanding any apparent contradiction in the Order Confirmation arising from data provided by User), any use authorized under the electronic course content pay-per-use service is limited as follows:

A) any License granted shall apply to only one class (bearing a unique identifier as assigned by the institution, and thereby including all sections or other subparts of the class) at one institution;

B) use is limited to not more than 25% of the text of a book or of the items in a published collection of essays, poems or articles;

C) use is limited to not more than the greater of (a) 25% of the text of an issue of a journal or other periodical or (b) two articles from such an issue;

D) no User may sell or distribute any particular materials, whether photocopied or electronic, at more than one institution of learning;

E) electronic access to material which is the subject of an electronic-use permission must be limited by means of electronic password, student identification or other control permitting access solely to students and instructors in the class;

F) User must ensure (through use of an electronic cover page or other appropriate means) that any person, upon gaining electronic access to the material, which is the subject of a permission, shall see:

- a proper copyright notice, identifying the Rightsholder in whose name CCC has granted permission,
- a statement to the effect that such copy was made pursuant to permission,
- a statement identifying the class to which the material applies and notifying the reader that the material has been made available electronically solely for use in the class, and
- a statement to the effect that the material may not be further distributed to any person outside the class, whether by copying or by transmission and whether electronically or in paper form, and User must also ensure that such cover page or other means will print out in the event that the person accessing the material chooses to print out the material or any part thereof.

G) any permission granted shall expire at the end of the class and, absent some other form of authorization, User is thereupon required to delete the applicable material from any electronic storage or to block electronic access to the applicable material.

iv) Uses of separate portions of a Work, even if they are to be included in the same course material or the same university or college class, require separate permissions under the electronic course content pay-per-use Service. Unless otherwise provided in the Order Confirmation, any grant of rights to User is limited to use completed no later than the end of the academic term (or analogous period) as to which any particular permission is granted.

v) Books and Records; Right to Audit. As to each permission granted under the electronic course content Service, User shall maintain for at least four full calendar years books and records sufficient for CCC to determine the numbers of copies made by User under such permission. CCC and any representatives it may designate shall have the right to audit such books and records at any time during User's ordinary business hours, upon two days' prior notice. If any such audit shall determine that User shall have underpaid for, or underreported, any electronic copies used by three percent (3%) or more, then User shall bear all the costs of any such audit; otherwise, CCC shall bear the costs of any such audit. Any amount determined by such audit to have been underpaid by User shall immediately be paid to CCC by User, together with interest thereon at the rate of 10% per annum from the date such amount was originally due. The provisions of this paragraph shall survive the termination of this license for any reason.

c) ***Pay-Per-Use Permissions for Certain Reproductions (Academic photocopies for library reserves and interlibrary loan reporting) (Non-academic internal/external business uses and commercial document delivery).*** The License expressly excludes the uses listed in Section (c)(i)-(v) below (which must be subject to separate license from the applicable Rightsholder) for: academic photocopies for library reserves and interlibrary loan reporting; and non-academic internal/external business uses and commercial document delivery.

i) electronic storage of any reproduction (whether in plain-text, PDF, or any other format) other than on a transitory basis;

ii) the input of Works or reproductions thereof into any computerized database;

iii) reproduction of an entire Work (cover-to-cover copying) except where the Work is a single article;

iv) reproduction for resale to anyone other than a specific customer of User;

v) republication in any different form. Please obtain authorizations for these uses through other CCC services or

directly from the rightsholder.

Any license granted is further limited as set forth in any restrictions included in the Order Confirmation and/or in these Terms.

d) ***Electronic Reproductions in Online Environments (Non-Academic-email, intranet, internet and extranet).*** For "electronic reproductions", which generally includes e-mail use (including instant messaging or other electronic transmission to a defined group of recipients) or posting on an intranet, extranet or Intranet site (including any display or performance incidental thereto), the following additional terms apply:

i) Unless otherwise set forth in the Order Confirmation, the License is limited to use completed within 30 days for any use on the Internet, 60 days for any use on an intranet or extranet and one year for any other use, all as measured from the "republication date" as identified in the Order Confirmation, if any, and otherwise from the date of the Order Confirmation.

ii) User may not make or permit any alterations to the Work, unless expressly set forth in the Order Confirmation (after request by User and approval by Rightsholder); provided, however, that a Work consisting of photographs or other still images not embedded in text may, if necessary, be resized, reformatted or have its resolution modified without additional express permission, and a Work consisting of audiovisual content may, if necessary, be "clipped" or reformatted for purposes of time or content management or ease of delivery (provided that any such resizing, reformatting, resolution modification or “clipping” does not alter the underlying editorial content or meaning of the Work used, and that the resulting material is used solely within the scope of, and in a manner consistent with, the particular License described in the Order Confirmation and the Terms.

15) **Miscellaneous.**

a) User acknowledges that CCC may, from time to time, make changes or additions to the Service or to the Terms, and that Rightsholder may make changes or additions to the Rightsholder Terms. Such updated Terms will replace the prior terms and conditions in the order workflow and shall be effective as to any subsequent Licenses but shall not apply to Licenses already granted and paid for under a prior set of terms.

b) Use of User-related information collected through the Service is governed by CCC's privacy policy, available online at www.copyright.com/about/privacy-policy/.

c) The License is personal to User. Therefore, User may not assign or transfer to any other person (whether a natural person or an organization of any kind) the License or any rights granted thereunder; provided, however, that, where applicable, User may assign such License in its entirety on written notice to CCC in the event of a transfer of all or substantially all of User's rights in any new material which includes the Work(s) licensed under this Service.

d) No amendment or waiver of any Terms is binding unless set forth in writing and signed by the appropriate parties, including, where applicable, the Rightsholder. The Rightsholder and CCC hereby object to any terms contained in any writing prepared by or on behalf of the User or its principals, employees, agents or affiliates and purporting to govern or otherwise relate to the License described in the Order Confirmation, which terms are in any way inconsistent with any Terms set forth in the Order Confirmation, and/or in CCC's standard operating procedures, whether such writing is prepared prior to, simultaneously with or subsequent to the Order Confirmation, and whether such writing appears on a copy of the Order Confirmation or in a separate instrument.

e) The License described in the Order Confirmation shall be governed by and construed under the law of the State of New York, USA, without regard to the principles thereof of conflicts of law. Any case, controversy, suit, action, or proceeding arising out of, in connection with, or related to such License shall be brought, at CCC's sole discretion, in any federal or state court located in the County of New York, State of New York, USA, or in any federal or state court whose geographical jurisdiction covers the location of the Rightsholder set forth in the Order Confirmation. The parties expressly submit to the personal jurisdiction and venue of each such federal or state court.

CCC Marketplace™

Order Date	30-May-2022	**Type of Use**	Republish in a thesis/dissertation
Order License ID	1226935-1		
ISSN	1616-3028	**Publisher**	WILEY - V C H VERLAG GMBH & CO. KGAA
		Portion	Chapter/article

LICENSED CONTENT

Publication Title	Advanced functional materials	**Publication Type**	e-Journal
		Start Page	n/a
Article Title	Antisite Defects Stabilized by Antiphase Boundaries in YFeO3 Thin Films	**End Page**	n/a
		Issue	9
Date	01/01/2001	**Volume**	32
Language	English	**URL**	http://www3.interscience.wiley.com/cgi-bin/jhome/77003362
Country	Germany		
Rightsholder	John Wiley & Sons - Books		

REQUEST DETAILS

Portion Type	Chapter/article	**Rights Requested**	Main product and any product related to main product
Page range(s)	1-7		
Total number of pages	7	**Distribution**	Worldwide
Format (select all that apply)	Print, Electronic	**Translation**	Original language of publication
Who will republish the content?	Author of requested content	**Copies for the disabled?**	Yes
		Minor editing privileges?	Yes
Duration of Use	Life of current and all future editions	**Incidental promotional use?**	No
Lifetime Unit Quantity	More than 2,000,000	**Currency**	USD

NEW WORK DETAILS

Title	Structure-property correlations in compositionally complex ferroelectrics	**Institution name**	Massachusetts Institute of Technology
		Expected presentation date	2022-07-07
Instructor name	Abinash Kumar		

ADDITIONAL DETAILS

The requesting person / organization to appear on the license	Abinash Kumar

REUSE CONTENT DETAILS

Title, description or numeric reference of the portion(s)	full article	**Title of the article/chapter the portion is from**	Antisite Defects Stabilized by Antiphase Boundaries in YFeO3 Thin Films
Editor of portion(s)	Abinash Kumar	**Author of portion(s)**	Abinash Kumar
Volume of serial or monograph	n/a	**Publication date of portion**	2022-02-23
Page or page range of portion	n/a-n/a		

RIGHTSHOLDER TERMS AND CONDITIONS

No right, license or interest to any trademark, trade name, service mark or other branding ("Marks") of WILEY or its licensors is granted hereunder, and you agree that you shall not assert any such right, license or interest with respect thereto. You may not alter, remove or suppress in any manner any copyright, trademark or other notices displayed by the Wiley material. This Agreement will be void if the Type of Use, Format, Circulation, or Requestor Type was misrepresented during the licensing process. In no instance may the total amount of Wiley Materials used in any Main Product, Compilation or Collective work comprise more than 5% (if figures/tables) or 15% (if full articles/chapters) of the (entirety of the) Main Product, Compilation or Collective Work. Some titles may be available under an Open Access license. It is the Licensors' responsibility to identify the type of Open Access license on which the requested material was published, and comply fully with the terms of that license for the type of use specified Further details can be found on Wiley Online Library http://olabout.wiley.com/WileyCDA/Section/id-410895.html.

Marketplace Order General Terms and Conditions

The following terms and conditions (“General Terms”), together with any applicable Publisher Terms and Conditions, govern User’s use of Works pursuant to the Licenses granted by Copyright Clearance Center, Inc. (“CCC”) on behalf of the applicable Rightsholders of such Works through CCC’s applicable Marketplace transactional licensing services (each, a “Service”).

1) **Definitions.** For purposes of these General Terms, the following definitions apply:

“License” is the licensed use the User obtains via the Marketplace platform in a particular licensing transaction, as set forth in the Order Confirmation.

“Order Confirmation” is the confirmation CCC provides to the User at the conclusion of each Marketplace transaction. “Order Confirmation Terms” are additional terms set forth on specific Order Confirmations not set forth in the General

Terms that can include terms applicable to a particular CCC transactional licensing service and/or any Rightsholder-specific terms.

"Rightsholder(s)" are the holders of copyright rights in the Works for which a User obtains licenses via the Marketplace platform, which are displayed on specific Order Confirmations.

"Terms" means the terms and conditions set forth in these General Terms and any additional Order Confirmation Terms collectively.

"User" or "you" is the person or entity making the use granted under the relevant License. Where the person accepting the Terms on behalf of a User is a freelancer or other third party who the User authorized to accept the General Terms on the User's behalf, such person shall be deemed jointly a User for purposes of such Terms.

"Work(s)" are the copyright protected works described in relevant Order Confirmations.

2) **Description of Service.** CCC's Marketplace enables Users to obtain Licenses to use one or more Works in accordance with all relevant Terms. CCC grants Licenses as an agent on behalf of the copyright rightsholder identified in the relevant Order Confirmation.

3) **Applicability of Terms.** The Terms govern User's use of Works in connection with the relevant License. In the event of any conflict between General Terms and Order Confirmation Terms, the latter shall govern. User acknowledges that Rightsholders have complete discretion whether to grant any permission, and whether to place any limitations on any grant, and that CCC has no right to supersede or to modify any such discretionary act by a Rightsholder.

4) **Representations; Acceptance.** By using the Service, User represents and warrants that User has been duly authorized by the User to accept, and hereby does accept, all Terms.

5) **Scope of License; Limitations and Obligations.** All Works and all rights therein, including copyright rights, remain the sole and exclusive property of the Rightsholder. The License provides only those rights expressly set forth in the terms and conveys no other rights in any Works

6) **General Payment Terms.** User may pay at time of checkout by credit card or choose to be invoiced. If the User chooses to be invoiced, the User shall: (i) remit payments in the manner identified on specific invoices, (ii) unless otherwise specifically stated in an Order Confirmation or separate written agreement, Users shall remit payments upon receipt of the relevant invoice from CCC, either by delivery or notification of availability of the invoice via the Marketplace platform, and (iii) if the User does not pay the invoice within 30 days of receipt, the User may incur a service charge of 1.5% per month or the maximum rate allowed by applicable law, whichever is less. While User may exercise the rights in the License immediately upon receiving the Order Confirmation, the License is automatically revoked and is null and void, as if it had never been issued, if CCC does not receive complete payment on a timely basis.

7) **General Limits on Use.** Unless otherwise provided in the Order Confirmation, any grant of rights to User (i) involves only the rights set forth in the Terms and does not include subsequent or additional uses, (ii) is non-exclusive and non-transferable, and (iii) is subject to any and all limitations and restrictions (such as, but not limited to, limitations on duration of use or circulation) included in the Terms. Upon completion of the licensed use as set forth in the Order Confirmation, User shall either secure a new permission for further use of the Work(s) or immediately cease any new use of the Work(s) and shall render inaccessible (such as by deleting or by removing or severing links or other locators) any further copies of the Work. User may only make alterations to the Work if and as expressly set forth in the Order Confirmation. No Work may be used in any way that is defamatory, violates the rights of third parties (including such third parties' rights of copyright, privacy, publicity, or other tangible or intangible property), or is otherwise illegal, sexually explicit, or obscene. In addition, User may not conjoin a Work with any other material that may result in damage to the reputation of the Rightsholder. User agrees to inform CCC if it becomes aware of any infringement of any rights in a Work and to cooperate with any reasonable request of CCC or the Rightsholder in connection therewith.

8) **Third Party Materials.** In the event that the material for which a License is sought includes third party materials (such as photographs, illustrations, graphs, inserts and similar materials) that are identified in such material as having been

used by permission (or a similar indicator), User is responsible for identifying, and seeking separate licenses (under this Service, if available, or otherwise) for any of such third party materials; without a separate license, User may not use such third party materials via the License.

9) **Copyright Notice.** Use of proper copyright notice for a Work is required as a condition of any License granted under the Service. Unless otherwise provided in the Order Confirmation, a proper copyright notice will read substantially as follows: "Used with permission of [Rightsholder's name], from [Work's title, author, volume, edition number and year of copyright]; permission conveyed through Copyright Clearance Center, Inc." Such notice must be provided in a reasonably legible font size and must be placed either on a cover page or in another location that any person, upon gaining access to the material which is the subject of a permission, shall see, or in the case of republication Licenses, immediately adjacent to the Work as used (for example, as part of a by-line or footnote) or in the place where substantially all other credits or notices for the new work containing the republished Work are located. Failure to include the required notice results in loss to the Rightsholder and CCC, and the User shall be liable to pay liquidated damages for each such failure equal to twice the use fee specified in the Order Confirmation, in addition to the use fee itself and any other fees and charges specified.

10) **Indemnity.** User hereby indemnifies and agrees to defend the Rightsholder and CCC, and their respective employees and directors, against all claims, liability, damages, costs, and expenses, including legal fees and expenses, arising out of any use of a Work beyond the scope of the rights granted herein and in the Order Confirmation, or any use of a Work which has been altered in any unauthorized way by User, including claims of defamation or infringement of rights of copyright, publicity, privacy, or other tangible or intangible property.

11) **Limitation of Liability.** UNDER NO CIRCUMSTANCES WILL CCC OR THE RIGHTSHOLDER BE LIABLE FOR ANY DIRECT, INDIRECT, CONSEQUENTIAL, OR INCIDENTAL DAMAGES (INCLUDING WITHOUT LIMITATION DAMAGES FOR LOSS OF BUSINESS PROFITS OR INFORMATION, OR FOR BUSINESS INTERRUPTION) ARISING OUT OF THE USE OR INABILITY TO USE A WORK, EVEN IF ONE OR BOTH OF THEM HAS BEEN ADVISED OF THE POSSIBILITY OF SUCH DAMAGES. In any event, the total liability of the Rightsholder and CCC (including their respective employees and directors) shall not exceed the total amount actually paid by User for the relevant License. User assumes full liability for the actions and omissions of its principals, employees, agents, affiliates, successors, and assigns.

12) **Limited Warranties.** THE WORK(S) AND RIGHT(S) ARE PROVIDED "AS IS." CCC HAS THE RIGHT TO GRANT TO USER THE RIGHTS GRANTED IN THE ORDER CONFIRMATION DOCUMENT. CCC AND THE RIGHTSHOLDER DISCLAIM ALL OTHER WARRANTIES RELATING TO THE WORK(S) AND RIGHT(S), EITHER EXPRESS OR IMPLIED, INCLUDING WITHOUT LIMITATION IMPLIED WARRANTIES OF MERCHANTABILITY OR FITNESS FOR A PARTICULAR PURPOSE. ADDITIONAL RIGHTS MAY BE REQUIRED TO USE ILLUSTRATIONS, GRAPHS, PHOTOGRAPHS, ABSTRACTS, INSERTS, OR OTHER PORTIONS OF THE WORK (AS OPPOSED TO THE ENTIRE WORK) IN A MANNER CONTEMPLATED BY USER; USER UNDERSTANDS AND AGREES THAT NEITHER CCC NOR THE RIGHTSHOLDER MAY HAVE SUCH ADDITIONAL RIGHTS TO GRANT.

13) **Effect of Breach.** Any failure by User to pay any amount when due, or any use by User of a Work beyond the scope of the License set forth in the Order Confirmation and/or the Terms, shall be a material breach of such License. Any breach not cured within 10 days of written notice thereof shall result in immediate termination of such License without further notice. Any unauthorized (but licensable) use of a Work that is terminated immediately upon notice thereof may be liquidated by payment of the Rightsholder's ordinary license price therefor; any unauthorized (and unlicensable) use that is not terminated immediately for any reason (including, for example, because materials containing the Work cannot reasonably be recalled) will be subject to all remedies available at law or in equity, but in no event to a payment of less than three times the Rightsholder's ordinary license price for the most closely analogous licensable use plus Rightsholder's and/or CCC's costs and expenses incurred in collecting such payment.

14) **Additional Terms for Specific Products and Services.** If a User is making one of the uses described in this Section 14, the additional terms and conditions apply:

a) ***Print Uses of Academic Course Content and Materials (photocopies for academic coursepacks or classroom handouts).*** For photocopies for academic coursepacks or classroom handouts the following additional terms apply:

i) The copies and anthologies created under this License may be made and assembled by faculty members

individually or at their request by on-campus bookstores or copy centers, or by off-campus copy shops and other similar entities.

ii) No License granted shall in any way: (i) include any right by User to create a substantively non-identical copy of the Work or to edit or in any other way modify the Work (except by means of deleting material immediately preceding or following the entire portion of the Work copied) (ii) permit "publishing ventures" where any particular anthology would be systematically marketed at multiple institutions.

iii) Subject to any Publisher Terms (and notwithstanding any apparent contradiction in the Order Confirmation arising from data provided by User), any use authorized under the academic pay-per-use service is limited as follows:

A) any License granted shall apply to only one class (bearing a unique identifier as assigned by the institution, and thereby including all sections or other subparts of the class) at one institution;

B) use is limited to not more than 25% of the text of a book or of the items in a published collection of essays, poems or articles;

C) use is limited to no more than the greater of (a) 25% of the text of an issue of a journal or other periodical or (b) two articles from such an issue;

D) no User may sell or distribute any particular anthology, whether photocopied or electronic, at more than one institution of learning;

E) in the case of a photocopy permission, no materials may be entered into electronic memory by User except in order to produce an identical copy of a Work before or during the academic term (or analogous period) as to which any particular permission is granted. In the event that User shall choose to retain materials that are the subject of a photocopy permission in electronic memory for purposes of producing identical copies more than one day after such retention (but still within the scope of any permission granted), User must notify CCC of such fact in the applicable permission request and such retention shall constitute one copy actually sold for purposes of calculating permission fees due; and

F) any permission granted shall expire at the end of the class. No permission granted shall in any way include any right by User to create a substantively non-identical copy of the Work or to edit or in any other way modify the Work (except by means of deleting material immediately preceding or following the entire portion of the Work copied).

iv) Books and Records; Right to Audit. As to each permission granted under the academic pay-per-use Service, User shall maintain for at least four full calendar years books and records sufficient for CCC to determine the numbers of copies made by User under such permission. CCC and any representatives it may designate shall have the right to audit such books and records at any time during User's ordinary business hours, upon two days' prior notice. If any such audit shall determine that User shall have underpaid for, or underreported, any photocopies sold or by three percent (3%) or more, then User shall bear all the costs of any such audit; otherwise, CCC shall bear the costs of any such audit. Any amount determined by such audit to have been underpaid by User shall immediately be paid to CCC by User, together with interest thereon at the rate of 10% per annum from the date such amount was originally due. The provisions of this paragraph shall survive the termination of this License for any reason.

b) ***Digital Pay-Per-Uses of Academic Course Content and Materials (e-coursepacks, electronic reserves, learning management systems, academic institution intranets).*** For uses in e-coursepacks, posts in electronic reserves, posts in learning management systems, or posts on academic institution intranets, the following additional terms apply:

i) The pay-per-uses subject to this Section 14(b) include:

A) **Posting e-reserves, course management systems, e-coursepacks for text-based content,** which grants

authorizations to import requested material in electronic format, and allows electronic access to this material to members of a designated college or university class, under the direction of an instructor designated by the college or university, accessible only under appropriate electronic controls (e.g., password);

B) **Posting e-reserves, course management systems, e-coursepacks for material consisting of photographs or other still images not embedded in text,** which grants not only the authorizations described in Section 14(b)(i)(A) above, but also the following authorization: to include the requested material in course materials for use consistent with Section 14(b)(i)(A) above, including any necessary resizing, reformatting or modification of the resolution of such requested material (provided that such modification does not alter the underlying editorial content or meaning of the requested material, and provided that the resulting modified content is used solely within the scope of, and in a manner consistent with, the particular authorization described in the Order Confirmation and the Terms), but not including any other form of manipulation, alteration or editing of the requested material;

C) **Posting e-reserves, course management systems, e-coursepacks or other academic distribution for audiovisual content,** which grants not only the authorizations described in Section 14(b)(i)(A) above, but also the following authorizations: (i) to include the requested material in course materials for use consistent with Section 14(b)(i)(A) above; (ii) to display and perform the requested material to such members of such class in the physical classroom or remotely by means of streaming media or other video formats; and (iii) to "clip" or reformat the requested material for purposes of time or content management or ease of delivery, provided that such “clipping” or reformatting does not alter the underlying editorial content or meaning of the requested material and that the resulting material is used solely within the scope of, and in a manner consistent with, the particular authorization described in the Order Confirmation and the Terms. Unless expressly set forth in the relevant Order Conformation, the License does not authorize any other form of manipulation, alteration or editing of the requested material.

ii) Unless expressly set forth in the relevant Order Confirmation, no License granted shall in any way: (i) include any right by User to create a substantively non-identical copy of the Work or to edit or in any other way modify the Work (except by means of deleting material immediately preceding or following the entire portion of the Work copied or, in the case of Works subject to Sections 14(b)(1)(B) or (C) above, as described in such Sections) (ii) permit "publishing ventures" where any particular course materials would be systematically marketed at multiple institutions.

iii) Subject to any further limitations determined in the Rightsholder Terms (and notwithstanding any apparent contradiction in the Order Confirmation arising from data provided by User), any use authorized under the electronic course content pay-per-use service is limited as follows:

A) any License granted shall apply to only one class (bearing a unique identifier as assigned by the institution, and thereby including all sections or other subparts of the class) at one institution;

B) use is limited to not more than 25% of the text of a book or of the items in a published collection of essays, poems or articles;

C) use is limited to not more than the greater of (a) 25% of the text of an issue of a journal or other periodical or (b) two articles from such an issue;

D) no User may sell or distribute any particular materials, whether photocopied or electronic, at more than one institution of learning;

E) electronic access to material which is the subject of an electronic-use permission must be limited by means of electronic password, student identification or other control permitting access solely to students and instructors in the class;

F) User must ensure (through use of an electronic cover page or other appropriate means) that any person,

upon gaining electronic access to the material, which is the subject of a permission, shall see:

- a proper copyright notice, identifying the Rightsholder in whose name CCC has granted permission,
- a statement to the effect that such copy was made pursuant to permission,
- a statement identifying the class to which the material applies and notifying the reader that the material has been made available electronically solely for use in the class, and
- a statement to the effect that the material may not be further distributed to any person outside the class, whether by copying or by transmission and whether electronically or in paper form, and User must also ensure that such cover page or other means will print out in the event that the person accessing the material chooses to print out the material or any part thereof.

G) any permission granted shall expire at the end of the class and, absent some other form of authorization, User is thereupon required to delete the applicable material from any electronic storage or to block electronic access to the applicable material.

iv) Uses of separate portions of a Work, even if they are to be included in the same course material or the same university or college class, require separate permissions under the electronic course content pay-per-use Service. Unless otherwise provided in the Order Confirmation, any grant of rights to User is limited to use completed no later than the end of the academic term (or analogous period) as to which any particular permission is granted.

v) Books and Records; Right to Audit. As to each permission granted under the electronic course content Service, User shall maintain for at least four full calendar years books and records sufficient for CCC to determine the numbers of copies made by User under such permission. CCC and any representatives it may designate shall have the right to audit such books and records at any time during User's ordinary business hours, upon two days' prior notice. If any such audit shall determine that User shall have underpaid for, or underreported, any electronic copies used by three percent (3%) or more, then User shall bear all the costs of any such audit; otherwise, CCC shall bear the costs of any such audit. Any amount determined by such audit to have been underpaid by User shall immediately be paid to CCC by User, together with interest thereon at the rate of 10% per annum from the date such amount was originally due. The provisions of this paragraph shall survive the termination of this license for any reason.

c) ***Pay-Per-Use Permissions for Certain Reproductions (Academic photocopies for library reserves and interlibrary loan reporting) (Non-academic internal/external business uses and commercial document delivery).*** The License expressly excludes the uses listed in Section (c)(i)-(v) below (which must be subject to separate license from the applicable Rightsholder) for: academic photocopies for library reserves and interlibrary loan reporting; and non-academic internal/external business uses and commercial document delivery.

i) electronic storage of any reproduction (whether in plain-text, PDF, or any other format) other than on a transitory basis;

ii) the input of Works or reproductions thereof into any computerized database;

iii) reproduction of an entire Work (cover-to-cover copying) except where the Work is a single article;

iv) reproduction for resale to anyone other than a specific customer of User;

v) republication in any different form. Please obtain authorizations for these uses through other CCC services or directly from the rightsholder.

Any license granted is further limited as set forth in any restrictions included in the Order Confirmation and/or in these Terms.

d) ***Electronic Reproductions in Online Environments (Non-Academic-email, intranet, internet and extranet).*** For "electronic reproductions", which generally includes e-mail use (including instant messaging or other electronic transmission to a defined group of recipients) or posting on an intranet, extranet or Intranet site (including any display or performance incidental thereto), the following additional terms apply:

i) Unless otherwise set forth in the Order Confirmation, the License is limited to use completed within 30 days for any use on the Internet, 60 days for any use on an intranet or extranet and one year for any other use, all as measured from the "republication date" as identified in the Order Confirmation, if any, and otherwise from the date of the Order Confirmation.

ii) User may not make or permit any alterations to the Work, unless expressly set forth in the Order Confirmation (after request by User and approval by Rightsholder); provided, however, that a Work consisting of photographs or other still images not embedded in text may, if necessary, be resized, reformatted or have its resolution modified without additional express permission, and a Work consisting of audiovisual content may, if necessary, be "clipped" or reformatted for purposes of time or content management or ease of delivery (provided that any such resizing, reformatting, resolution modification or “clipping” does not alter the underlying editorial content or meaning of the Work used, and that the resulting material is used solely within the scope of, and in a manner consistent with, the particular License described in the Order Confirmation and the Terms.

15) **Miscellaneous.**

a) User acknowledges that CCC may, from time to time, make changes or additions to the Service or to the Terms, and that Rightsholder may make changes or additions to the Rightsholder Terms. Such updated Terms will replace the prior terms and conditions in the order workflow and shall be effective as to any subsequent Licenses but shall not apply to Licenses already granted and paid for under a prior set of terms.

b) Use of User-related information collected through the Service is governed by CCC's privacy policy, available online at www.copyright.com/about/privacy-policy/.

c) The License is personal to User. Therefore, User may not assign or transfer to any other person (whether a natural person or an organization of any kind) the License or any rights granted thereunder; provided, however, that, where applicable, User may assign such License in its entirety on written notice to CCC in the event of a transfer of all or substantially all of User's rights in any new material which includes the Work(s) licensed under this Service.

d) No amendment or waiver of any Terms is binding unless set forth in writing and signed by the appropriate parties, including, where applicable, the Rightsholder. The Rightsholder and CCC hereby object to any terms contained in any writing prepared by or on behalf of the User or its principals, employees, agents or affiliates and purporting to govern or otherwise relate to the License described in the Order Confirmation, which terms are in any way inconsistent with any Terms set forth in the Order Confirmation, and/or in CCC's standard operating procedures, whether such writing is prepared prior to, simultaneously with or subsequent to the Order Confirmation, and whether such writing appears on a copy of the Order Confirmation or in a separate instrument.

e) The License described in the Order Confirmation shall be governed by and construed under the law of the State of New York, USA, without regard to the principles thereof of conflicts of law. Any case, controversy, suit, action, or proceeding arising out of, in connection with, or related to such License shall be brought, at CCC's sole discretion, in any federal or state court located in the County of New York, State of New York, USA, or in any federal or state court whose geographical jurisdiction covers the location of the Rightsholder set forth in the Order Confirmation. The parties expressly submit to the personal jurisdiction and venue of each such federal or state court.

CAMBRIDGE UNIVERSITY PRESS LICENSE
TERMS AND CONDITIONS

Jul 25, 2022

This Agreement between Mr. Abinash Kumar ("You") and Cambridge University Press ("Cambridge University Press") consists of your license details and the terms and conditions provided by Cambridge University Press and Copyright Clearance Center.

License Number	5327491006861
License date	Jun 14, 2022
Licensed Content Publisher	Cambridge University Press
Licensed Content Publication	Microscopy and Microanalysis
Licensed Content Title	In Situ Ferroelectric Domain Dynamics Probed with Differential Phase Contrast Imaging
Licensed Content Author	Abinash Kumar, Rohan Dhall, James M. LeBeau
Licensed Content Date	Aug 5, 2019
Licensed Content Volume	25
Licensed Content Issue	S2
Start page	1838
End page	1839
Type of Use	Book/Textbook

Requestor type	Author
Requestor details	Not-for-profit
Format	Print and electronic
Portion	Full article
Distribution quantity	1000000
Author of this Cambridge University Press article	Yes
Author / editor of the new work	Yes
Will you be translating?	No
Title of new book	Structure-property correlations in compositionally complex ferroelectrics
Lead author	Abinash Kumar
Publisher	Massachusetts Institute of Technology
Expected publication date	Jul 2022
Expected number of pages	2
Territory for reuse	World
If publisher of new book has its main base in USA, Canada or Mexico	Yes
	Mr. Abinash Kumar

Requestor Location	70 Pacific St Cambridge, MA 02139 United States Attn: Mr. Abinash Kumar
Publisher Tax ID	GB823847609
Total	0.00 USD

Terms and Conditions

TERMS & CONDITIONS

Cambridge University Press grants the Licensee permission on a non-exclusive non-transferable basis to reproduce, make available or otherwise use the Licensed content 'Content' in the named territory 'Territory' for the purpose listed 'the Use' on Page 1 of this Agreement subject to the following terms and conditions.

1. The License is limited to the permission granted and the Content detailed herein and does not extend to any other permission or content.
2. Cambridge gives no warranty or indemnity in respect of any third-party copyright material included in the Content, for which the Licensee should seek separate permission clearance.
3. The integrity of the Content must be ensured.
4. The License does extend to any edition published specifically for the use of handicapped or reading-impaired individuals.
5. The Licensee shall provide a prominent acknowledgement in the following format: author/s, title of article, name of journal, volume number, issue number, page references, , reproduced with permission.

Other terms and conditions:

v1.0

Questions? customercare@copyright.com or +1-855-239-3415 (toll free in the US) or +1-978-646-2777.